Technical University of Denmark

DTU

Joachim Skov Johansen

Fast-Charging Electric Vehicles using AC

Master's Thesis, September 2013

DTU Electrical Engineering
Department of Electrical Engineering

Joachim Skov Johansen

Fast-Charging Electric Vehicles using AC

Master's Thesis, September 2013

Fast-Charging Electric Vehicles using AC

This report was prepared by
  Joachim Skov Johansen

Contact
  joachimskovjohansen@gmail.com
  Newest version available at
  http://udel.edu/~jsj/JSJ-EV-AC-Fast-Charging-Thesis.pdf

Advisors
  PhD Peter Bach Andersen
  Associate Professor Tonny Wederberg Rasmussen
  Associate Professor Chresten Træholt

Department of Electrical Engineering
Centre for Electric Technology (CET)
Technical University of Denmark
Elektrovej building 325
DK-2800 Kgs. Lyngby
 Denmark

www.elektro.dtu.dk/cet
Tel: (+45) 45 25 35 00
Fax: (+45) 45 88 61 11
E-mail: cet@elektro.dtu.dk

Abstract

Electric vehicles are here. Sales figures are approximately doubling each year, and the growth is projected to continue. The goal is to have 20 million electric vehicles on the roads by 2020. In order to reach this goal, it is now time to make intelligent choices for the next-generation electric drive technologies.

One major challenge with electric vehicles is range anxiety. This project investigates AC fast-charging as a means of mitigating range anxiety while lowering total cost of electric vehicle roll-outs. The benefit of AC charging is that it allows vehicles to charge from an inexpensive AC charging station feeding power directly from the electric grid to the vehicle. Charge rates up to 43kW in Europe and 52kW in US are supported with standard AC cord sets. This power level matches that of the more expensive DC chargers. Hence, AC fast-charging technologies are an effective catalyst for considerably expanding fast-charging infrastructure.

With AC fast-charging, high-power electronics are required onboard the vehicle. By reusing traction components for charging purposes, the onboard converter can be made inexpensive with only few additional components. The possible practical challenges with this high-power charger topology have been identified, and no barriers are found. Furthermore, these components allow bidirectional power flow, enabling vehicle-to-grid (V2G), vehicle-to-load (V2L) and grid-forming operation. This serves as an additional economical incentive for deploying AC fast-charging technologies.

A novel low-cost 63A AC-only fast-charging station is developed. The all-electric Renault Zoe is charged at 43kW, proving AC fast-charging is indeed realizable. To support AC fast-charging at sites with limited grid power, a simple and practical load management algorithm is presented. Finally, high-level IP communication is enabled through the upcoming IEC 61851-1 Annex D standard, and EVs can be connected to the Internet or other IP networks.

The project concludes that fast-charging using AC is feasible and practically realizable. If the recommendations presented are taken into account in future EVs and infrastructure implementations, it is expected that EV fast-charging will be easily accessible, range anxiety is minimized and costs related to increasing EV penetration are considerably reduced.

Resumé

Elbiler er kommet for at blive. Salgstallene fordobles hvert år, og væksten ser ud til at fortsætte. Målsætningen er at have 20 millioner elbiler på vejene i år 2020. For at opnå dette mål er det nødvendigt at træffe fornuftige valg i dag for teknologien i den næste generations elbiler.

Én af elbilens største udfordringer er bekymringen for en for kort rækkevidde og dermed at løbe tør for strøm. Dette projekt undersøger hvordan man ved hjælp af AC hurtigladning reducerer rækkeviddebekymringen, samtidig med at omkostningen til fremtidig elbilsudrulning minimeres. Fordelen ved AC ladning er at elbiler kan lades fra billige AC ladestandere, hvor strømmen føres direkte fra elnettet til bilen. Det er muligt at opnå ladeeffekter op til 43kW i Europa og 52kW i USA med almindelige, standardiserede ladekabler. Dette effektniveau svarer til dét en noget dyrere DC-ladestander kan levere. På denne måde kan AC hurtigladning fungere som en katalysator til fremtidig udbygning af ladeinfrastruktur.

Med AC hurtigladning er det nødvendigt at placere højeffektelektronik til opladning af batteriet i bilen. Omkostningen ved dette kan reduceres ved at anvende den eksisterende fremdrifts-elektronik, der driver elmotoren, til også at bruges til opladning af batteriet. Udfordringer i forbindelse med denne metode identificeres, og der findes ingen direkte hindringer for praktisk anvendelse. Med denne teknologi muliggøres også tilbageløbseffekt, hvilket omfatter at strøm kan løbe fra bil til elnet (V2G), fra bil til belastning (V2L) eller bilen kan spændingsstøtte elnettet (grid-forming). Dette udgør et yderligere økonomisk incitament for AC hurtigladning.

En ny 63A AC hurtigladestander er udviklet. Elbilen Renault Zoe lades med 43kW, hvilket viser at AC-hurtigladning er praktisk muligt og realiserbart. I det tilfælde at et tilslutningspunkt i elnettet ikke understøtter hurtigladning af mange biler samtidig, er der udviklet en simpel og praktisk algoritme til håndtering af denne type belastning. Derudover er højniveaukommunikation muliggjort ved hjælp af den nye IEC 61851-1 Annex D standard, og det vises hvordan elbiler kan kommunikere til Internettet eller andre IP netværk.

Projektet konkluderer, at hurtigladning med AC er muligt og realiserbart. Såfremt der tages hensyn til de præsenterede anbefalinger, er det forventet at hurtigladning i fremtiden vil være let tilgængeligt, at rækkeviddebekymringen minimeres og omkostninger i forbindelse med udrulning af elbiler reduceres markant.

Acknowledgements

I would like to thank my closest for their help and support throughout the project.

Contents

List of Figures

List of Tables

Introduction

The interest in electric vehicles has increased rapidly over the past few years. An important milestone was reached in 2012 with more than 100.000 hybrid and all-electric vehicles sold globally, and sales figures are approximately doubling each year [18]. Many automobile manufacturers have at this point developed and commercialized their first modern electric models, proving that the electric drive is technically viable, environmentally friendly and affordable. Manufacturers are now approaching a subsequent phase in their development efforts that entails building powerful, long-range, fast-charging, more efficient and cheaper electric vehicles. This makes it a good time to think beyond proof-of-concept solutions, and to make intelligent choices for the next-generation electric drive technologies that once and for all give electric vehicles its rightful place in the transportation market.

The concern with all-electric vehicles (EV) is their limited driving range on a fully charged battery, also known as range anxiety. The range is usually between 100km and 500km for a modern EV. At the same time, the refueling time for an electric vehicle is long, ranging from 30 minutes to 10 hours or more. Therefore, consumers feel this is too restraining and stick with their conventional gasoline vehicle (GV) that can be refueled almost anywhere in 5-10 minutes or less.

There are many ways to mitigate the problem of range anxiety for EVs, one of which is the focus of this report, namely fast-charging. The basic idea is that if the charging power of the vehicle can be increased, then the time to charge the vehicle is lowered correspondingly. If the charging time is less than 30-60 minutes then en-route charging is possible, given that charging stations have been installed at appropriate locations. Charging times of around 2-4 hours are also useful, since this enables charging at e.g. a work place or other sites where the vehicle is parked during the day. This effectively doubles the driving range, because the vehicle can be fully recharged before it returns to its over-night charging spot.

For instance, if a vehicle with a driving range of 200km is charged at its destination then its effective range is 400km. A study on US consumers' driving range gives

a conservative estimate of possible EV penetration with a widely deployed fast-charging infrastructure [60]. With a vehicle range of 400km, 45% of all vehicles can be replaced with EVs without constraining the user's driving behaviour. This corresponds to a global market of more than 450 million vehicles that could be EVs today.

However, there is one possible show-stopper in this equation. If the fast-charging equipment turns out to be expensive or otherwise infeasible then it is unlikely to become widely adopted, and EV penetration will be considerably lower due to the aforementioned range anxiety. The cost of the charging equipment is therefore a major concern, and will become even more so when public funding for infrastructure pilot projects declines in the future.

The focus in this project is on driving down cost of fast-charging equipment by charging the EV with power from an AC charging station connected directly to the electric grid. The current approach to EV fast-charging uses DC chargers, which are bulky and pricy because they contain additional high power circuitry to convert the grid's AC into DC. The approach in this project is to investigate a concept known as *integrated motor drives* [40], where the existing traction components onboard the vehicle are reused for the purpose of charging the battery also. This eliminates redundancy in power electronics hardware and should thus come at little additional cost to the vehicle manufacturer. On the infrastructure side, an AC charging station is required, which allows power transfer directly from the grid to the car. An AC charging station can therefore be constructed as simple, small and inexpensive units.

This project encompasses many topics ranging from high power electronics onboard the vehicle to load management algorithms in the charging station. This holistic approach is necessary to efficiently select the charging solution that lowers overall system cost and provides the most benefits for the stakeholders of the EV industry, including the EV users. Therefore, it is essential to investigate and discuss a wide range of technologies from the perspective of both the EV and the charging infrastructure.

Problem statement

The project shall explore fast-charging of EVs using AC with the goal of lowering total system cost of EV roll-outs while mitigating range anxiety and providing additional grid services. The arguments for using AC fast-charging must be spelled out, and policy recommendations must be stated to improve current EV technology and infrastructure solutions.

A simulation of a 63A high-power battery charger must be developed in Simulink. The charger shall be based on a three-phase two-level bidirectional topology that supports charging the battery from the AC grid with unity power factor. The project should also explore:

- How the converter can be used to provide services, such as reverse active power flow (also known as vehicle to grid, V2G), reactive power compensation, grid-forming operation, and other ancillary services.

- The practical challenges in utilizing this converter topology and how these can be handled. For example, the construction of the inductance required in the topology should be addressed as well as the minimum DC voltage requirement.

Furthermore, a fast-charging three-phase AC charging station must be procured and extended to support:

- Three-phase charging up to 63A per phase using the standardized IEC 62196 Type 2 cord set.
- CAN Communication over the control pilot wire, based on IEC 61851-1 Ed. 3 Annex D.

To allow future AC fast-charging infrastructure rollouts, a description of a simple load management algorithm must be given with the goal of effectively sharing available grid power at a site.

Outline

The introductory chapter 1 provides an overview of the various EV technologies in use today. At the same time, this chapter elaborates on the argument of why AC fast-charging for electric vehicles is a good idea. Fourteen such arguments are stated.

The report investigates the two main components required for AC fast-charging: The power converter onboard the vehicle (chapter 2), and the required off-board infrastructure, including the high-power cord set and charging stations (chapter 3). These components are shown in fig. 1.

All chapters and most sections provide a brief introduction and conclusion so that each section stands relatively independently and many sections may be read by non electrical engineers, especially in chapters 1 and 3.

Approach

The report approaches the topic of EV fast-charging from a systems engineering perspective. This is important because EV charging is an interdisciplinary field in which a best solution can only be obtained by addressing multiple subtopics within policy, standardization, economics and engineering, including software, hardware and communications engineering. This holistic approach requires a detailed analysis and comparison of existing and possible future charging technologies followed by stating actual solutions and recommendations. This does not necessarily entail leaving out technical details, rather, the point is to select the technologies to explore based on clear and sensible arguments before actually investigating the technologies in question.
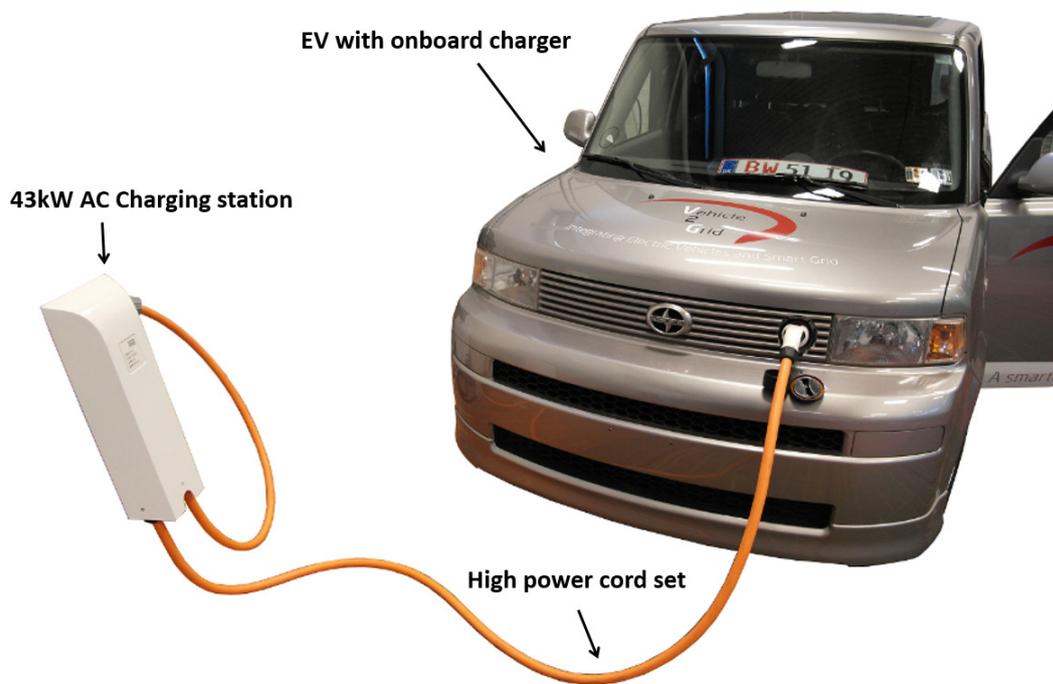
Figure 1: Overview of EV components

CHAPTER 1

Technology overview

1.1 Why Electric Vehicles?

Why concern ourselves with EVs when they have limited range and hence seem inferior to other types of vehicles? After all, other types of environment-friendly vehicles exist. Most notably, plug-in hybrid electric vehicles (PHEV) are becoming increasingly popular. This type of vehicle carries both a conventional gasoline engine along with a battery and an electric motor, and the battery can be charged by plugging into an outlet or a charging station. As such, the PHEV attempts to use the best of two worlds: The long driving range is provided by the conventional gasoline engine, while the electric powertrain makes the vehicle efficient and clean. By using technologies such as regenerative braking and running the engine only at rpms where it has maximum efficiency give the PHEV a high mileage and low emissions. However, there are two major downsides to the PHEV concept:

1. A hybrid vehicle is still highly dependent on gas.
2. A hybrid vehicle is much more complex since it has two powertrains. This makes the vehicle more expensive in upfront cost and in maintenance compared to both gasoline vehicles and electric vehicles that rely on a single powertrain.

In combination with these reasons, some countries, such as Denmark, are currently not offering tax deductions on hybrid vehicles, while EVs are often fiscally incentivized. For example, EVs are in Denmark exempt from the 180% registration tax that is put on both hybrid and gasoline personal vehicles [1]. In the US, a tax credit worth $7.500 is offered on both EVs and hybrids [42].

Whereas the hybrid and the gasoline vehicle relies on a rather complex powertrain, an electric vehicle is on the other hand quite simple. It consists of mainly three

---

[1]There is still 25% VAT on EVs. The exact registration tax for a vehicle is a somewhat complicated calculation, but it is approximately 105% up to a car value of 79.000DKK and 180% above, see [62].

electric power components: An electric motor with a gear box, a battery and power electronics for driving the motor and charging. An EV often uses a fixed-ratio transmission because the motor can run at many speeds and still provide its maximum torque and power. Only a few frictional parts are located between the motor and the wheels: The bearings in the motor, the single gear in the gear box and the drive shafts for the wheels. This causes EVs to require little maintenance. Compare this to a gasoline vehicle with pistons, valves, turbo, crankshaft, camshaft, etc., all frictional parts that are soaked in oil to limit wear. The fact that an EV motor provides maximum torque over a wide range of speeds, also at zero rpm, makes EVs snappy and many EV models outrun comparable gasoline vehicles. At this point in time, EVs are rather expensive compared to conventional cars, largely due to non-recurring engineering (NRE) investments made by several big OEMs[2]. However, due to simplicity in the construction of EVs and the potential for economies of scale, they are likely to become cheaper than gasoline vehicles eventually.

Gasoline and hybrid vehicles rely on gas refined from oil, and oil dependency is a controversial topic in many industrialized countries, especially those that are not self-sufficient like the US. The Americans have a huge interest in becoming independent of foreign oil, and oil in general. This was immediately apparent during the 2012 presidential election [51], where it was often debated whether US energy independence should be ensured by increasing domestic oil production or through renewable energy initiatives.

In the book *Lives per gallon* by Tamminen [63] it is attempted to put a value on the subsidies that the oil industry enjoys, as well as the various externalities related to the burning of fossil fuels. This is obviously a difficult task, because, for example, health-care costs due to increased pollution are difficult to quantify: What is the cost of lost productivity, or what is the cost of an early death? Tamminen estimates the annual cost of oil subsidies and externalities such as health-care, water pollution and damage to crops and forests etc. is around $1 trillion in US. It also quickly turns into a political discussion, because it may be argued [47] that the war in Iraq was fought to secure oil reserves, a war that costs at least $100 billion annually [63]. Therefore, EVs have a potential for massively reducing global expenditure related to oil procurement and burning.

EV opponents argue that EVs are not environmentally friendly due to emissions from the "long tail-pipes", implying the pollution generated by the centralized and often coal-fired electric power plants should be taken into account [59]. Obviously, the effective emission level for EVs depend highly on which type of power plant is generating the electric power. There are no emissions if an EV is powered from photovoltaics or wind, and if they're powered by a US national average electric generation mix, emissions from an EV are 54% lower than an average new vehicle [26]. However, the key benefit is that an EV does not care what type of power plant that generates its electricity. Since more renewable energy production will be introduced in the future, EVs will continue to reduce their green house gas footprint. Furthermore, EVs significantly reduce urban pollution.

Denmark is a global front runner with green technology and renewable energy production. In 2012, 49% of the electrical energy was produced by renewables

---

[2]Renault has spent at least $5 billion on EV development [22]

[31], compared to the global average of 19% [70]. Furthermore, Denmark is known for its widespread use of district heating, where excess heat from power plants is provided to homes. For example, the Avedøre Power Station is powered primarily by coal and reaches efficiencies up to 94% [27]. Thus, Denmark takes advantage of the flexibility in electric power generation, and the effective pollution from EVs is therefore tiny compared to conventional vehicles.

The intermittent nature of many renewables such as wind and solar require considerations on how to deliver energy when production from renewables is not sufficient. The *Smart Grid* technology is positioned to solve this task. One key component in the Smart Grid is an intelligent control of the timing, rate and possibly direction of the power flow between vehicle and grid. For example, when excess renewable power is generated, the charge rate of EVs can increase to utilize renewables as much as possible. The Vehicle To Grid (V2G) technology expands the possibilities of using EVs as part of the grid, because a V2G-enabled car can both charge and discharge and effectively be used as an energy buffer in the grid. A study shows that the grid can be powered by renewables cost-efficiently up to 99.9% of the time through the use of V2G-enabled cars [25]. Furthermore, it turns out that V2G technology relies heavily on the use of AC fast-charging and integrated motor drives, for reasons that will be spelled out in section 1.5 and throughout the report.

There is no doubt that EVs are a viable solution to personal transportation, and the sooner we can mitigate the issue of range anxiety, the sooner we will see a significant increase in EV penetration. This entails energy independence, increased renewable energy production, reduced smog and pollution while at the same time driving cheap, powerful and low-maintenance cars.

1.2 EVs, connectors and charging power levels

A selection of available EVs and their charging powers are provided in Table 1.1, sorted by charging power[3]. A few important facts are clear from the table: All EVs have an onboard charger, meaning they can charge from a regular AC outlet. Most EVs have a relatively low charge level of around 3.3kW or 6.6kW, and at these rates, single-phase charging is always used. Many vehicles rely on an off-board charging mechanism to support higher charge levels, especially those that have a low AC charge level. This is often offered by DC charging or in the case of the Fluence ZE, battery swap[4]. However, it is also evident that some manufacturers use faster AC chargers, including Tesla, BMW, Volvo and Renault.

Tesla uses three-phase chargers in Europe. They use single-phase chargers rated for 20kW in US, since three-phase service is not typically found in residential locations in the US. The BMW Mini-E was developed with a powertrain from the American supplier AC Propulsion, who also uses a single-phase onboard charger rated for 19kW (240V/80A). Volvo uses powertrains from the Swiss manufacturer Brusa, who develops three-phase onboard chargers rated for 22kW (3x32A at 230V). Renault has developed their own high power onboard charger known as Chameleon [29],

---

[3]The information has been gathered from various websites, brochures and tests by best effort.

[4]Better Place, the supplier of Renault Fluence and battery swapping stations went bankrupt in May 2013 [23], and thus the Fluence is quickly becoming antiquated

	AC charger (Phases/kW)	Energy storage (kWh)	Approximate range (km)	Off-board charge option
Renault Zoe	3/43	22	210 (NEDC)	No
Volvo C30 Electric	3/22	24	150 (NEDC)	No
Tesla Model S	1|3/22	85	480 (Tesla)	Yes (Tesla)
BMW Mini-E	1/19	35	160 (BMW)	No
Nissan Leaf 2013	1/6.6	24	135 (EPA)	Yes (CHAdeMO)
Ford Focus Electric	1/6.6	23	122 (EPA)	No
Think City 2011	1/3.6	24	160 (Think)	No
Renault Fluence ZE	1/3.6	22	185 (NEDC)	Yes (Bat Swap)
Chevy Spark EV	1/3.3	21	132 (EPA)	Yes (Combo)
Mitsubishi i-MiEV	1/3.3	16	100 (EPA)	Yes (CHAdeMO)
Chevy Volt (hybrid)	1/3.3	16	60 (EPA)	No

Table 1.1: Some EVs, their range and charge options

referring to the fact that it charges at many power levels ranging from 3kW to 43kW (3x63A at 230V).

The connectors and their power limits for charging EVs are presented in Table 1.2. There are mainly two AC connection solutions on the market, as shown in fig. 1.1: The Type 1 (also known as SAE J1772), a single-phase connector often used in the US and Asia, and the Type 2 (sometimes known as the IEC 61851[5] connector), a three-phase connector mostly used in Europe. The terms "Type" 1 and 2 connectors are defined in the standard IEC 62196-1.

Figure 1.1: A typical three-phase IEC 61851 compliant Type 2 connector (left) and a single-phase J1772 Type 1 connector (right)

Single-phase connections with a voltage of 120V is found only in US and Asia, so this type of charging is not applicable for Europe. The 120V circuits often have circuit breakers rated at 16A, and the maximum power from this type of outlet is

---

[5]The three-phase connector's functionality and requirements are defined by the standard IEC 61851-1. This is similar to the definitions in SAE J1772

	Connection type	Max voltage/amps	Max power (kW) EU US	
Type 1 level 1	1 (split) phase AC	120V/16A		1.9
Type 1 level 2	1 phase AC	240V/80A	14	19
Type 2	1-3 phase AC	480V/63A	43	52
CHAdeMO	DC	500V/125A	63	
Type 3 Combo	DC	1000V/400A[6]	36-200+	

Table 1.2: EV connector standards

around 2kW. The higher 240V single-phase voltage in the US has a maximum rated amperage of 80A according to the standard, yielding a maximum power of around 19kW. In Europe, the single-phase voltage is 230V, and since circuit breakers are typically rated no more than 63A, the maximum single-phase power in practice is around 14kW.

The power capabilities of the three-phase AC connectors are also different between Europe and US, because US three-phase voltages are 480V, compared to the European three-phase voltage of 400V. Since the rated amperage is equal, the three-phase power levels are a bit higher in the US. Therefore, the Type 2 three-phase connector has a standardized maximum power level of 52kW in the US, and it will in practice achieve a maximum of 43kW in Europe.

The CHAdeMO connector is a Japanese initiative for a global DC charging method. It is standardized to a maximum power of 63kW, and is currently the most prevailing DC charging solution with more than 2700 installations worldwide [4]. However, even though the DC power level is rated for 63kW, not many DC-charged vehicles actually support it, nor do the charging stations that use CHAdeMO connectors. The Nissan Leaf, for example, uses the CHAdeMO plug and supports up to 44kW charging [9]. Most CHAdeMO charging stations supply up to a maximum of 50kW[7].

SAE and IEC is currently working on defining a universal connector for DC charging. This is known as the DC Combo plug or the "Combined Charging System", since it unites AC and DC pins in the same connector. It even allows transferring DC power over the usual AC pins, which introduces a new concept of "slow" DC charging with power levels around 40kW. However, with dedicated high-power DC pins the plug is rated for power levels of up to 200kW (e.g. 750V/250A) or more. The standard IEC 62196-3 defines these DC plugs and combined plugs, and it is planned to be published late 2013. As mentioned before, even though very high power levels are standardized and supported by the connectors, it is not implied that vehicles can actually charge at these rates.

Clearly, some development has already been undertaken with faster AC charging as seen with the Renault Zoe, Volvo C30 Electric and the Teslas. However, most EVs do not support AC charging above 3.3kW. This leads us to one important argument for the use of AC fast-charging, as follows.

---

[7]A discussion on industry terminology in relation to AC and DC fast-charging is provided in appendix F

AC fast-charging argument #1:

Mismatch between standardized charge rates and EV capabilities

Many EVs do not support AC charging power levels higher than 6.6kW, but the AC connectors support single-phase power levels up to 19kW (US), 14kW (EU) and three-phase power levels up to 52kW (US), 43kW (EU). Thus, there is a considerable potential for increasing AC charge levels within existing charging standards.

1.2.1 Charge level and average traction power

Eventually, the maximum charge level supported by an EV, be it supplied with DC or AC, is limited by the tolerable heat dissipation in the power electronics and the battery. In this section we focus on the power dissipated in the battery due to I^2R losses, where R is the battery's internal resistance. As an example, a Brusa battery has a rated resistance of 150mΩ at 400V [24]. The battery temperature must be maintained within 0-40°C. If the battery is charged with 43kW, the current in the DC battery wires and the battery is approximately:

$$I_{dc} = \frac{43\text{kW}}{400\text{V}} \approx 108\text{A} \tag{1.1}$$

The heat dissipation in the battery is then

$$P_{loss} = 150\text{m}\Omega \cdot 108\text{A}^2 \approx 1730W \tag{1.2}$$

Therefore, the DC bus must be designed to sustain an average current of 108A, and the thermal management system in an EV must be designed so that the battery can be operated within specified temperature while driving and charging. Some lithium-ion battery chemistries are also limited by high charge and discharge rates, but we will neglect this here. The charging process of a battery involves a constant current scheme (e.g. between 0-80% state of charge, SOC) and a constant voltage scheme (e.g. between 80-100% SOC). We assume the constant current scheme is used here, since the battery power is limited by the maximum battery voltage rather than temperature in the constant voltage region.

The traction power required for a Tesla Roadster is shown in Figure 1.2. This shows that traction power increases quadratically with speed. When the EV drives 80km/hr it draws 10kW, but doubling the power to 20kW only increases speed 38% to 110km/hr. This means an EV's top speed is limited by the maximum average traction power delivered by the battery, if nothing else limits it[8]. If the top speed were 150km/hr, then this vehicle would require the battery to deliver 42kW on average without overheating.

---

[8]Acceleration and motor rpm could also be used as design constraints, but this is not considered in present discussion.
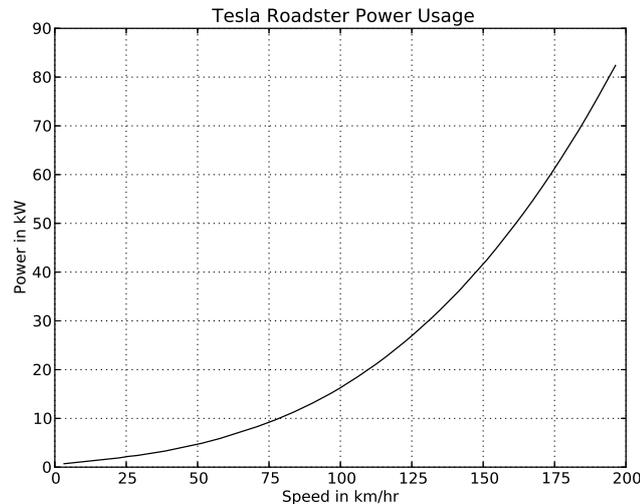
Figure 1.2: Tesla Roadster power versus speed [64]

The top speed for the Nissan Leaf coincides since it is around 150km/hr. Roughly assuming the Leaf uses a similar amount of power as the Tesla Roadster, the battery must be rated for a traction power of 42kW. Recalling that the maximum DC fast-charge power level for the Leaf is 44kW, these two power levels match quite well. This suggests that the Leaf battery thermal management system is capable of handling roughly this amount of *average* battery power[9]. It is a similar story for the Renault Zoe: Its top speed is 140km/hr, requiring approximately 35kW average traction power while it has a maximum charge level of 43kW.

However, if we were to increase the charge rate of the vehicle much beyond its average traction power, then the battery cooling would be dictated by charging requirements rather than traction requirements. This may adversely affect performance and cost because the thermal management system and wiring will be oversized for normal driving.

Therefore, despite the fact that DC power levels increase in the new DC Combo standard (see table 1.2), future EVs may not be designed to utilize it anyway. Rather, a charging power level of 30-50kW matches well with the maximum average traction power, which in turn matches well with AC charge levels and hence advocates the use of AC fast-charging:

> AC fast-charging argument #2:
> Limited average battery power
>
> The power levels offered by AC fast-charging (43kW EU/52kW US) match well with the maximum average traction power for many EVs. Thus, additional cooling and component requirements are avoided when designing an EV for charging at these power levels.

---

[9]Note it is generally easier to cool a vehicle during driving with natural air flow. This suggests charge rates may be slightly lower than the average traction power.

	Connector or outlet	DC power	AC power	Est. Price	Weight
Report EVSE	Conn. Type 2	-	43kW	2000 €	10kg
Bosch PowerMax	Conn. Type 1	-	7.2kW	500 €	9kg
RWE eSTATION SMART	Outlet Type 2	-	2x22kW	6000 €	42kg
RWE eBOX	Outlet Type 2	-	1x11kW	600 €	10kg
Electrodrive	Outlet Type 2	-	1x22kW	1000 €	5kg
Schneider EVLink	DC CHAdeMO	50kW	-	25000 €	600kg
ABB Terra 52	DC CHAdeMO Outlet Type 2	50kW	1x22kW	25000 €	600kg
Efacec QC50	DC CHAdeMO Outlet Type 2	50kW	1x43kW	25000 €	800kg
Eaton DCQC	DC CHAdeMO	20-50kW	-	25000 €	350kg

Table 1.3: Some AC and DC charging stations and their supported charge rate

Some scenarios have not been considered in above discussion. For example, if an EV is charged in colder weather, then it may support very fast charging until it reaches a critical temperature. However, this depends completely on the powertrain design, so to figure this out would require more detailed analyses on specific powertrains, which is outside the scope of this discussion.

Furthermore, high-performance EVs with higher battery capacities and rated traction powers, like the Tesla Model S, have the same trade-off, but at a much higher power level. The Tesla Model S has a top speed of 210km/hr, which corresponds to an average traction power of around 100kW. Correspondingly, the battery is rated for this power, and the charging can be boosted to similar levels. The Tesla DC fast-chargers known as Superchargers achieve up to 120kW in charging power.

1.3 AC versus DC fast-charging

Unquestionably, the battery operates with DC whereas the electric utility grid operates with AC. Consequently, a conversion between the two has to take place when power is transferred between the battery and grid. The question is now: Where should the AC-DC conversion occur?[10] To make a fair comparison, we assume in this section that DC and AC fast-chargers operate with similar power levels, around 50kW or less. Specifically, Tesla stands out with DC power levels of up to 120kW.

With DC charging stations, the AC-DC conversion takes place in the station itself, off-board the vehicle, whereas AC charging stations transfer grid AC power directly to the vehicle's on-board converter. In other words, an AC charging station does not require power conversion, whereas DC charging stations require power electronics to convert AC to DC, which adds to the charging station's cost, weight and complexity. An overview of charging station powers, prices and weights is seen in Table 1.3[11].

---

[10]This section requires little knowledge on power electronics and grid construction. For more elaborate technical discussions, e.g. the reason why DC charging stations are expensive, see the subsequent chapters.

[11]The information found in the table has been gathered from vendors' websites. The estimated price excludes VAT, installation and grid connection. The prices for the DC chargers are based on

---

AC fast-charging argument #3:

AC charging stations are cheap to build

AC charging stations require fewer components because no AC to DC conversion power electronics is required, and they can therefore be made small, light and inexpensive.

Many DC charging stations weigh between 300kg and 800kg, requiring elaborate planning and several people for installation. This increases installation costs.

AC fast-charging argument #4:

AC charging stations are cheaper to install

The smaller size and weight of an AC charging station make it easily installed. AC charging stations can be wall-mounted to further reduce installation costs.

1.3.1 Flexibility

Typically, AC charging stations tend to be rated for lower powers than DC charging stations due to the generally lower rated AC onboard chargers (Table 1.1). However, it is easy to scale an AC charging station to support higher power levels, because the AC charging station does not need AC to DC power conversion. An AC charging station usually has one or a few contactors for shutting off power to the vehicle, but these contactors are found as relatively inexpensive off-the-shelf components in most electronics shops, also for high currents up to 63A. See [44] and chapter 3 for an example of building an AC charging station. Hence, AC charging stations can be designed for any power level up to its rated maximum (43kW EU/52kW US), and cost of an AC charging station does not scale with power level.

In some cases, the rated power cannot be supplied by the grid. For example, households may only support 16A connections, or a parking lot with many charging stations cannot charge all connected EVs simultaneously. Therefore, it is necessary to derate the charging level in some situations. A practical algorithm for sharing available power at a site between AC fast-charging stations is presented in section 3.6. However, with DC charging stations, it is much more difficult to share a grid feeder, because it immediately defeats the purpose of a DC fast-charger to limit its charge level. Considering the price point of a DC fast-charging station, it is only feasible to place it at locations where the grid is strong enough to support the maximum charge level for all connected vehicles, at all times[12].

---

a report from the Danish Energy Agency [16]. Installation and connection may double or triple the price of a DC charger.

[12]With DC charging, it may be an option to provide battery backup at the site to level out the grid power draw, but this significantly adds to cost.

AC fast-charging argument #5:

AC charging stations are flexible in power

The price of an AC charging station does not scale with power supply capability, and AC charging stations are hence ideal for charging at different power levels, depending on user preferences and grid constraints.

Being able to charge at many power levels will support all types of cars, including PHEVs. Owners of PHEVs will rarely use DC fast-chargers, because the point of owning a PHEV is to not have to charge en-route where most DC fast-chargers will be installed. However, PHEV owners still want a quick charge on the battery once they arrive at the destination.

AC fast-charging argument #6:

PHEVs prefer AC charging

PHEVs are rarely charged at en-route locations with DC chargers. Fast-charging PHEVs is fully supported by AC fast-charging stations.

1.3.2 Batteries and DC charging stations

A DC charging station is also known as an "off-board" charger, which rightfully indicates that the battery charger is physically separated from the battery it charges. The battery charger is often made by a different manufacturer[13] than the battery and its battery management system (BMS). With an increasing number of battery chemistries as well as an increasing number of DC charging station manufacturers, the compliance matrix becomes quite large. Obviously, this can be solved by adhering to strict standards (CHAdeMO and IEC62196-3 defines these), but there is still a risk that compliance issues arise. Compliance must be ensured both in communication protocols on all layers and power transfer (correct voltage, current, noise level, fault handling).

Furthermore, by separating the charger from the battery, the EV manufacturer is effectively locked to a certain architecture (be it CHAdeMO, the IEC62196-3 DC standard, or others). This may restrict future innovation within battery and powertrain technology. For example, the CHAdeMO DC charging standard allows voltages up to 500V, and it would therefore be difficult for an EV manufacturer to advance to newer battery technologies operating at higher voltages. With AC charging and an onboard converter, the EV manufacturer may decide the charging and battery architecture arbitrarily.

---

[13]Tesla is, as with much else, an exception to this, because they make both EVs and DC chargers

---

AC fast-charging argument #7:

An onboard charger knows its battery

An offboard charger cannot know the battery it charges and must be informed using high-level communication how it is supposed to deliver power. This introduces a risk of interoperability issues, and it may restrict future powertrain innovation. An onboard charger is built and tested for the battery it charges and is thus not exposed to these issues.

Usually, a Lithium-ion battery is charged using a constant current from 0% SOC to approximately 80-90% SOC. Hence, it is relatively simple to charge the battery in this region, which may limit the aforementioned interoperability issues. However, this also means that most DC charging stations stop charging at 80% SOC because the charging power must be lowered, which makes the DC station inappropriate for this type of charging.

AC fast-charging argument #8:

On-board chargers can charge a battery to 100% SOC

Since on-board chargers also operate during the constant voltage region, the EV battery is charged to 100% SOC without intervention.

1.3.3   Charging station to EV ratio

A rough estimate for the total number of charging stations needed can be found by considering the ideal ratio between charging stations and EVs.

Most EV owners will have a charging station at home. Also, many workplaces will offer a charging station for their employees that own an EV. Finally, charging stations will be placed at strategic public places along roads or at public parking lots[14]. Charging stations will be placed when there is a long distance to the next charging station, or when the charging station can serve many vehicles en-route. Private companies may also invest in charging station to attract EV customers to their business, e.g. at hotels, shopping malls or highway restaurants.

Therefore, there will be *at least* one charging station per EV (likely at home), but up to three charging stations per EV (at home, at work, en-route/public space). This is, as mentioned, a very rough estimate, but it still suggests that there is a considerable need for small, adaptive and cheap charging stations to enable this vast increase in infrastructure. With the goal of reaching 20 million EVs in 2020 [18], the projected number of charging stations range between 20 and 60 million units.

---

[14]Unfortunately, charging stations are often seen to be installed at rather random locations depending on company CSR profiles.

AC fast-charging argument #9:

Enables vast increase in infrastructure

AC fast-chargers being small, light, cheap and adaptive enables
the required increase in infrastructure to support future EV fast-
and slow-charging.

China is aiming for a 1.25 non-residential charging station to EV ratio in 2020
[18]. Including residential charging stations, this ratio could increase to 2.25, again
suggesting that charging stations must be cheap and manageable.

1.3.4 Onboard converter

Most EV manufacturers do not develop higher power onboard chargers. One reason
is that it becomes costly to design power electronics rated at a power level above
3-6kW when constructing the charger as a separate unit. The chargers rated for
more than 3kW are also said to add weight and take up more space in the vehicle.
This is unfortunate when EVs must be designed for high efficiencies in order to
drive as long as possible on a single charge.

Therefore, instead of using high-power onboard chargers, car manufacturers rely on
DC offboard chargers to provide fast-charging. This is a cheap and convenient way
for the manufacturer to allow fast-charging, but it does not take into account the
additional requirements and cost of DC infrastructure. The price of a DC charging
station is typically 10-40 times more than an AC charging station providing a similar
amount of power (see table 1.3).

As mentioned in the introduction, there is a way to avoid the issue of added vehicle
cost, and still use an onboard charger. The idea is to use the already available
traction electronics onboard the vehicle that is used to drive the electric motor. In
this way, the traction electronics are reused for charging purposes. This feature is
explored in chapter 2. Currently, the California-based company AC Propulsion and
Renault uses this technology. Renault estimates that in the 43kW capable Renault
Zoe EV, the cost of charging components is only around 150 €[15].

To estimate the possible infrastructure savings, let us say that 10.000 fast-charging
stations are to be deployed globally. Assuming a DC fast-charging station costs
25000 € and an AC fast-charging station costs 3000 €, the infrastructure savings of
using AC fast-charging stations totals 220M €.

AC fast-charging argument #10:

Low total system cost benefits users

AC charging stations are cheap mainly due to their simplicity. On-
board fast-chargers can be made inexpensively with appropriate
technology. Hence, AC charging lowers overall system cost, which
benefits EV drivers and the EV industry.

---

[15]Noted from Renault presentation, april 2012

Another interesting feature of the power electronics in typical onboard fast-chargers is that it theoretically supports charging from DC sources as well: A three-phase converter can be used as a DC-DC full-bridge converter (see section 2.2). Therefore, in the (unusual, but not unthinkable) case that an onboard charger is connected to a DC charging station, it could still be able to charge off of it. This has seemingly not been implemented in any vehicles yet, and must be researched in more detail before it can be realized. Also, the setup is slightly less efficient, because it requires yet another power converter in the interface between the grid and battery. However, this may be a way of increasing onboard charge levels beyond the 43kW limit set by the Type 2 connector. It also opens possibilities of doing vehicle-to-vehicle or battery-to-vehicle charging using DC in situations where a supporting grid is not available.

Hence, the onboard converter allows for a universal charger design, able to charge from any single-phase or three-phase grid outlet[16] or DC fast-charger, and which can be used all over the world.

1.3.5 Comparing AC and DC power

It is important to emphasize that there is no inherent advantage in transferring power with DC rather than with AC for EV charging[17]. After all, DC charging stations get their power from the AC grid.

The power transferred through balanced three-phase AC power lines is constant, as with DC[18]. The difference is that three-phase AC transfers constant power over three wires whereas DC uses two. This means that the current per wire is less using AC, but the total wire losses are equal for AC and DC power transfer. A simple example to show this has been set up in appendix D. The example also shows that if the neutral wire is not included in a three-phase system, then AC power transfer has lower losses per cross section of wire than DC.

In terms of EV charging, the neutral will usually be included because we should also be able to charge EVs with single-phase chargers, which use one phase and the neutral for the return current. The point is, however, that AC features either similar or lower losses compared to DC, not more.

AC fast-charging argument #11:

AC transfers power as well as DC

DC and single-phase AC transfer power over two wires. Three-phase AC transfers constant power over three wires with a lower current per-wire. There is no inherent advantage for either type of power transfer for EV charging.

---

[16]See the discussion on four-leg converters in section 2.6.4.

[17]Assuming grid frequency AC in conductors with a diameter smaller than the skin depth, which means wire cross section should be less than 66mm^2

[18]This is shown in section 2.7.2

1.4 Why Fast Charging?

As mentioned in the introduction, one reason for showing interest in fast charging is its potential for mitigating range anxiety. When drivers can charge their vehicles in 30-60 minutes then longer trips are made possible because EVs can be charged en-route without inconvenient waiting times.

To determine the actual required daily vehicle range, real-life studies such as [60] are essential. This study treats per-second GPS measurements of representative driving behavior for around 500 gasoline vehicles (not electric vehicles) in an area surrounding Atlanta, Georgia in the calendar year 2004. This area has the second highest daily vehicle distance traveled per capita in the US, and the average daily driving distance is 72km. To compare, the average daily driving distance in Denmark is 40km [28]. These numbers suggest that this particular study is rather conservative and could serve as an example of a worst-case scenario for EV rollouts. However, the average daily driving distance is not sufficient when determining the required EV range. The maximum daily distance driven at any time must also be taken into account because an EV driver should be able to use their vehicle as much as possible.

Therefore, the study extracts the maximum daily distance driven for all vehicles over the course of the year. The cumulative distribution of this dataset is depicted in fig. 1.3. For example, it can be seen that 8% of vehicles never drive more than 100km and 25% never drive more than 250km. Correspondingly, an EV with a range of 250km could replace 25% of the vehicle fleet, without ever requiring an alternative means of transportation for the users. It is also seen that around 10% of the users in the study drive more than 1000km in a day during the year, suggesting it requires a considerable range to cover all driving needs at all times.
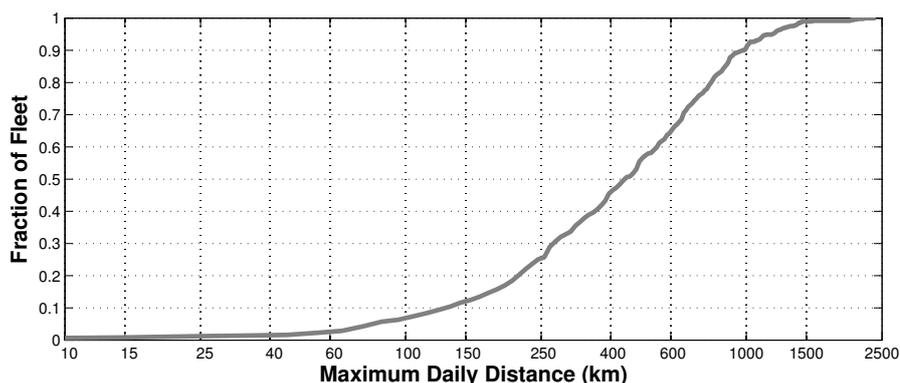
Figure 1.3: Cumulative driving distance

With charging times below around 2-4 hours, an EV can be charged at its destination before it returns to its over-night charging spot. The destination could be a workplace, shopping mall or some sort of public space. This effectively doubles the range for an EV. Returning to fig. 1.3 it is evident that this increases the possible EV penetration considerably: For a 250km range EV, its effective range is 500km with destination charging, corresponding to a possible EV fleet penetration

of around 50%.

With charging times below 30-60 minutes, an EV can be charged both at its destination or en-route without inconvenient waiting times. This makes it possible to travel any distance, and potentially also serving the users that require up to 1000km of driving a day or more. Thus, fast-charging technologies are paramount in mitigating range anxiety and increasing EV penetration.

Batteries are expensive, and they constitute a considerable fraction of the vehicle cost (e.g. around 50-60% for the first Nissan Leaf [54]). At the end of 2012, batteries were priced at approximately $500 per kWh [42], going down from $1000 in 2008. In 2020, it is projected that batteries will cost $300 per kWh, which is noticeably less, but batteries are still quite expensive. However, fast-charging can increase the perceived range of EVs, because they can be recharged quickly when the battery runs low. Furthermore, power electronics for onboard fast-chargers is relatively cheap (see chapter 2). Therefore, in order to lower EV cost, smaller batteries are preferred if cheap and abundant fast-charging equipment can make up for the missing capacity. Obviously, the batteries need to have a certain size to avoid inconvenient charging, but the point is that the trade-off between battery size and charge power level has to be considered.

Very often, potential buyers ask how long it takes to charge an EV[19]. While it is in many cases sufficient for an EV driver to use slower over-night charging, it sounds comfortable that they can fast-charge their vehicle so the charge time is less than 30-60 minutes. This selling point must not be underestimated, and surveys show that buyers are willing to pay for this attribute [41].

As stated, fast-chargers extend vehicle range. Long trips are often driven on highways, and it is usually a sensible decision to put fast-charging equipment alongside these types of roads. However, EV drivers want to be able to go anywhere, not only along highways. This raises the need for providing fast-chargers on remote locations, which may not be used very often. These stations serve as "range assuring" rather than "range extending", and it is vital that the installation and maintenance cost of the charging stations is minimal, because they will otherwise not be put up on private initiative.

AC fast-charging argument #12:
Range assurance

At remote sites, fast-chargers are needed to mitigate range anxiety but they will be used rarely. Only AC fast-chargers can provide a profitable business case for this purpose.

1.4.1 Other range extending improvements

Other ways of extending range deserve mentioning, but they will not be the main focus of this report. The following improvements are all seen as supplements to

---

[19]This question may be somewhat difficult to answer in general, because it depends on EV battery capacity and charge level (so asking about these would be more enlightening).

conductive charging, and are as such not direct competitors to AC or DC fast-charging. The following methods extends EV range:

1. Increasing battery size.

2. Improving battery technology.

3. Improving EV efficiency.

4. Adapting other charging methods, such as wireless charging or battery swap.

Increasing the battery size is indeed possible, and Tesla offers an 85kWh battery in the Model S. However, this solution will inevitably increase cost and is thus restricted to higher-end (luxury) EVs. Furthermore, the increased volume and weight of the battery impose certain requirements on the size and frame of the car, which makes it difficult to use in compact cars and other smaller cars that many people find attractive, especially in Europe.

Improving battery technology is a very desirable solution: The higher energy density the better, and this will unquestionably be a part of the long-term solution. However, while the research within battery technology is highly active, it does not seem to be able to provide short-term breakthroughs that can considerably increase energy density compared to lithium-ion and other existing solutions. An interesting technology to follow in this context is lithium-air based batteries, which may be able to increase energy density between 5-15 times compared to lithium-ion [6].

Increasing the efficiency of EVs implies improving aerodynamics, rolling resistance, power electronics design and introducing the use of heat pumps for heating the cabin efficiently. Increasing efficiency is a very important part of extending range, since a gain in overall vehicle efficiency can lead to a considerably increased range, and the introduction of heat pumps will be one of the significant improvements that extends range in future EVs, especially in colder climates. It can be noticed from 1.1 that there are quite noticeable differences between EV driving ranges per kWh of battery capacity, which is directly attributable to the efficiency of the vehicle (given that the driving ranges are measured similarly). The 2013 Nissan Leaf increased its range 24% over past year's model due to the use of a heat pump.

Non-traditional charging schemes aim at solving the range anxiety problem. Wireless inductive charging technology is being pushed by Qualcomm and Bosch. Qualcomm imagines different configurations of inductive charging, where stationary charging and dynamic charging (that is, charging while driving) are possible. Bosch sells after-market inductive charging kits that are currently being sold for select EVs, including the Nissan Leaf, with a charge rate of 3.3kW.

Tesla's Model S is capable of swapping the battery, but it is still unclear if they will pursue this technology or not [14]. Battery swapping was used by Better Place until they went bankrupt [23]. Better Place cooperated with Renault who produced the Renault Fluence ZE that supported swapping out its 22kWh battery. However, among other issues, the single car model offered by Better Place was likely not sufficient for their potential customers.

1.5 Vehicle to grid

The idea of vehicle to grid (V2G) technology is to use the energy storage in EV batteries to complement the operation of the electric grid. This is accomplished by controlling EV charging and discharging in real time, that is, bidirectional power flow is a prerequisite for this technology, as indicated by its name. The load in the grid is known to fluctuate over short periods of time, but with an increasing amount of intermittent renewable generation such as wind and solar, generation is fluctuating as well. For that reason, there is an increasing need for regulating the production and consumption quickly and precisely, which can be achieved with V2G-enabled EVs, which is one type of a grid integrated vehicle (GIV).

There are several ways in which GIVs can complement grid operation. One is to participate in one of the many electricity markets. The baseload power markets are generally unattractive, because in these markets, centralized power plants (nuclear, hydro, coal, etc) produce cheap electricity based on long-term contracts. This is difficult to match with batteries due to a relatively low energy density in current EV batteries. Furthermore, it is possible to use GIVs to buy electricity throughout the day when it is cheap and sell it when it is expensive, known as energy arbitrage. This is a simple market for GIVs, but is not yet possible since neither US nor Danish grids offer time-of-use billing[20]. However, even if these markets were available, they would likely not become very profitable for GIVs.

The most profitable markets right now are the ancillary services and regulation markets that provide a capacity payment for available power, plus a payment for delivered energy. These markets will typically only require GIVs to deliver power in shorter periods (e.g. less than an hour), meaning that the energy limitations of batteries are no longer a problem. Instead, it is required to deliver power almost instantly when it is requested, which is completely acceptable because it is in the very nature of an EV to vary its power output. Furthermore, GIVs can provide power in two directions, and can thus participate in the up- and down-regulation markets simultaneously.

Several of these types of markets exist in Denmark, depending on which area the service is provided (Denmark is parted in two independent asynchronous grid areas with varying legislation). For example, in western Denmark (DK1) in the primary reserve regulation market, 27MW of regulation capacity was required in 2011. In mainland Europe the required regulation capacity was 3000MW [32]. This type of regulation service must be provided within 15 seconds of the request but runs for maximum 15 minutes. It is a perfect scenario for a fleet of GIV to bid into this type of market.

Calculations on the economics of GIVs have been accomplished before, e.g. in US [48], which identifies profitable business cases. Basically, the net revenue is found from the capacity payment plus the payment of the actual delivered electricity minus the cost of providing the service. The cost is related to capital cost, inefficiencies and battery wear. The battery wear is found to be limited due to the small amounts of energy exchanged, but it depends on the battery chemistry and its cyclability[21].

---

[20]In Denmark, this may be possible from October 2014 [34].
[21]For example, the LiFePO$_4$ battery chemistry manufactured and sold by e.g. the company

As a simple example, we can calculate the possible revenue from the primary reserve capacity payment for up-regulation in Denmark. In DK1 in 2013 (January until ultimo July), the average capacity payment for each hour was 31.49 € per MW [30]. This corresponds to 0.03149 € per kW. Assuming we own a GIV with a 43kW bidirectional charger, and it is parked and available for V2G services 12 hours a day on average, the revenue r accumulated over one month is

$$r_{month} = 43\text{kW} \cdot 0.03149\text{€}/\text{kW} \cdot 16\text{hr} \cdot 30\text{days} = 487\text{€} \tag{1.3}$$

Over the course of a year, this vehicle would generate a revenue of 5850 €. This is a considerable amount of money generated just by having a car parked and plugged in. Notice that with capacity payments, the revenue is directly proportional to the charge rate: The revenue is halved with half the charge rate. Hence, the V2G technology depends highly on fast-charging and fast-discharging EVs. Off-board DC chargers cannot be used with this technology, because vehicles will not be parked near DC chargers for longer periods of time (e.g. 12 hours as assumed in above example).

AC fast-charging argument #13:
AC fast-charging enables V2G

When charge (and discharge) power levels are increased, the revenue generated from V2G services increases correspondingly.

Naturally, there are tasks to be addressed with V2G before it is practically realizable. First of all, there are limits to the minimum bid size on most regulation markets, so a fleet of a certain size has to exist. In DK1, the minimum bid size is 0.3MW and thus at least 7 cars with the power capability from the example above are needed (more cars will be needed due to faults or unpredictable behavior). This means a third-party player must act as an aggregator and forecast the amount of vehicles available at a certain time, and also take driver's needs into account. Secondly, the aggregator has to communicate with the power electronics onboard the vehicle, e.g. to know the battery SOC and start the regulation service when needed. Finally, the GIV must be safe to grid faults, and also disconnect in case the vehicle has become electrically islanded. Most of these tasks have been addressed and solved at the University of Delaware [3, 68].

Many other types of ancillary services can be provided from a bidirectional on-board EV charger[22]. For example, in the US there is a peak demand charge, which is billed when a customer supersedes a predetermined power level for more than 15 minutes in a month. A V2G vehicle can lower this demand charge, and thus provide a directly measurable saving for the customer. A similar saving could be achieved in Denmark, if one or several V2G EVs could avoid a transformer upgrade.

EVs could work as uninterruptable power supplies (UPS) during power outages, avoiding the need of a gasoline-based generators. This is also known as vehicle-to-load (V2L). Furthermore, an EV could charge another EV, known as vehicle

---

A123 Systems is extremely durable, at the expense of a somewhat lower capacity. See also [69].

[22]Most are explored in the Nikola project at DTU

to vehicle (V2V). In this way, there are several possibilities of providing power to various loads under varying terms. Therefore, the bidirectional capabilities in an EV has been known as V2X, to emphasize the fact that the vehicle can provide power to any load that should require it[23].

AC fast-charging argument #14:

Bidirectional chargers enable ancillary services

If a charger is constructed with bidirectional power flow capability, many types of services can be provided, each of which has value for specific customer segments and use cases.

1.6 AC versus DC conclusion

Today, it seems established that DC charging stations provide fast-charging for EVs. However, the reason is not so obvious when comparing AC and DC fast-charging technologies. AC can with standardized cables charge up to 43kW (EU) and 52kW (US), and the CHAdeMO charging stations being installed provide between 20 and 50kW. Hence, with current technologies, AC and DC charging stations provide similar power levels. At the same time, AC charging stations are much cheaper and smaller. Furthermore, vehicle to grid and ancillary services can greatly aid to the business case for EVs, and these technologies rely on onboard fast-chargers and AC charging stations. Therefore, expanding EV infrastructure with AC fast-charging stations seems like the most feasible approach.

A few DC charging stations provide a separate AC outlet. However, it does not make sense when a 50kW DC charging station only provides a 22kW AC connector. Certainly, a 50kW DC charging station will be able to provide 43kW AC, because it gets its 50kW power from the AC grid anyway. This is likely caused by DC charging station manufacturers trying to protect their investments in DC solutions.

There is a use case for unidirectional DC fast-charging stations when power levels go above 50kW. In that case, larger, long-range EVs can be fully charged within an hour or less. For example, this is the case for the 500km range Tesla Model S which uses the Tesla DC Superchargers. Also, fewer charging stations are needed for this class of EVs[24]. Existing AC solutions cannot compete with power levels above 50kW. It has not yet been investigated if it is technically possible to fast-charge with AC much beyond 63A per phase with onboard chargers. Anyhow, the main problem is that EV standards do not allow higher AC currents at this point, which kills initiatives to that end.

---

[23]The V2X term has, unfortunately, at conferences also been misused by auto manufacturers to actually mean vehicle to load, that is, not including neither V2V nor V2G.

[24]In Tesla's case, since they manufacture their own charging stations and provide power for free, they have an interest in limiting the number of charging stations while extending their vehicle range as much as possible

Chapter 2

Integrated motor drives and battery chargers

2.1 Introduction

This chapter explores the concept of *integrated motor drives* (IMD). The main focus is how to apply a three-phase motor drive for charging purposes. The chapter explores power electronic topologies, challenges in practical realizations, space vector modulation and converter control.

Almost all electric motors for high power applications are constructed as three-phase machines. This makes it an inherent requirement for EVs to carry a three-phase motor drive that converts the battery DC to three-phase AC for the motor. Coincidentally, the electric grid is worldwide constructed with three phases, similar to motors and motor drives. Since an EV must interface the grid for charging and its motor for driving, it is a logical step to combine these interfaces into one physical unit because they basically consist of the same components. Note also that conductive charging and driving never occur simultaneously, so it makes sense to utilize the available power electronics as much as possible. Eventually, integrating the traction and charging components results in lower price and size of the onboard electronics.

A simulation is developed to show how a three-phase motor drive is similar to a three-phase grid converter, and how this can be used for charging a DC source such as a battery. The simulation also shows how to control a converter for various types of power exchange, such as reverse active power flow (DC to AC), controlling reactive power (emit and consume), grid-forming modes, and unbalanced loads. It turns out that single-phase charging is a special case of an unbalanced three-phase load (that is, only one phase is loaded) which is therefore treated implicitly.
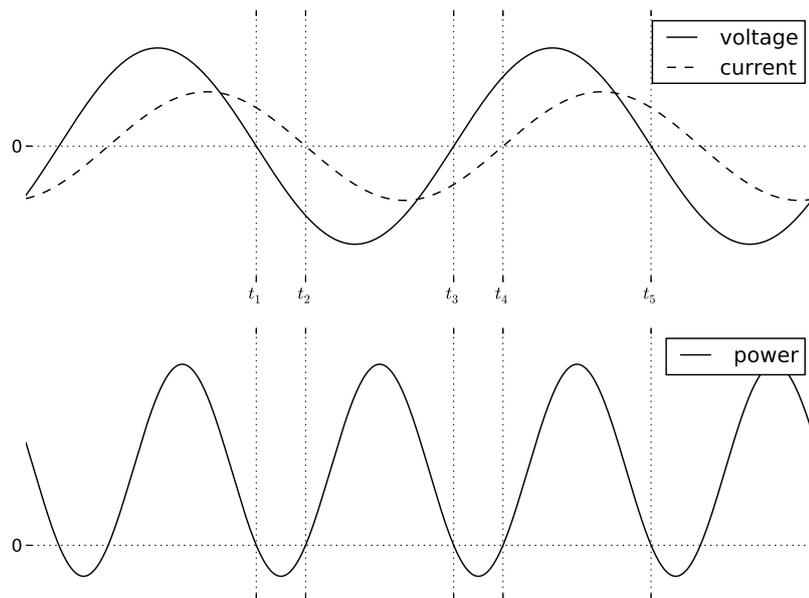
Figure 2.1: Voltage, current and active power in AC motor for a single phase

2.2   Motor drive power electronics

The basic requirements of a motor drive is found in this section. Fundamentally, a motor is an inductive load due to the generation of magnetic fields. This implies that the current lags the voltage, as exemplified in fig. 2.1. The figure shows the ideal waveforms of one of three phases, but the other two phases would show similar behavior with a 120 degree phase shift. The corresponding single-phase active power is shown at the bottom of the same figure. Four distinct time periods can be identified based on the sign of the voltage and current. In the time period between t_1 and t_2, the current is positive and the voltage is negative. The active power being the product of the two yields a negative value. Between t_2 and t_3 both voltage and current are negative, yielding a positive power. Between t_3 and t_4 the voltage is positive and current is negative, again yielding negative power. Finally, between t_4 and t_5 the voltage and current are both positive resulting in a positive power. This pattern repeats itself continuously. As a side note, it is seen that power has double frequency compared to the voltage and current waveforms. The average power is positive.

It is evident from the figure that power becomes negative when the voltage and current have opposite signs. Therefore, a motor drive must be bidirectional by nature to provide reverse (negative) active power during these periods. Furthermore, the drive output current and voltage must be provided in all four (v, i) quadrants, as shown during the four time periods. Furthermore, it is highly attractive in EV applications to use regenerative braking which also requires a bi-directional converter[1].

One common high power converter topology that satisfies these requirements is

---

[1] In this case, the average active power is negative, that is, active power is flowing from the motor to the DC bus
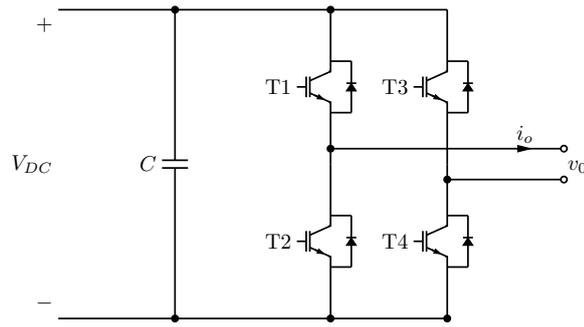
Figure 2.2: Four quadrant bidirectional single-phase converter

the full-bridge converter, shown in Figure 2.2 in a single-phase configuration. This is a two-level bidirectional topology that can be used as a DC-DC buck or boost converter[2] or as an AC-DC converter with proper control. It is seen that the converter consists of two vertically drawn *legs*, each of which has two switches, in this case IGBTs. The IGBTs have an antiparallel diode connected across its collector-emitter terminals. This configuration ensures that the current can flow both ways in each IGBT-diode pair. For example, with a positive current i_o with T1 on makes the current flow in T1. If the current is negative and keeping T1 on, the current flows through the diode connected across T1. This is the case for all four switches, and it means that we can apply a voltage v_o on the output terminals independently of the direction of the output current.

Naturally, the two IGBTs in a leg must not be on simultaneously, or the DC bus will be short circuited. Instead, the switches in a leg are usually operated so that when one switch is on the other is off. The switches between two legs may be operated independently. This yields four possible switch states with corresponding output voltages:

1. T1 on, T4 on (T2 and T3 off): $v_o = V_{DC}$.
2. T2 on, T3 on (T1 and T4 off): $v_o = -V_{DC}$.
3. T1 on, T3 on (T2 and T4 off): $v_o = 0$.
4. T2 on, T4 on (T1 and T3 off): $v_o = 0$.

It is seen that there are two non-zero voltages, which is the reason for denoting this topology as two-level. Since the two switches in a leg are always operated in a mutually inverted fashion, we can denote the leg state as p when the upper switch conducts (and the lower is off), and n when the lower switch conducts (and the upper is off). Using this notation, the generated voltages and the corresponding switch states are shown in table 2.1.

The topology explored so far was applied for single-phase bidirectional loads, whereas the motors in EVs are three-phase. However, the basic requirements to the bi-directionality of the converter are similar. Therefore, adding a switch leg to the topology as shown in Figure 2.3 makes it possible to operate three-phase loads and motors.

---

[2]For higher powers than a conventional buck or boost converter

Switch state	On switches	Output
pn	T1, T4	V_{DC}
np	T2, T3	$-V_{DC}$
pp	T1, T3	0
nn	T2, T4	0

Table 2.1: Single phase full bridge switch states
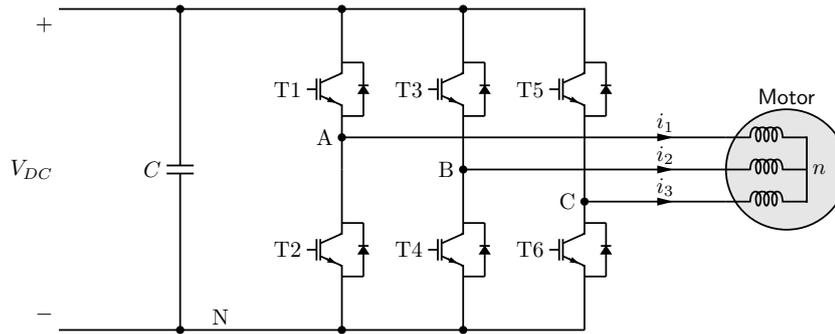
Figure 2.3: Typical three-phase AC motor drive

To operate a three-phase balanced load, it is required to output three sinusoidal voltages on nodes A,B,C (related to node n) with equal amplitude v_o and phase shifted 120 degrees. Assuming the converter is operated in this way, the sum of the voltages is always zero:

$$v_{An} + v_{Bn} + v_{Cn} = v_o \sin\left(\omega t\right) + v_o \sin\left(\omega t - \frac{2\pi}{3}\right) + v_o \sin\left(\omega t - \frac{4\pi}{3}\right) = 0 \quad (2.1)$$

The voltages between each of the nodes A,B,C and the negative DC bus terminal, node N, can be expressed as follows:

$$v_{AN} = v_{An} + v_{nN} \tag{2.2}$$
$$v_{BN} = v_{Bn} + v_{nN} \tag{2.3}$$
$$v_{CN} = v_{Cn} + v_{nN} \tag{2.4}$$

We can take advantage of the relation in eq. (2.1) if we sum eqs. (2.2) to (2.4):

$$v_{AN} + v_{BN} + v_{CN} = v_{An} + v_{Bn} + v_{Cn} + 3 \cdot v_{nN}$$
$$v_{nN} = \frac{1}{3}\left(v_{AN} + v_{BN} + v_{CN}\right) \tag{2.5}$$

Putting eq. (2.5) back into eq. (2.2) we get:

	ppp	nnn	pnn	ppn	npn	npp	nnp	pnp
v_{An}	0	0	$\frac{2}{3}$	$\frac{1}{3}$	$-\frac{1}{3}$	$-\frac{2}{3}$	$-\frac{1}{3}$	$\frac{1}{3}$
v_{Bn}	0	0	$-\frac{1}{3}$	$\frac{1}{3}$	$\frac{2}{3}$	$\frac{1}{3}$	$-\frac{1}{3}$	$-\frac{2}{3}$
v_{Cn}	0	0	$-\frac{1}{3}$	$-\frac{2}{3}$	$-\frac{1}{3}$	$\frac{1}{3}$	$\frac{2}{3}$	$\frac{1}{3}$

Table 2.2: Three phase converter switch states

$$v_{AN} = v_{An} + \frac{1}{3}\left(v_{AN} + v_{BN} + v_{CN}\right) \tag{2.6}$$

$$v_{An} = \frac{2}{3}v_{AN} - \frac{1}{3}\left(v_{BN} + v_{CN}\right) \tag{2.7}$$

This can be done likewise for eqs. (2.3) and (2.4):

$$v_{Bn} = \frac{2}{3}v_{BN} - \frac{1}{3}\left(v_{AN} + v_{CN}\right) \tag{2.8}$$

$$v_{Cn} = \frac{2}{3}v_{CN} - \frac{1}{3}\left(v_{AN} + v_{BN}\right) \tag{2.9}$$

Now the voltages on each phase can be found based on the switch states. The states will again be denoted p when the upper switch conducts, meaning this leg applies a voltage v_{DC}, and n when the lower switch conducts, meaning this leg applies a voltage of zero. Having three legs with each two states, there are a total of $2 \cdot 2 \cdot 2 = 8$ switching states. For example, in state *pnp*, by inserting into previous equations:

$$v_{An,pnp} = \frac{2}{3}v_{DC} - \frac{1}{3}v_{DC} = \frac{1}{3}v_{DC} \tag{2.10}$$

$$v_{Bn,pnp} = -\frac{2}{3}v_{DC} \tag{2.11}$$

$$v_{Cn,pnp} = \frac{2}{3}v_{DC} - \frac{1}{3}v_{DC} = \frac{1}{3}v_{DC} \tag{2.12}$$

This has been carried out for all eight switching states in table 2.2, normalized by v_{DC} for brevity. Notice that there are only six active switching states that generate non-zero voltages on the output, and there are two zero states (ppp,nnn).

The voltages in the six active switching states for each phase are shown graphically in fig. 2.4. The bottom graph shows the line-line voltage between phases A and B. Sinusoids are drawn as well, which illustrate how an appropriate switching scheme in the three-leg converter is able to generate three-phase sinusoidal voltages.

A few important facts can be noticed from fig. 2.4:

- The frequency of the fundamental sinusoid can be changed arbitrarily by cycling through the switching states at different rates. Notice that two switching cycles are shown in the figure.
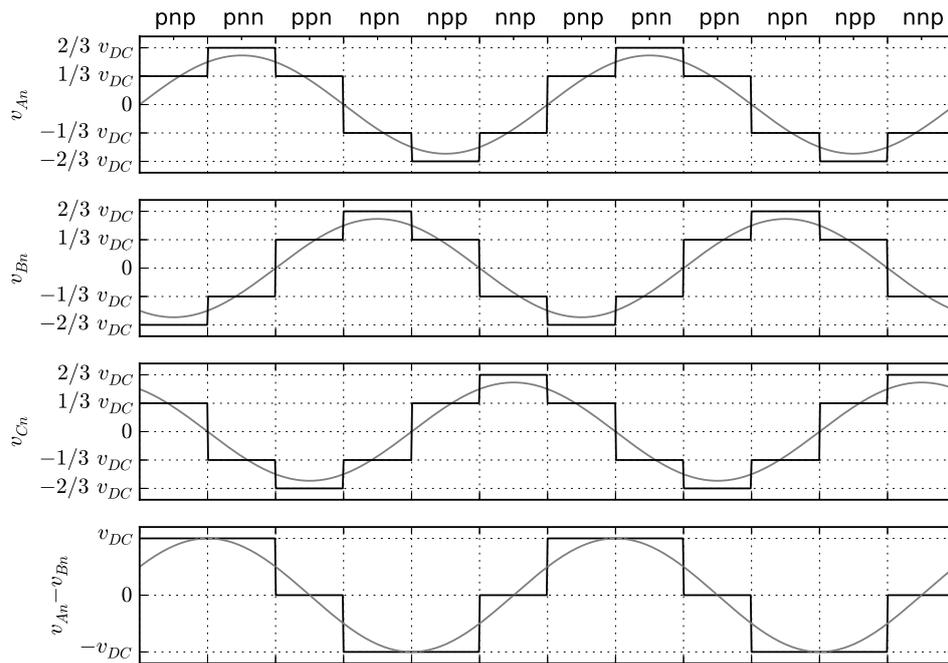
Figure 2.4: Switching scheme for generating three-phase voltages

- The switching scheme shown is known as square wave modulation. Clearly, the sinusoid is tracked relatively poorly, and hence many harmonics would be generated by this switching scheme. Therefore, space vector modulation can be used to reduce harmonics and improve power factor, which is shown later.

- The line-line voltage square wave has two non-zero levels, which shows this topology is a two-level converter.

- The peak line-line amplitude is v_{DC}, which is also the amplitude of the sinusoid drawn in the bottom graph. Correspondingly, the amplitude of the line-neutral sinusoids is $\frac{v_{DC}}{\sqrt{3}}$. Note that the sinusoids drawn are not the fundamentals of the square waves, but rather indicate the maximum theoretical voltage that can be generated regardless of modulation method. Therefore, it is evident that *the peak line-line AC voltage is always equal to or less than the DC voltage.*

- The zero states are not shown in the figure. However, the zero states are used with other types of modulation when the output AC voltage should be lower. Due to the fact that there are two zero states, it is possible to choose the zero state that entails the lowest switching loss.

Hence, with the bidirectional two-level three-leg drive shown in fig. 2.3 it is possible to drive a three-phase motor with varying frequency and with a line-line voltage up to the DC voltage. This is the basic prerequisite of any motor drive, regardless of motor type. Control methods for motors will not be discussed in this report, and it will be assumed that the shown three-leg drive is capable of driving any type of three-phase EV motor, including the two most commonly used, induction and synchronous motors. On motor control, see e.g. [35].

2.3 Grid connected converters and power factor

This section will explore grid-connected power converters, and show how a three-leg motor drive can be applied for EV charging applications.

It is generally desirable to draw a sinusoidal current from the grid [56]. Deviations from a sinusoidal current implies the generation of harmonics, which has several disadvantages, including interference with sensitive electronics equipment and it lowers the amount of usable (active) power that can be drawn from the grid. The *power factor* quantifies the ratio between active power and the apparent power. In other words, it expresses the effectiveness of the power transfer and it ranges from 0 to 1, where 1 indicates perfect power transfer and 0 no power transfer. The power factor is given by [56][3]:

$$PF = \frac{P}{S} = \frac{I_1}{I} \cdot \cos(\phi_1) \tag{2.13}$$

Here, P is active power and S is apparent power. The power factor is seen to be composed of two terms: The first term $\frac{I_1}{I}$ is known as the distortion factor and it is given by the ratio of the fundamental component of the current I_1 to the total current I. Hence, any non grid-frequency current lowers this number and hence the power factor. It can be related to the current total harmonic distortion (THD):

$$\frac{I_1}{I} = \frac{1}{\sqrt{1 + THD^2}} \tag{2.14}$$

Here, THD is defined as the square root of the squares of the non-fundamental current components divided by the fundamental current:

$$THD = \frac{\sqrt{\sum_{n=2}^{n} I_n^2}}{I_1} \tag{2.15}$$

It is evident that THD should be low to achieve a high power factor.

In the second term of eq. (2.13), $\cos(\phi_1)$, the phase shift between the fundamental voltage and current is denoted ϕ_1. The term is denoted *displacement factor*. A value different from 0° lowers power factor, and at -90° or +90° the power factor is zero, meaning no active power is transferred (only reactive power). In this case, there is not necessarily any current harmonics. For example, in fig. 2.1 the phase shift is $\phi_1 = 45°$ and the power factor is thus 0.71.

Standards like IEC 61000-3-2 and IEEE 519 pose requirements on the acceptable THD levels and the levels of the harmonics [33]. Thus, these standards address the distortion factor, and not the displacement factor. Therefore, the power factor

---

[3]This assumes a grid without voltage harmonics
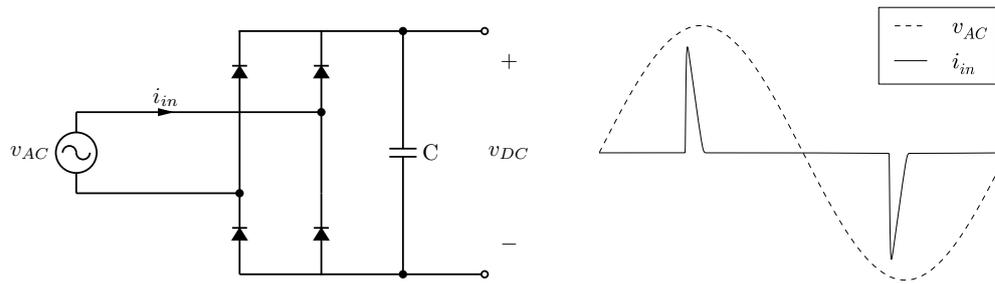
Figure 2.5: Single phase rectifier with waveforms

alone cannot generally be used to set requirements on grid connected equipment, because some applications have inherent low power factors, like motors connected directly to the grid. However, equipment with power factors close to unity implies that harmonics are low and the current and voltage are in phase. Thus, unity power factor operation is a desirable goal.

IEEE 519 varies its THD requirements based on the ratio between the short circuit current at the site of the connected equipment (known as PCC, point of common coupling) and the load current of the equipment. Thus, a high ratio means that the equipment draws little current compared to the maximum possible at a site, and a low ratio means the equipment draws a significant amount of current compared to the maximum possible. The maximum current will depend on the local transformer rating and the distance from the transformer to the outlet. The THD requirements range from 5% where the ratio is low to 20% where the ratio is high [33]. Generally speaking, this means that small loads like computer power supplies have weaker restrictions than larger loads like EV chargers, where the THD requirement could be as low as 5%.

Regardless of standards, the power factor is as mentioned a measure of the effectiveness of the power transfer, and this should in any case be as high as possible to utilize available power. Thus, the goal must be to construct an EV charger with unity power factor capability.

One conventional AC to DC rectifier circuit is shown in fig. 2.5. The diodes rectify the sinusoidal voltage into a pulsating DC, and the diodes conduct when the voltage across the capacitor is lower than the instantaneous AC voltage. Clearly, the current contains pulses, which increases the THD considerably. For the current in fig. 2.5, the THD is around 220%, and this circuit is therefore not applicable for anything other than very small loads.

It is easy to lower the THD considerably using inductors and capacitors as filter components, known as passive power factor correction (passive PFC). However, a passive filter solution will never result in sinusoidal current draw, and the converter will thus never reach unity power factor. Instead, an active PFC should be utilized [56], which is shown conceptually in fig. 2.6. The switch T_1 is either a MOSFET or IGBT depending on power requirements. The active PFC circuit is basically a boost converter that is controlled to track the voltage. This ideally results in a sinusoidal current and unity power factor. In other words, the active PFC circuit ideally makes the load look purely resistive.
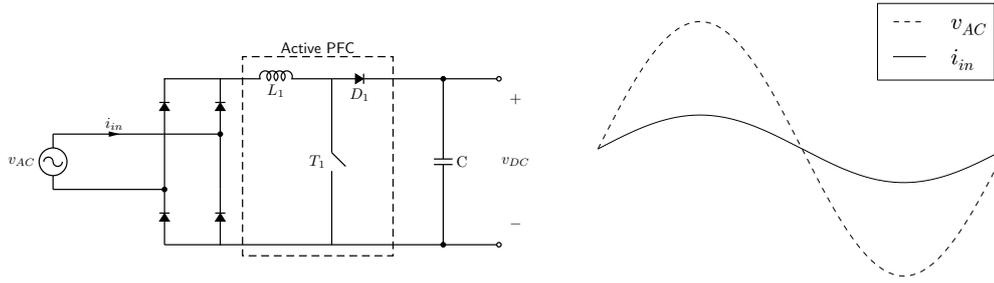
Figure 2.6: Single phase rectifier with active PFC and waveforms

Hence, the topology of the circuit in fig. 2.6 could be used for EV chargers, which is also the case, and reference designs for EV chargers using this topology is found online [1]. As mentioned, the active PFC boosts the voltage, meaning that the average DC voltage will be more than peak AC voltage, which in most of Europe would be $230V \cdot \sqrt{2} \approx 325V$. However, it should be noted that the DC voltage after the active PFC circuit will contain a ripple at twice the line frequency, because the power through D_1 varies with this frequency.

Therefore, it is not possible to regulate the voltage v_{DC} precisely, because otherwise the current tracking is not possible. Furthermore, an EV battery's voltage may vary considerably depending on its state of charge (SOC). For this and other reasons, a DC-DC converter is usually needed after the PFC circuit. This is in [1] implemented using an isolated full-bridge converter. The workings of DC-DC converters will not be discussed further.

The boost active PFC stage only operates with positive voltages. In case a converter operates with negative voltages in its input stage, it would not require the four rectifying diodes to generate a pulsating DC voltage. This is the case with a full bridge converter as described previously. However, to comply with THD requirements for grid connection, an inductor is required in the full bridge converter's input to reduce current switching harmonics. Notice the similarity with the boost converter in fig. 2.6: The diode D_1 is replaced with a switch, and this three-element boost circuit is duplicated to make up the two legs in a full-bridge converter. This allows the generation of negative voltages, thus avoiding diodes in the input stage. This circuit supports unity power factor operation, and it also supports bidirectional power flow.

Expanding this into a three-phase solution yields the same topology as the three-leg motor drive, with inductors added for each phase, as shown in fig. 2.7[4]. The purpose of the inductors is elaborated in section 2.3.1. Due to the similarity of the motor drive and the battery charger, it is possible to utilize the same components for both purposes, because EVs are not driven and charged simultaneously. One approach to reusing the components is seen in fig. 2.8, where the additional components to the motor drive are a contactor (K1-K3) and the inductors (L1-L3). The working principle is that during driving, the contactor is configured so the motor is supplied

---

[4]The full-bridge single-phase topology could also be triplicated for a three-phase solution, but this requires the double amount of switches and require galvanic isolation if the same DC bus is shared.
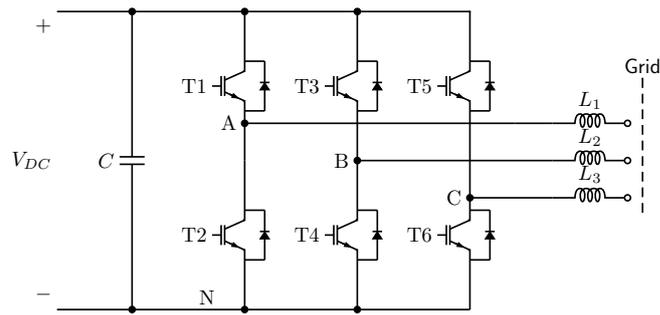
Figure 2.7: Grid interfacing three-phase bridge
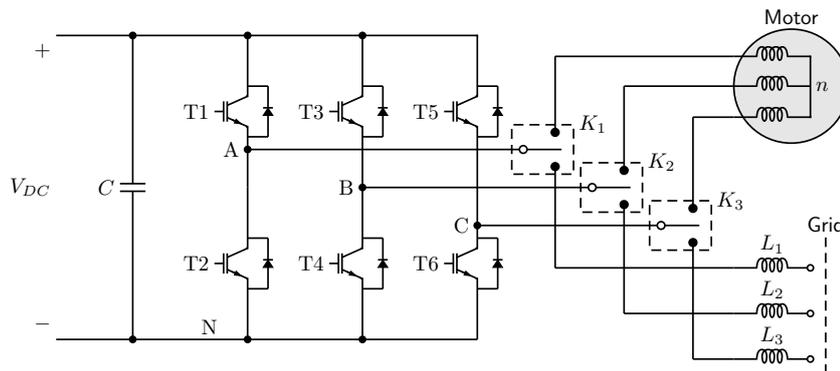
Figure 2.8: Integrated motor drive and battery charger using discrete inductors

by switches T1-T6, and when the vehicle is charged, the same switches T1-T6 interfaces the grid through the inductors. This is the first of two steps in integrating the battery charger with the motor drive.

The second step is to utilize the leakage reactance in the motor windings as the inductance required in the grid interface, as shown in fig. 2.9. This requires splicing the motor's star point and employing a contactor to switch between traction mode (closed) and charging mode (open). Successfully accomplishing this step reduces the component count further, because no additional discrete inductors are needed. These two steps are the basic idea behind the *integrated motor drive*.

However, there is one major concern with this approach: The three-phase currents running through the motor windings in charging mode effectively exerts a torque on
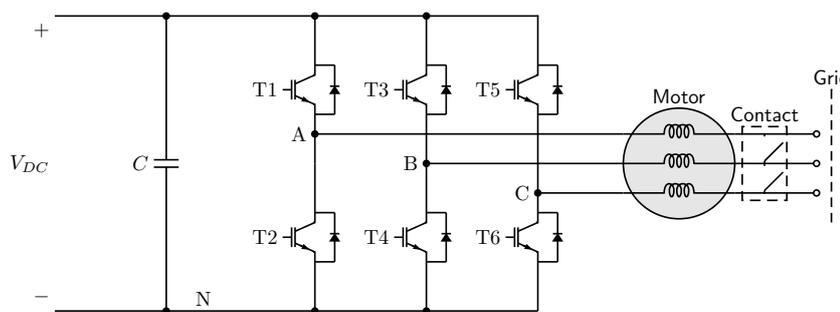
Figure 2.9: Integrated motor drive and battery charger using motor leakage inductance
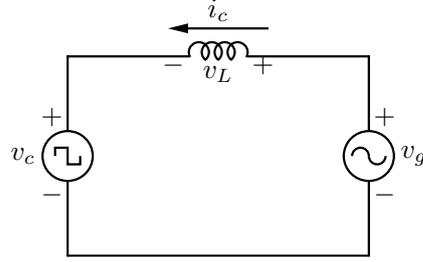
Figure 2.10: Simplified single-line converter circuit

the rotor, exactly as if the motor was used for traction. This is obviously undesired because the EV must not move during charging. Therefore, using discrete inductors as shown in fig. 2.7 may be a viable choice after all. Both solutions, and more, are explored in section 2.4.

When the concept of *integrated motor drives* is employed, this approach clearly lowers the cost of the charger, because only few additional components are required. Furthermore, the components will be rated for the high power that is required to drive the motor, and thus high power charging is implicitly made possible. Furthermore, the bidirectional capability of the motor drive enables reverse power flow for vehicle to grid purposes.

2.3.1 Power transfer through an inductor

As shown in the previous section, an inductance is placed between the three-leg converter switches and the grid. This is shown in a simplified single-line lossless fashion in fig. 2.10. Here, v_c is the modulated voltage from the converter, v_g is the sinusoidal grid voltage and v_L is the voltage across the inductor. The converter current i_c is positive in rectifier mode. We denote the phasors as $\boldsymbol{V_c}, \boldsymbol{V_L}, \boldsymbol{V_g}$ and choose $\boldsymbol{V_g}$ as the reference phasor. Thus, the current through the inductor is:

$$\boldsymbol{V_L} = \boldsymbol{V_g} - \boldsymbol{V_c} \tag{2.16}$$

$$j\omega L \boldsymbol{I_c} = V_g - V_c \cdot e^{j\delta} \tag{2.17}$$

$$\boldsymbol{I_c} = \frac{V_g - V_c \cdot e^{j\delta}}{j\omega L} \tag{2.18}$$

Here δ is the phase shift between the grid voltage and the converter voltage, known as the load angle. The power transfer from the grid to the converter is given by grid voltage multiplied with the converter current conjugated:

$$\begin{aligned} \boldsymbol{S_C} &= V_g \cdot \boldsymbol{I_c^*} \\ &= V_g \cdot \frac{V_g - V_c \cdot e^{-j\delta}}{-j\omega L} \\ &= \frac{jV_g}{\omega L} \cdot \left(V_g - V_c \cdot e^{-j\delta} \right) \end{aligned} \tag{2.19}$$

Extracting the real and imaginary part yields the active power P_c and reactive power Q_c:

$$\boldsymbol{S_C} = \frac{jV_g}{\omega L} \cdot (V_g - V_c\,(\cos\delta - j\sin\delta)) \tag{2.20}$$

$$P_c = \mathrm{Re}(\boldsymbol{S_C}) = -\frac{V_g V_c}{\omega L}\sin\delta \tag{2.21}$$

$$Q_c = \mathrm{Im}(\boldsymbol{S_C}) = \frac{V_g}{\omega L}(V_g - V_c\cos\delta) \tag{2.22}$$

The usual relations for active and reactive power are still valid:

$$P_c = V_g I_c \cos(\theta) \tag{2.23}$$

$$Q_c = V_g I_c \sin(\theta) \tag{2.24}$$

Here, θ is the power factor angle and expresses the phase shift of the voltage and current fundamentals. Above relations can be visualized in a phasor diagram, as shown in fig. 2.11. It is evident that the grid voltage is the reference phasor and drawn vertically with a magnitude corresponding to its rms value V_g. The voltage generated by the converter is drawn with magnitude V_c and the load angle δ from the grid voltage. The voltage difference between the two is the voltage across the inductor, $\boldsymbol{V_L}$, and the current through the inductor I_c is seen to be exactly 90° shifted with a magnitude given by $\frac{V_L}{\omega L}$. The power factor angle θ is, according to its definition, drawn as the angle between the grid current and voltage. This is also the angle of the phasor $\boldsymbol{V_L}$ from horizontal. If $\boldsymbol{V_L}$ is located along the horizontal axis, θ will be zero and eqs. (2.23) and (2.24) yield only active power. In eq. (2.22), the term $V_c\cos\delta$ yields V_g, also resulting in zero reactive power.

Correspondingly, if $\boldsymbol{V_L}$ is located along the vertical axis (in phase with $\boldsymbol{V_g}$) then theta is 90° and only reactive power will be exchanged with the grid. In this case, δ will be zero and eq. (2.21) also yields zero. This is clarified in the drawing by indicating that a displacement in $\boldsymbol{V_c}$ along the horizontal axis from the grid voltage is related to active power, and a displacement along the vertical axis from the grid voltage is related to reactive power. It is then easily imagined which situations entail minimum and maximum active and reactive power.

It is clear that by varying the amplitude of the converter voltage V_c and controlling the load angle δ, it is possible to generate any combination of active and reactive power, up to the limits indicated by the dashed circles. This is therefore implemented in the controller of the converter, to be explained in section 2.6. A few situations are especially useful, which are indicated in fig. 2.12, where the annotation is left out for simplicity because it is similar to fig. 2.11. It is seen that $\theta = 0°$ yields maximum active power flowing from the grid to the converter, and no reactive power. $\theta = 90°$ yields no active power but maximum reactive power emitted by the converter. $\theta = 180°$ yields maximum reverse active power flow, that is, power flowing from the converter to the grid. Finally, $\theta = -90°$ yields no active power but maximum reactive power consumed by the converter.
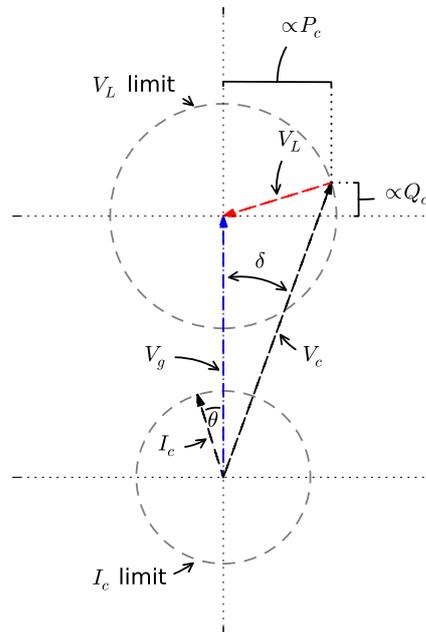
Figure 2.11: Phasor diagram with grid, inductor and converter voltage phasor
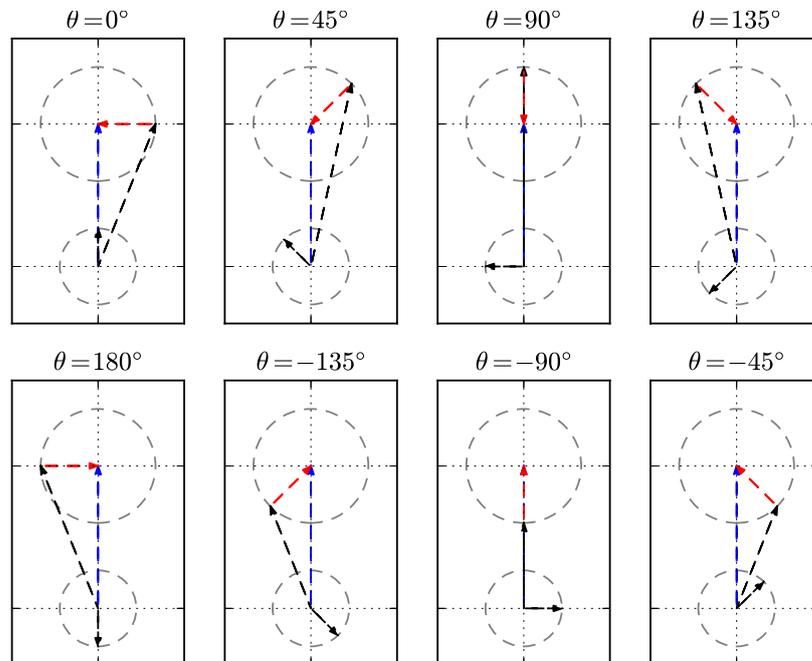
Figure 2.12: Multiple phasors with varying power factor angle

It should also be noticed from the phasor diagrams that unity power factor entails $\theta = 0°$ or $\theta = 180°$, and in these cases, the converter voltage must always be higher than the grid voltage. If it is lower than the grid voltage, the current will be phase shifted and reactive power will be consumed by the converter. Therefore, as was earlier pointed out, this shows that the DC bus voltage must always be higher than the peak AC voltage for unity power factor operation.

The presented illustrations show how a modulation of the voltage across an inductance is indeed useful, and allows arbitrary four-quadrant power flow depending on the converter voltage phasor. This is the core technology required for EVs to provide ancillary services to the grid and provide active and reactive power as demanded.

2.4 Implementation of the integrated motor drive

A number of different topologies for integrated motor drives (IMD) exist [39]. Some will be briefly described in 2.4.2. Common for most IMDs is that they utilize the leakage reactance in the motor's stator windings to realize the inductor required in the boost converter topology. Since all motors are built with an air gap to allow the rotor to revolve, the leakage reactance can be substantial. Furthermore, the current rating of the motor is often higher than required for charging applications. These facts make it obvious to exploit the motor for charging purposes while requiring only little or no additional inductance. Furthermore, the IMD topologies utilizing the motor leakage reactance all require means of avoiding or mitigating torque exertion in either induction machines (IM) or synchronous machines (SM) with or without permanent magnets (SMPM).

2.4.1 Using motor leakage reactance

Fundamentally, leakage reactance stems from magnetic flux linking only the coil that creates it. Inductors are made from a single coil, meaning the magnetic flux can only link that coil. Transformers and motors are made of multiple coils, and both types of machines work by linking magnetic flux between multiple coils. The goal is usually to have a perfect coupling of magnetic flux between the coils, but this is impossible due to the finite magnetic permeability of air surrounding the windings in transformers and electric motors. Thus, some of the flux will only link the coil that creates it, which makes this coil look like a pure inductor in series with a purely coupled set of windings.

For example, the equivalent circuit of an induction motor is shown in fig. 2.13 where the leakage components are denoted X_1 and X_2. The former is the leakage reactance created by flux leakage in the stator windings, and the latter is the leakage reactance created by the rotor windings. The resistances R_1, R_c, R_2 are, respectively, the stator winding resistance, the equivalent core loss resistance and the rotor winding resistance (which depends on slip s). X_m is the magnetizing reactance which signifies the air gap flux actually linking the stator and rotor windings. The leakage components X_1, X_2 are made as small as possible because they introduce voltage drops that inhibit motor performance. However, they are not possible to remove completely, and the remaining leakage reactance can be exploited for use
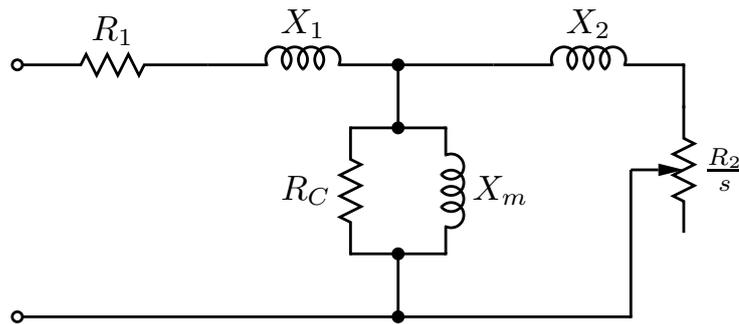
Figure 2.13: Induction motor equivalent circuit diagram
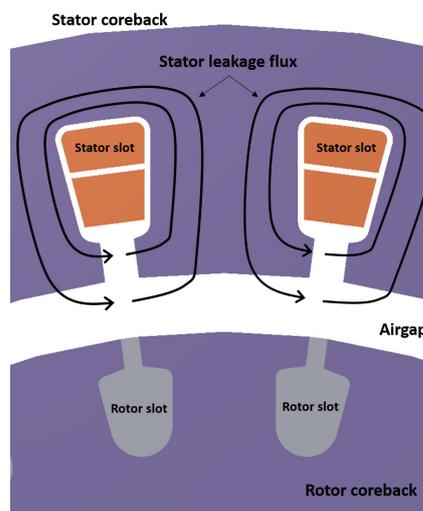
Figure 2.14: Stator coreback. Leakage flux arrows drawn for one coil

in IMDs.

In fig. 2.14 two slots of an IM stator coreback are sketched. A few black lines are (inaccurately) added to the drawing which show the magnetic flux lines that only link the coil that creates it, in this case the stator coils. Note these lines do not reach the rotor windings, meaning they add to the leakage reactance of the stator coil.

The leakage reactance is difficult to calculate analytically [35], and estimation requires either finite element models or practical experimenting. Generally, the leakage reactance will depend on the the size of the motor, the materials used, coreback dimensions and winding layout. Assuming the leakage reactance is a fixed percentage of the useful air-gap flux, the leakage reactance can be expected to be proportional with motor radius r, length l and number of turns squared, N^2, that is, $X_{leak} \propto l \cdot r \cdot N^2$.

2.4.2 Some IMD topologies

Six examples of IMDs are described below. Many other IMD configurations are possible, but they will usually be variants of these examples.

Discrete inductor. This approach was previously sketched in fig. 2.9, and it does not utilize the motor leakage reactance but rather a separate inductor. This is a relatively simple approach, and since the charging current is not flowing through the motor, it does not pose any requirements on motor type, stator winding layout or vehicle restraining. The disadvantage is that it adds cost and weight to the powertrain. This approach has seemingly not been touched upon in academic papers in relation with EV onboard integrated fast-chargers, perhaps because it is judged not to contain novel value. However, it is crucial to compare other approaches with this to make sure other approaches are feasible. Therefore, a reference design using this approach is described in detail in section 2.4.3.

IM with blocked rotor. This approach is relatively simple, because it only requires deleting the motor star splice and using a contactor for reconfiguration between traction and charging modes, as already shown in fig. 2.9. However, the major disadvantage is that due to a three-phase current running through the stator windings, a torque is exerted on the rotor. Therefore, the car must be restrained with a parking brake or pawl during charging. Due to its simplicity, it is explored in detail in section 2.4.4. This approach cannot be used with SMs due to torque ripple and vibration introduced when operating an SM asynchronously [39].

IM or SM with mechanical clutch. The idea of this approach is to allow the motor to rotate while it is physically disconnected from the wheels using a clutch. This approach was used in [39] with SMs, and is therefore not described further here. This approach is only moderately suitable for IMs because SMs will usually be more efficient. In any case, it entails friction losses during charging, which lowers efficiency.

IM or SM with wound rotor. It is possible with this approach to avoid magnetic field generation in the rotor because the rotor is wound and can be disconnected. Thus, no torque is exerted when no field is generated in the rotor. One disadvantage is that this is an uncommon motor design for EVs, and has thus not been possible to test in this project. Furthermore, a wound rotor means slip rings are required to electrically connect the stator and the rotor, which may lower motor durability. An uncommon design may also increase initial costs. However, this is indeed a valid approach that should be investigated further to assess its feasibility.

One approach may be especially interesting, which seemingly has not been investigated before: Slip rings can be avoided in an IM design if the rotor windings can be connected and disconnected magnetically, that is, wirelessly. Wound rotor IMs exist, but they are usually used to vary the rotor resistance for altering the torque curve for motor starting, or in the case with doubly fed induction generators, for variable speed applications in e.g. wind turbines. Therefore, the existing wound rotor IMs must have slip rings for power transfer between rotor and stator. However, in the case of IMDs in EVs, we are only interested in having either full torque during traction (short circuited rotor winding) or no torque during charging (open ended rotor winding), and therefore only a connect-disconnect mechanism is required. This may be possible to implement without slip rings through a special electromechanical arrangement. This is a promising approach, but has not been explored further in this project.

IM or SM with split phases. With this approach, the motor stator winding
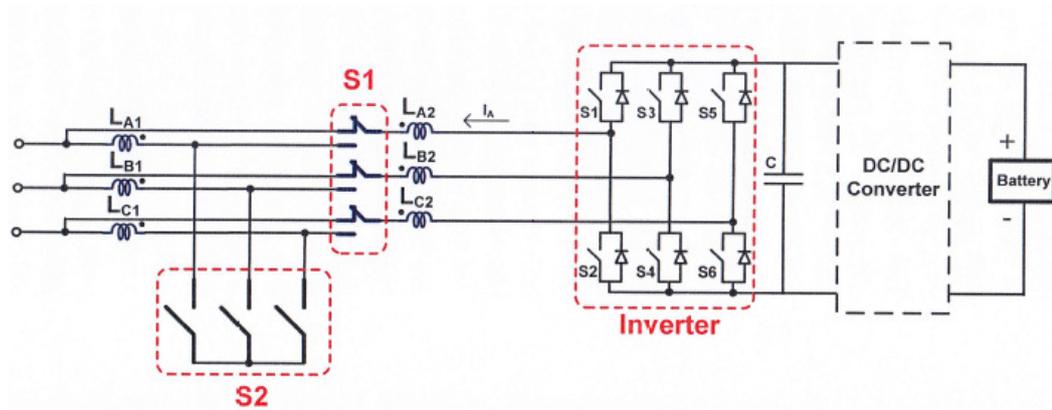
Figure 2.15: Split-phase topology, from [39]
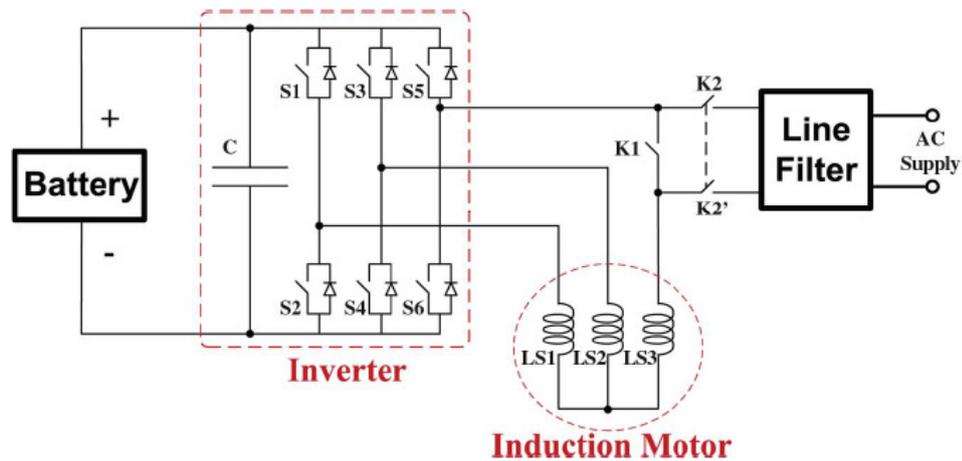
Figure 2.16: AC Propulsion single-phase topology, from [39]

is split into two similar halves, and the current flows in opposite directions in the two phase halves. This results in zero net torque, but the leakage reactance is still present and can be used for charging purposes. An example of such topology is shown in fig. 2.15. Here, two contactors are used to reconfigure the motor windings. For traction, S2 is closed, S1 is connected as shown, and the windings are thus star connected. For charging, S2 is open, S1 is switched, and the windings are connected in series with opposite winding directions. Therefore, this approach requires two contactors, and it requires deletion of the motor star splice so it can be accessed and reconfigured between traction and charging. This approach has been touched upon in [39], but it requires more research to assess its feasibility. One issue is that harmonics generate a non-zero torque which entails audible noise and requirements for vehicle restraining.

IMs and single phase charging. Running a single-phase current through a coil in a three-phase machine will generate an equal amount of torque in both directions, meaning that the net torque is zero when the rotor is at standstill. This is a major

advantage inherent to this approach, but since it only uses one phase the power transfer will vary sinusoidally, and less power can be transferred compared to a three-phase connection. The many single-phase outlets in the US advocates the use of this IMD type there. The American company AC Propulsion uses this approach in the AC Propulsion eBox and in the BMW Mini-E, as depicted in fig. 2.16.

The two most simple solutions are explored further: Using a discrete inductor and using a blocked rotor IM.

2.4.3 Construction of discrete inductor

This section describes the design of an inductor, and afterwards constructs a prototype of this design. This is important because any attempt of realizing the converter inductance by using motor leakage reactance must be compared to this relatively simple approach.

An inductor can be designed in many ways using various materials and shapes. Generally, an inductor consists of a copper wire wound on a magnetically permeable, ferrous material. The permeability of an inductor core is normally limited to avoid core saturation at rated current. For highly permeable materials, an air gap is introduced to limit the effective permeability of the core. When designing an inductor for any application, there are a few constraints that must be fulfilled:

1. The required inductance must be obtained. This is given by

$$L = \frac{N^2 \mu A_c}{l_c} \tag{2.25}$$

   Here, L is the inductance in Henry, N is the number of turns, μ is the effective magnetic permeability of the core, A_c is the cross section of the core, and l_c is the effective path length of the core. The number of turns may be obtained from equation (2.25) when the required inductance and the core constants are known.

2. The core must not saturate. The maximum core flux density is given by

$$B_{max} = \mu H_{\max} = \frac{\mu N I_{max}}{l_c} \tag{2.26}$$

   Here, B_{max} is the maximum flux density, H_{max} is the maximum field strength, and I_{max} is the maximum current in the windings. The relationship between B and H is often obtained much more accurately through a B-H graph of a given material, since it is non-linear and thus does not have a constant μ over its operating range. An example of the B-H characteristic of an inductor core is seen in fig. 2.17.

3. There must be enough space for the wiring. If we denote the total area of the copper in the window as A_{cu} and the window area as A_w then it must be valid that

$$A_{cu} \leq \frac{K_u \cdot A_w}{N} \tag{2.27}$$

Core dimensions	
Core outer diameter	77.8mm
Core height	17.1mm
Window area	1820mm^2
Core cross section	442mm^2
Magnetic path length	196mm
Mean length per turn, $K_u = 0.5$	131mm
Weight	640g

Table 2.3: Physical dimensions of inductor core

where K_u is the winding factor, which is typically in the range of 0.3 to 0.5. If it is lower, then a part of the window area is unused and a smaller core can be picked, and if it is higher then the wires will likely not fit (note that round wires do not pack perfectly and wire insulation should also fit in the core window). Also, if the copper wires are made too small, then the heat dissipation from the I^2R loss will be the limiting factor.

One possible design parameter to calculate appropriate wire sizes is to define a current density J, usually on the order of 2-8 A/mm^2 for copper using natural convection cooling. The wire area is then given by

$$A_{cu} = \frac{I_{rms}}{J} \tag{2.28}$$

Assuming a sinusoidally shaped current we have $I_{rms} = I_{max}/\sqrt{2}$.

2.4.3.1 Example design

Based on the constraints given in the previous section, an example inductor design will be shown. It is clear that a good design may require a few iterations, and the design presented here has been found after a few retries that are not described. Also, only toroidal designs were investigated, but other core shapes may be used as well.

The inductor will be designed for a grid-connected (50Hz) converter with a current rating of 63A RMS $\approx$ 90A peak. The inductance should be 1mH. The current density is assumed to be 6A/mm^2.

The core used in the design features a distributed air gap and is made from ferrite-silicon (6.5%) powder. The core is manufactured by the company Magnetics Inc, and its part number is 78907. It is a part of the the X-Flux core material series used for high flux density, low frequency applications requiring low cost. The core has a rated permeability of $60\mu_0$ at low currents (see fig. 2.17). Two cores are stacked together, and their combined dimensions can be seen in Table 2.3.

First, the approximate number of turns is found from eq. (2.25):

$$N = \sqrt{\frac{Ll_c}{\mu A_c}} = \sqrt{\frac{1\text{mH} \cdot 196\text{mm}}{60\mu_0 \cdot 442\text{mm}^2}} \approx 77 \text{ Turns} \tag{2.29}$$
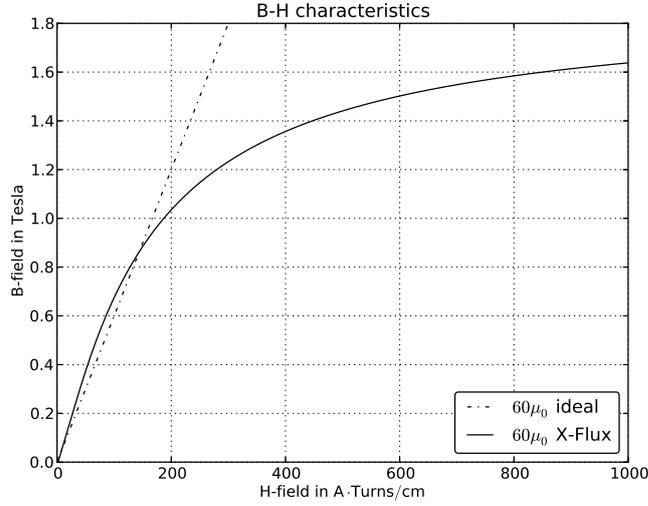
Figure 2.17: B-H curve for the chosen inductor core

The resulting magnetic field strength can be found by

$$H_{max} = \frac{NI_{max}}{l_c} = \frac{70 \text{ Turns} \cdot 90\text{A}}{196\text{mm}} = 3.52\text{A} \cdot \text{Turns/m} \qquad (2.30)$$

From the B-H curve in fig. 2.17 this corresponds to a flux density of 1.3T, which is high but still reasonable compared to its saturation limit of around 1.4T-1.6T.

The wire cross section is:

$$A_{cu} = \frac{I_{max}}{\sqrt{2}J} = \frac{90\text{A}}{\sqrt{2} \cdot 6\text{A/mm}^2} = 10.6\text{mm}^2 \qquad (2.31)$$

Thus, the fill factor is:

$$K_u = \frac{NA_{cu}}{A_w} = \frac{70 \cdot 10.6\text{mm}^2}{1820\text{mm}^2} = 0.44 \qquad (2.32)$$

For a fill factor of 50% (that is, a bit more than just calculated), the mean length per turn is 131mm according to Table 2.3. Assuming a copper resistivity of ρ=16.8nΩm, the total copper resistance is:

$$R_{cu} = \rho\frac{l_{cu}}{A_{cu}} = 16.8\text{n}\Omega\text{m}\frac{131\text{mm} \cdot 77 \text{ Turns}}{10.6\text{mm}^2} = 16\text{m}\Omega \qquad (2.33)$$

The copper losses are then

$$P_{cu} = I_{rms}^2 R = (63\text{A})^2 \cdot 16\text{m}\Omega = 63W \qquad (2.34)$$

Assuming a copper density of 8900 kg/m^3, the copper mass is:

$$M_{cu} = 8900\text{kg/m}^3 \cdot 131\text{mm} \cdot 77 \text{ Turns} \cdot 10.6\text{mm}^2 = 940\text{g} \qquad (2.35)$$

Thus, the inductor weighs around

$$M_L = 940\text{g} + 640\text{g} = 1580\text{g} \qquad (2.36)$$

(a) Inductor cores before winding

(b) Four copper wires wound in parallel

(c) Finished inductor
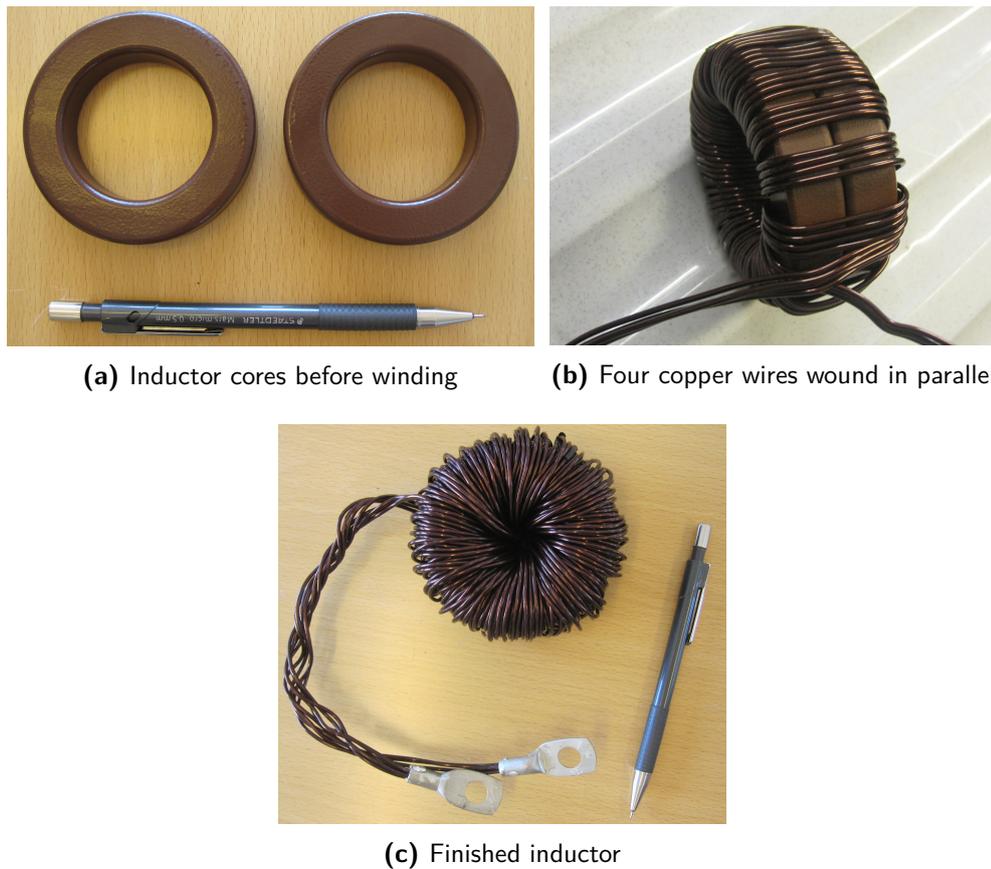
Figure 2.18: Inductor prototype

2.4.3.2 Inductor prototype and test

The aforementioned core was procured and it was wound according to the calculations made in the previous section. The two cores stacked in the design are shown in fig. 2.18 along with the finished inductor. The copper wire used was 1.8mm in diameter, yielding 2.54mm^2 per wire. Four wires were put in parallel achieving a total copper cross sectional area of $4 \cdot 2.54\text{mm}^2 = 10.2\text{mm}^2$, meaning the actual current density is $\frac{63\text{A}}{10.2\text{mm}^2} = 6.2\text{A/mm}^2$. The total length of the copper wire was expected to be $131\text{mm} \cdot 77\text{turns} = 10.1\text{m}$ of copper wire. However, it was in this hand-wound prototype design only possible to put 9.5m of wire on the inductor, and it is therefore expected to achieve a somewhat lower inductance than found in previous section. Furthermore, the weight came in at 1500g, a bit lower than the calculated 1580g.

For testing, a three-phase 150kW power amplifier available in the lab was used, capable of supplying up to 63A from a normal CEE outlet with a fine control of supply voltage. The inductor was connected between a phase and neutral, and a 50Hz voltage was applied in steps of 0.1V. The inductance is then for each measurement calculated by
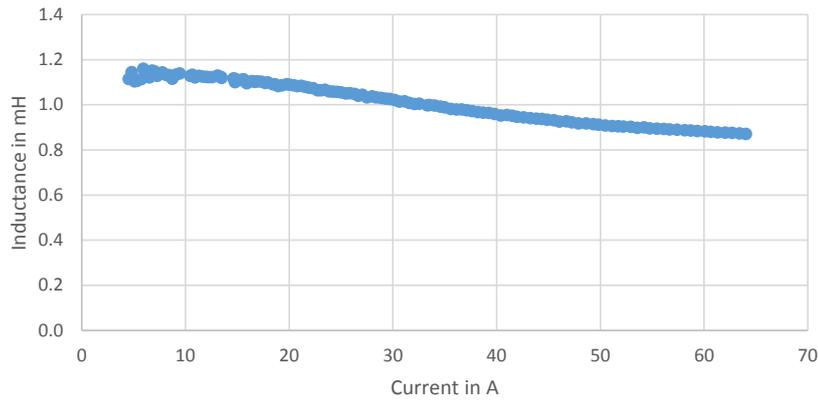
Figure 2.19: Discrete inductor inductance versus current

Inductor parameters	
Current rating	63 A
Inductor outer diameter	90mm
Inductor height	55mm
Turns	70
Wiring	3x3.14mm^2
Weight	1.5kg
Price	22.88 USD / 100 pcs

Table 2.4: Chinese manufacturer's inductor parameters

$$L = \frac{Q_{1p}}{2\pi \cdot 50\text{Hz} \cdot I_{line}^2} \tag{2.37}$$

Here, Q_{1p} is reactive power per-phase measured by the power amplifier. The measurements and calculations can be seen in appendix A, and the current versus inductance is plotted in fig. 2.19. It is seen the inductance is 1.1mH at low currents and decreases to 0.85mH at currents around 63A. The drop in inductance is expected due to the decreasing slope of the relative permeability μ as seen in fig. 2.17. However, it is seen the inductance in any case is quite close to the design goal of 1mH. The series resistance was found to be 16mΩ (see fig. A.3), which is similar to the theoretical value.

2.4.3.3 Production and cost

To get a realistic estimate of the production cost of the inductor on a larger scale, a quote was procured from a Chinese manufacturer. Their inductor's parameters are found in Table 2.4.

It is evident that this design matches well with the theoretical design shown in the previous section. The manufacturer suggests a price of around 23 USD per coil in a relatively small volume (100 pcs). In a three-phase converter, at least three of

these coils are needed, resulting in a price of 69 USD and a total weight of less than 5kg.

It should be repeated that this design and price estimate is for a 1mH inductor rated for 63A RMS. In case the current rating is less (say 32A RMS), the weight and price might be less than half the price and weight because other and cheaper core materials will be available and the cooling requirements may be less due to lower I^2R losses. However, this can vary a great deal depending on how the design turns out exactly.

2.4.4 Tests on Think City EV motor

In order to assert the feasibility of using the leakage reactance in an IM with blocked rotor during charging, practical experiments were carried out. An induction motor from a Think City EV was procured for this purpose. The vehicle was broken and could not drive, likely due to a battery issue, but this was secondary to this project because only the motor is of interest. The experiments performed and their results are described in this section.

A picture of the EV, the test setup and the motor is shown in fig. 2.20. It was decided to do testing with the motor mounted in the vehicle, because it would have been difficult to design a separate test stand for the motor. For instance, the rotor in the motor is fixed in position by the gearbox, meaning it is nearly impossible to make an experimental setup without the gearbox. However, the gearbox has the differential built-in and the wheel axle splines are attached directly to the differential. This again makes it difficult to mount in a separate test stand because both differential axles have to be used. For this and other reasons, the car itself was used to hold the motor in place and the traction wheels were lifted from the ground allowing the wheels and motor to spin freely.

The three-phase AC connection for the motor was disconnected from the onboard motor drive, and was instead connected to the 150kW three-phase power amplifier available in the lab. The power was supplied from a 63A outlet connected to the power amplifier. As seen in fig. 2.20e, the motor's rated frequency is 120Hz, at which frequency it supplies up to 17kW at a wye voltage of 127V and a line current of 130A. However, the motor was only tested up to currents of around 63A because of the outlet's current limitation. Hence, the motor was not tested to its limits and there was no risk of damaging it.

The power amplifier has many features. To keep these tests as simple as possible, it was only necessary to change voltage and frequency, and read out the corresponding measurements of actual voltage, frequency, current, active and reactive power. These measurements were performed by the power amplifier itself. To speed up the testing procedure, a Python script was written to easily change voltage and frequency, and automate the readout of measurements, as shown in appendix C.

A total of five tests were conducted. Initially, the stator resistance was found by measuring the DC voltage-current characteristic. The next two tests, the no load test and the blocked rotor test, were used to estimate the IM equivalent circuit parameters and the dynamic torque characteristic. The third test was a measurement of the starting torque at a supply frequency of 50Hz, resembling the case where the

(a) Setup with Think City EV. Torque measurement lever is mounted on right front wheel.

(b) A look to the motor. Note the three-phase cable hangs out.

(c) Torque lever mounted on reversed disc brake. It presses on digital scale 20cm from wheel center.

(d) Three-phase 150kW power amplifier connected to the motor. The cable to the motor is quite long and must be taken into account.

(e) Motor ratings as shown on sticker. 127V wye, 120Hz, 130A, totaling 17kW.

(f) A look inside the motor. The rotor must be held in place by the gearbox, and it is thus easiest to have it mounted in the EV.

Figure 2.20: Think City EV motor test

rotor is blocked but grid frequency current is flowing through it. The last test was a measurement of the maximum starting torque (at low frequency) to be compared with the torque measured in the 50Hz torque test. A detailed description of the tests is found in appendix B. The accuracy of the tests is not overly important, because the goal is to emphasize the concepts and issues related to IMDs.

2.4.4.1 Motor test discussion

The experiments performed lead to the following conclusions:

- Through relatively simple tests it is possible to calculate the torque characteristic of an IM.

- The starting torque of an IM is low when it is supplied with grid frequency voltage. With the motor used in this test, the torque was below 5Nm. This makes it possible to restrain the vehicle during charging. Full torque is only provided when the motor is supplied at much lower frequencies.

- The leakage inductance of the Think City EV motor was found to be approximately 170μH per phase.

It should be noted that the leakage inductance in this motor is only 170μH. This is likely too small to be used in a converter application. However, the motor leakage inductance could be made much higher. For instance, if the motor had doubled its voltage rating, the number of turns would equally have doubled to create the same flux density in the core material. Hence, assuming the leakage inductance is proportional to air-gap inductance and the number of turns squared, the leakage inductance would become four times larger. Also, the Think City motor is only rated for 17kW, where modern EV motors typically provide more power - 80-200kW is commonly seen. This means the motor will be larger and the leakage inductance will increase as well.

However, this means the motor must be designed with the charging application in mind. This is a disadvantage in that it requires the use of motors designed specifically for this purpose, and it is difficult to change the motor without a considerable amount of redesign.

The discrete inductor designed in the previous section had a measured inductance of around 1mH. This shows it is relatively easy to achieve inductances similar to that of the leakage inductance in motors.

The parking pawl required for vehicle restraining will likely add some weight to the vehicle, although this has not been considered in detail in this report. However, the point is that this is not needed if discrete inductors are used. Hence, the additional weight of the inductors ($\approx$5kg) may be an acceptable trade-off.

Based on above tests and considerations, it is deemed somewhat difficult to use the motor leakage inductance for charging applications. It is definitely possible, but it requires additional considerations during the design of the power train. It should be considered if using discrete inductors is a simpler and easier approach, or if one of the other approaches described in section 2.4.2 should be utilized.

2.5 Converter topology challenges

This section briefly discusses challenges in relation to the presented three-phase converter topology, namely galvanic isolation, DC injection and leakage, DC bus voltage restrictions, efficiency and THD. The solution to these challenges depend on the exact converter design and are therefore difficult to present in general in this section.

2.5.1 Galvanic isolation

The term galvanic isolation is used whenever electric reference potentials across an isolation barrier can be set arbitrarily. In the case of EVs, the isolation would be located between the grid and the battery DC bus during charging. Isolation is achieved through e.g. the use of a transformer which only links AC voltages between the transformer coils, but the DC voltage level can be chosen arbitrarily (limited by insulation capabilities). A few general considerations on isolation and safety are presented in this section, but a more comprehensive analysis of all possible fault conditions is required to assess the required safety means.

Commonly, galvanic isolation is employed as part of a safety strategy. It is often referred to the fact that in an isolated system, a person can touch one DC voltage rail and not experience an electric shock other than an ESD discharge arising from parasitic capacitances. In a non-isolated system, touching one voltage rail gives an electric shock, but it is possible to detect this because a current flows to earth and not through the usual path in the return conductor. In both isolated and non-isolated systems, a person touching both voltage rails simultaneously will experience a hazardous shock. Hence, it can be stated that a galvanically isolated system is "one-fault safe" whereas a non-isolated system is "one-fault protectable" [52], implying a non-isolated system is safe if the fault is detected and the circuit is switched off.

The transformer employed in an isolated system adds to weight and price while lowering efficiency due to iron and copper losses. The transformer may be either a low-frequency transformer located on the grid side, or it can be employed as part of a high-frequency DC-DC converter on the DC bus side, which reduces the weight of the transformer considerably. In any case, non-isolated converters are typically more efficient.

Galvanic isolation is not a modern requirement in standards related to EVs, including IEC 61851. Within the solar inverter industry, several vendors avoid the use of transformers to increase efficiency (also known as transformer-less, or TL, inverters) [13].

In non-isolated EV converters, the traction battery must be electrically isolated from vehicle chassis (due to the voltage v_{Nn} in eq. (2.5)). This is not a strict requirement for an isolated converter, but the traction battery is typically isolated anyway to allow the one-fault-safe capability, that is, one voltage rail can be touched by a person or short circuited to chassis without any adverse effects. For both non-isolated and isolated converters, a short circuit to vehicle chassis can be detected by measuring the voltage v_{mid} across a resistive voltage divider with its midpoint
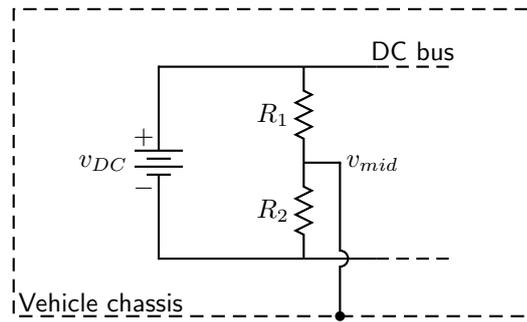
Figure 2.21: Simple battery isolation fault detection

connected to vehicle chassis, as shown in fig. 2.21. If one rail is short circuited to chassis, current is shunted away from one of the resistors in the voltage divider and the fault can be detected [58].

Faults in isolated systems may effectively lead to a non-isolated system. For example, insulation breakdown caused by an accident or other mechanical failure may short circuit the two isolated sides. This means residual current detection employed in non-isolated systems must also be used in isolated systems, and there are hence no implicit savings on fault-detection equipment in isolated systems.

Conclusively, it is not required to have the traction battery electrically isolated from the grid. With both isolated and non-isolated systems, vehicle chassis short circuit detection, residual current detection (RCD) and over-current fuses are necessary to protect against faults.

2.5.2 DC injection and leakage

The current flowing between the battery and the grid is completely controllable by the three-phase bridge (see section 2.6). In the most extreme case, imagine a fault where a converter switch malfunctions, and the battery voltage is applied directly to two or three grid phases. This introduces a DC current injected into the grid. In this specific case, a breaker or fuse onboard the vehicle or in the charging station will likely switch the converter off due to excessive currents.

However, a smaller DC current may be injected into the grid during normal operation due to small inaccuracies in the control circuit[43]. For example, in practice, the current used in the control circuit is usually measured using hall effect sensors which may introduce a DC drift depending on temperature [21]. This inhibits complete elimination of DC offsets, and small DC injection currents flow to the grid.

DC injection currents may drive local distribution transformers into saturation which could result in additional losses. For energy metering applications, DC currents through wires monitored by current transformers result in erroneous current measurements and thus incorrect energy measurements [15].

The standard IEEE 1547 sets the DC current injection limit to 0.5% of the rated current of the equipment. A paper suggests this limit is reasonable based on the difficulty in measuring small DC currents [43]. Furthermore, DC injection from

multiple grid-connected converters are found to have a normal distribution with a mean of zero, suggesting there may not be any adverse effect when several EVs are charged at one location simultaneously.

One project tests RCDs by applying a DC injection current [15], and it was evident that the tested RCDs trip as expected during a ground fault.

The DC injection issue is not solved only by employing galvanic isolation in an onboard DC/DC converter. Although the battery is isolated from the grid with this topology, it is still possible to inject DC currents due to inaccurate control in DC/AC bridges.

Measurement techniques to reduce DC injection currents have been proposed [20]. Furthermore, means for removing DC currents without precise DC current measurement sensors have been suggested [21]. The idea is to series connect a large capacitor in front of the converter. Since a capacitor also provides galvanic isolation, no DC currents can flow.

Theory suggests DC injection could introduce transformer saturation and faulty metering. However, in practice, DC injection does not pose a problem as long as converters are operated within defined limits.

It should be noted that DC injection currents are not *residual* currents, meaning they return to the source (e.g. EV battery) through the grid wires. Hence, RCDs[5] are not affected by DC injection currents.

However, RCDs are affected by residual DC currents flowing from the DC bus to earth, also known as DC leakage. This occurs if a non-isolated DC voltage rail erroneously conducts to earth, i.e. vehicle chassis. The DC leakage current is important to detect, because it is feared it may inhibit standard *type A* household RCDs from functioning properly due to saturation in the RCD coil. An earth fault on the DC rail can be detected by the circuit shown in fig. 2.21, or using a DC-sensing RCD as described in section 3.4. These RCDs are typically known as *type B*, and are more expensive than their type A counterparts. Appropriate countermeasures depend on the specific converter design, but it seems solvable in any case.

2.5.3 DC voltage requirement

In the full-bridge and three-leg converter topology, the DC bus voltage must be greater than peak line-line AC voltage to allow unity power factor operation. With the 400V three-phase grid common in EU, this entails a minimum DC bus voltage of:

$$v_{DC,EU} = 400\text{V} \cdot \sqrt{2} \approx 566\text{V} \tag{2.38}$$

In the US 480V three-phase grid, this entails

---

[5]Also known as GFCI, ground fault current interrupter

$$v_{DC,US} = 480\text{V} \cdot \sqrt{2} \approx 679\text{V} \tag{2.39}$$

Both are quite high voltages and are not supported by most EVs on the market today. Typically, battery voltages are less than 500V. This is also evident from the fact that CHAdeMO DC fast-chargers generate voltages up to 500V. There are at least three ways to accommodate this issue:

1. Increase battery voltage

2. Add DC-DC converter or introduce combined AC/DC converter

3. Add low-frequency step-down transformer

The advantages and disadvantages of these approaches are discussed below.

2.5.3.1 Increasing battery voltage

The cell voltage in a battery increases when it is charged. This means there is a minimum cell voltage when the battery is at 0% SOC and a maximum cell voltage when the battery is at 100% SOC. The minimum and maximum cell voltage depends on battery chemistry as well as temperature. As an example, assume we construct our battery with the cell type NCR-18650A from Panasonic [10]. The minimum cell voltage is 2.5V and the maximum voltage is around 4.2V. To reach the minimum DC bus voltage required (asumme this is 600V in Europe) at minimum cell voltage, we need a total of $\frac{600\text{V}}{2.5\text{V}} = 240$ cells in series. When the battery has been charged, the battery voltage will be $240 \cdot 4.2\text{V} = 1008\text{V}$, that is, around 1kV. This is more than twice as much as present EVs.

However, this voltage may be within reach: It likely requires redesigning the motor for higher voltages, and cable and connector insulation must be rated for this voltage. IGBTs are readily found with 1200V rating, and electrolytic capacitors can be put in series to withstand this voltage, or film capacitors can be used instead which are found with 1kV ratings or more. Another benefit is that increasing voltage means lower current, which means conductor cross sections can be made smaller and/or efficiency increases.

The EV battery vendor Brusa manufactures batteries with a minimum voltage of 540V and a maximum voltage of 747V, which is higher than most other EV batteries. Hence, high-voltage batteries are likely seen in the future, and when the battery voltage increases above e.g. 600V it is possible to supply power directly to the battery from the three-phase converter without additional circuitry. The voltage requirement increases to around 700V in US due to the higher three-phase AC voltage.

2.5.3.2 Additional DC-DC converter

An additional DC-DC converter is a common and good approach. It may use galvanic isolation or not. Without isolation, no transformer is needed which may
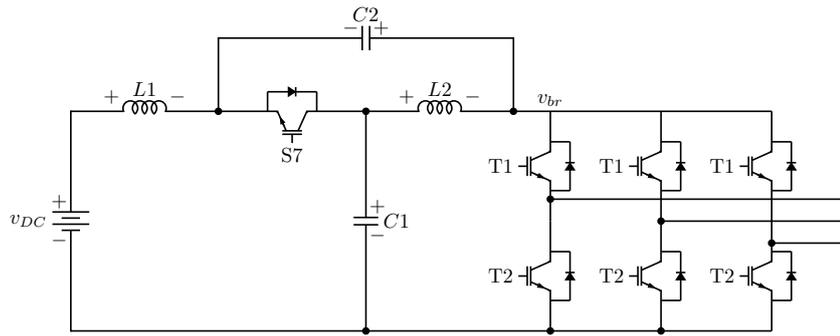
Figure 2.22: Bidirectional Quasi Z-Source converter topology

increase efficiency. On the other hand, the transformer can be used to step down voltage which is a benefit if the battery voltage is low (e.g. less than half the peak AC voltage). This efficiency and cost trade-off has to be assessed in a specific application.

The DC-DC converter also has the ability to ensure constant power is delivered to the battery. As will be evident in section 2.7.3, if the grid voltages are unbalanced then charging power will vary with twice the line frequency. Specifically, with single-phase charging, power varies from zero to twice the average power, which may stress the battery during charging. A DC-DC converter can vary its duty cycle at two times line frequency and in this way ensure constant power is delivered to the battery. The IGBTs, capacitors and parts of the DC bus must be rated for around 600V, but the remaining part of the DC bus including the battery can be rated for a lower voltage.

One interesting approach is to combine the AC and DC converter into a single unit using the Quazi Z-Source converter (QZSC) topology [19, 37]. This is illustrated in fig. 2.22. The goal is to boost the voltage v_{br} across the bridge. This is achieved by allowing a shoot-through state in which both switches in one leg conducts simultaneously. This is allowed because the inductors limit the short circuit current. It can be shown that the voltage boost is given by:

$$v_{br} = \frac{1}{1 - 2d} v_{DC} \, , \ 0 \leq d < 0.5 \tag{2.40}$$

Here, d is the duty cycle of the shoot-through state. When the duty cycle approaches 0.5 the voltage increases towards infinity. However, in reality, the voltage v_{br} can be boosted up to 2-3 times the DC battery voltage.

The challenges with this topology are that the shoot-through duty cycle limits the remaining time for the converter to operate as a normal three-phase bridge. That is, if the shoot-through duty cycle is 0.4, the converter bridge modulation index given later in eq. (2.54) must be 0.6 or less[6]. Furthermore, the combination of a capacitor and an inductor introduces a resonance frequency that, depending on the series resistances in the circuit, may be difficult to compensate for in the control circuit. However, one practical realization using this topology has been presented

---

[6]Theoretically, it may be a bit higher than this. See [53] for more on practical switching schemes.
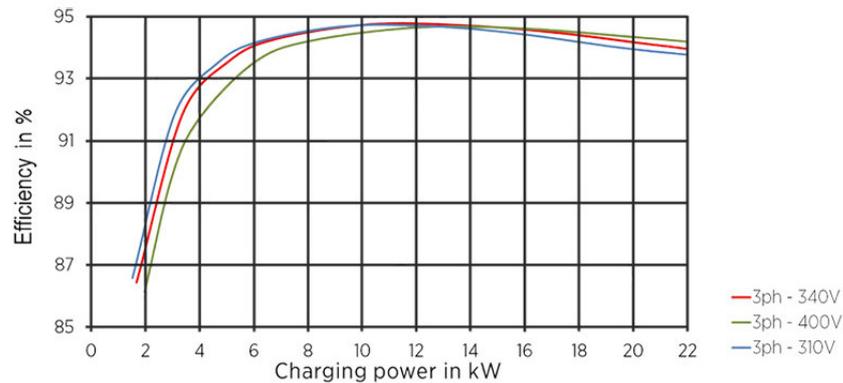
Figure 2.23: Efficiency curve of Brusa 22kW charger

in [37] in which an EV motor is supplied 85kW from a 200V battery, boosted to 400V across the bridge switches.

2.5.4 Efficiency

Some onboard EV converters have been reported to achieve quite low efficiencies when operating over a wide range of charging power levels. This does not seem to be relevant with DC fast-chargers, because they are always operated at maximum or close to maximum power rate.

Onboard EV chargers should ideally be able to work at power rates ranging from 230V/10A (2.3kW) in single-phase household outlets to 400V/63A three-phase (43kW) in charging stations. This is difficult to achieve with any converter design. As an example, the efficiency versus power level for a 22kW charger from Brusa is shown in fig. 2.23, and the efficiency is seen to derate at lower power rates. The problem with low efficiency at low power is not only power loss, but also increased charging time.

When using the motor drive as part of the charging circuit for low power charging, the components become somewhat overrated which implies higher switching and conduction losses than necessary. For example, MOSFETs would normally be used over IGBTs whenever possible due to lower losses. However, efficiency was found to be more than 98% in the simulations presented in section 2.7.2 using IGBTs. Practical experience has to be acquired on this subject.

2.5.5 THD

Low THD for unity power factor converters is achieved mainly through choosing an appropriate converter topology and precisely controlling the switches. There are at least four ways of decreasing THD if it turns out to be too high:

- Implement multi-level inverters so more than two voltage levels exist in the converter. This has been researched in [46].
- Use a larger inductor, or additional filter elements, to decrease current ripple.

- Increase switching frequency, which is a trade-off between additional switching loss and THD.

2.5.6 Challenges conclusion

Challenges with the three-leg three-phase converter topology have been presented in previous section, and ideas for solutions have been outlined.

In terms of efficiency, it is often difficult to construct a one-size-fits-all converter ranging over the wide power level that is required. Hence, it should be considered if two converters are needed: One for low and one for high power levels, where the latter could be based on integrating it with the motor drive. However, this approach should be avoided if possible because it would increase cost.

Based on the discussions presented in this section and the fact that some similar converter types are readily available on the market (e.g. Renault Zoe and AC Propulsion eBox), the three-phase topology seems like a viable approach.

2.6 Three-phase converter control

This section investigates how a three-phase three-leg converter is modulated and controlled. In section 2.3.1 it was described how power transfer through an inductor can be controlled by changing the voltage phasor on the converter side. The voltage phasor must be sinusoidal, and we will explore how this is achieved through space vector modulation, SVM. Eventually, the goal is to control the three-phase current flowing in and out of the converter, so a control circuit will be developed to achieve this.

2.6.1 Two-dimensional space vector modulation

A modulation strategy employing two-dimensional space vector modulation is developed in this section. Assuming the converter creates a three-phase balanced set of voltages, it holds that

$$v_a + v_b + v_c = 0 \tag{2.41}$$

This can be seen as a plane in three-dimensional space, where the sum of the coordinates of any point located on the plane is zero. A point on this plane can be described as components of two orthogonal vectors lying on the plane. These vectors are chosen by convention and known as the $\alpha\beta$ base vectors:

$$\vec{\alpha} = \frac{2}{3} \begin{bmatrix} 1 \\ -\frac{1}{2} \\ -\frac{1}{2} \end{bmatrix}, \ \vec{\beta} = \frac{2}{3} \begin{bmatrix} 0 \\ \frac{\sqrt{3}}{2} \\ -\frac{\sqrt{3}}{2} \end{bmatrix} \tag{2.42}$$

	ppp	nnn	pnn	ppn	npn	npp	nnp	pnp
v_α	0	0	$\frac{2}{3}$	$\frac{1}{3}$	$-\frac{1}{3}$	$-\frac{2}{3}$	$-\frac{1}{3}$	$\frac{1}{3}$
v_β	0	0	0	$\frac{\sqrt{3}}{3}$	$\frac{\sqrt{3}}{3}$	0	$-\frac{\sqrt{3}}{3}$	$-\frac{\sqrt{3}}{3}$

Table 2.5: Three phase converter switch states in (α, β) plane
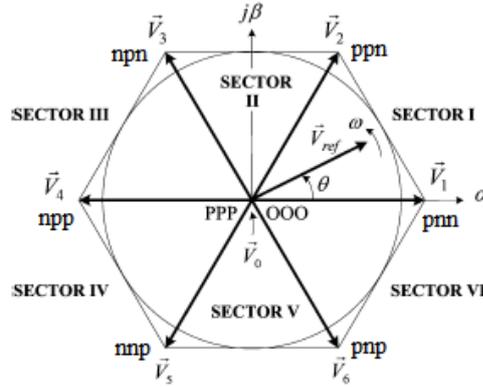
Figure 2.24: Switch states drawn in two-dimensional plane [71]

Thus, the transformation from a balanced set of voltages with components (v_a, v_b, v_c) can be transformed into a two-dimensional vector (v_α, v_β):

$$\begin{bmatrix} v_\alpha \\ v_\beta \end{bmatrix} = \frac{2}{3} \begin{bmatrix} 1 & -\frac{1}{2} & -\frac{1}{2} \\ 0 & \frac{\sqrt{3}}{2} & -\frac{\sqrt{3}}{2} \end{bmatrix} \begin{bmatrix} v_a \\ v_b \\ v_c \end{bmatrix} \tag{2.43}$$

For instance, we can transform the three-phase voltages generated by the three-leg two-level converter as was shown in table 2.2. The result is shown in table 2.5, and the vectors are drawn on the two-dimensional plane in fig. 2.24.

The idea of space vector modulation is to synthesize a reference three-phase voltage vector transformed to a two dimensional quantity using the vectors shown in fig. 2.24. A three-phase reference could be given by:

$$\vec{V}_{ref} = V_{ref} \begin{bmatrix} \cos(\omega t) \\ \cos(\omega t - \frac{2\pi}{3}) \\ \cos(\omega t - \frac{4\pi}{3}) \end{bmatrix} \tag{2.44}$$

Here, V_{ref} is the length (amplitude) of the reference voltage vector. Transforming this using eq. (2.43) yields:

$$\vec{V}_{ref,\alpha\beta} = \frac{2}{3} \begin{bmatrix} 1 & -\frac{1}{2} & -\frac{1}{2} \\ 0 & \frac{\sqrt{3}}{2} & -\frac{\sqrt{3}}{2} \end{bmatrix} V_{ref} \begin{bmatrix} \cos(\omega t) \\ \cos(\omega t - \frac{2\pi}{3}) \\ \cos(\omega t - \frac{4\pi}{3}) \end{bmatrix} = V_{ref} \begin{bmatrix} \cos(\omega t) \\ \sin(\omega t) \end{bmatrix} \tag{2.45}$$

Note the (α, β) reference vector resembles a circle with radius V_{ref}. This circle must be inscribed within the circle shown in fig. 2.24 for the converter to be able to synthesize this voltage vector. In that case, it is seen that at any point in time, there are three adjacent voltage vectors: two non-zero and a zero vector, denoted $\vec{V_1}$, $\vec{V_2}$ and $\vec{V_0}$. A reference voltage vector can then be synthesized by switching quickly (much higher than the AC frequency) between these adjacent voltage vectors. The voltage-second balance can be used to express the reference vector:

$$\vec{V}_{ref,\alpha\beta} \cdot T_s = T_1 \cdot \vec{V_1} + T_2 \cdot \vec{V_2} + T_0 \cdot \vec{V_0} \tag{2.46}$$

Here, T_s is the switching period chosen in a given converter design. Dividing by this on both sides yields the duty cycles for each switch state:

$$\vec{V}_{ref,\alpha\beta} = d_1 \cdot \vec{V_1} + d_2 \cdot \vec{V_2} + d_0 \cdot \vec{V_0} \tag{2.47}$$

Furthermore, the duty cycles always sum to 1:

$$d_1 + d_2 + d_0 = 1 \tag{2.48}$$

Inserting eq. (2.45) and the space vectors V_1 (pnn) and V_2 (ppn) from table 2.5 into eq. (2.47) yields:

$$V_{ref} \cos(\omega t) = \frac{2}{3} d_1 v_{DC} + \frac{1}{3} d_2 v_{DC} \tag{2.49}$$

$$V_{ref} \sin(\omega t) = \frac{\sqrt{3}}{3} d_2 v_{DC} \tag{2.50}$$

These are solved for d_1, d_2 and d_0 by using eq. (2.48). From eq. (2.50) we get:

$$d_2 = \frac{\sqrt{3} V_{ref} \sin(\omega t)}{v_{DC}} \tag{2.51}$$

By inserting eq. (2.51) into eq. (2.49) we get:

$$\frac{2}{3} d_1 v_{DC} = V_{ref} \cos(\omega t) - \frac{1}{3} \frac{\sqrt{3} V_{ref} \sin(\omega t)}{v_{DC}} v_{DC}$$
$$d_1 = \frac{3}{2} \frac{V_{ref}}{v_{DC}} \left(\cos(\omega t) - \frac{\sin(\omega t)}{\sqrt{3}} \right) \tag{2.52}$$
$$= \frac{\sqrt{3} V_{ref}}{v_{DC}} \cos\left(\omega t + \frac{\pi}{6} \right)$$

Finally, using eq. (2.48) we have:

$$d_0 = 1 - d_1 - d_2 \tag{2.53}$$

Here, the factor

$$m = \frac{\sqrt{3}V_{ref}}{v_{DC}} \tag{2.54}$$

is known as the modulation index and must be less than or equal to 1 for the reference vector to be synthesized. Note above equations are only valid for a reference vector in sector 1. When the reference vector is located in other sectors, its corresponding angle in sector 1 can be found by a modulus operation and the equations can be reused.

2.6.2 Control of two-dimensional SVM

Using SVM, the converter can synthesize any balanced three-phase set of voltages at any given frequency. However, we have to determine the reference vector the converter is to synthesize.

When the converter is connected to the grid, the grid voltage phasor must be tracked by the converter as explained using phasor diagrams in section 2.3.1. This means the converter must track a sinusoidally varying quantity, which is generally difficult with conventional controllers such as P, PI and PID regulators. Hence, it simplifies the control part if the rotating vector can be transformed into a constant non-rotating vector. This is done using the so called *dq* transform and it consists of a transformation matrix that rotates along with the voltage vector defined in α, β components:

$$\begin{bmatrix} v_d \\ v_q \end{bmatrix} = \begin{bmatrix} \cos\phi & \sin\phi \\ -\sin\phi & \cos\phi \end{bmatrix} \begin{bmatrix} v_\alpha \\ v_\beta \end{bmatrix} \tag{2.55}$$

The transformation can be done from *abc* components directly to *dq* components if eq. (2.43) is inserted into eq. (2.55):

$$\begin{bmatrix} v_d \\ v_q \end{bmatrix} = \frac{2}{3} \begin{bmatrix} \cos(\phi) & \cos(\phi - \frac{2\pi}{3}) & \cos(\phi - \frac{4\pi}{3}) \\ -\sin(\phi) & -\sin(\phi - \frac{2\pi}{3}) & -\sin(\phi - \frac{4\pi}{3}) \end{bmatrix} \begin{bmatrix} v_a \\ v_b \\ v_c \end{bmatrix} \tag{2.56}$$

Here, ϕ is an angle tracking that of the grid, so ideally $\phi = \omega t$. This implies the grid voltage phasor has to be determined, which may be difficult in practice since the grid contains harmonics and frequency fluctuations. A phase locked loop (PLL) can be employed to take care of voltage angle tracking, which can be implemented in a number of ways depending on requirements, see [38]. In this project, it was chosen to implement a simple grid voltage angle tracker while assuming low distortion on grid voltage (which is easily done in a simulation). The angle tracker entails measuring the three phase voltages, transforming them to an α, β vector and calculating the angle of this rotating vector as

$$\phi = \tan^{-1} \frac{v_\beta}{v_\alpha} \tag{2.57}$$

Thus, this angle can be used in the *dq* transform in eqs. (2.55) and (2.56).

Applying Kirchoff's voltage law to the converter's single line diagram in fig. 2.11 for each phase yields the following three equations:

$$\begin{bmatrix} v_{g,a} \\ v_{g,b} \\ v_{g,c} \end{bmatrix} = R \begin{bmatrix} i_a \\ i_b \\ i_c \end{bmatrix} + L \frac{d}{dt} \begin{bmatrix} i_a \\ i_b \\ i_c \end{bmatrix} + \begin{bmatrix} v_{c,a} \\ v_{c,b} \\ v_{c,c} \end{bmatrix} \tag{2.58}$$

Here, v_g is a grid voltage (either phase), and v_c is the converter voltage (either phase). These equations can be *dq* transformed using eq. (2.56). The detailed derivations are shown in appendix E, and the result is as follows:

$$v_{g,d} = L \frac{di_d}{dt} + v_{c,d} + Ri_d - L\omega i_q \tag{2.59}$$

$$v_{g,q} = L \frac{di_q}{dt} + v_{c,q} + Ri_q + L\omega i_d \tag{2.60}$$

Using the Laplace transformation yields:

$$v_{g,d} = i_d(sL + R) + v_{c,d} - L\omega i_q \tag{2.61}$$

$$v_{g,q} = i_q(sL + R) + v_{c,q} + L\omega i_d \tag{2.62}$$

We can define two new quantities v_d', v_q':

$$v_d' = v_{g,d} - v_{c,d} + L\omega i_q \tag{2.63}$$

$$v_q' = v_{g,q} - v_{c,q} - L\omega i_d \tag{2.64}$$

Inserting v_d', v_q' into eqs. (2.61) and (2.62) and solving for the currents yield:

$$\frac{i_d}{v_d'} = \frac{1}{sL + R} \tag{2.65}$$

$$\frac{i_q}{v_q'} = \frac{1}{sL + R} \tag{2.66}$$

The reference voltage vector v_c in *dq* coordinates for the converter will therefore be given by:

$$v_{c,d} = -v_d' + v_{g,d} + L\omega i_q \tag{2.67}$$

$$v_{c,q} = -v_q' + v_{g,q} - L\omega i_d \tag{2.68}$$
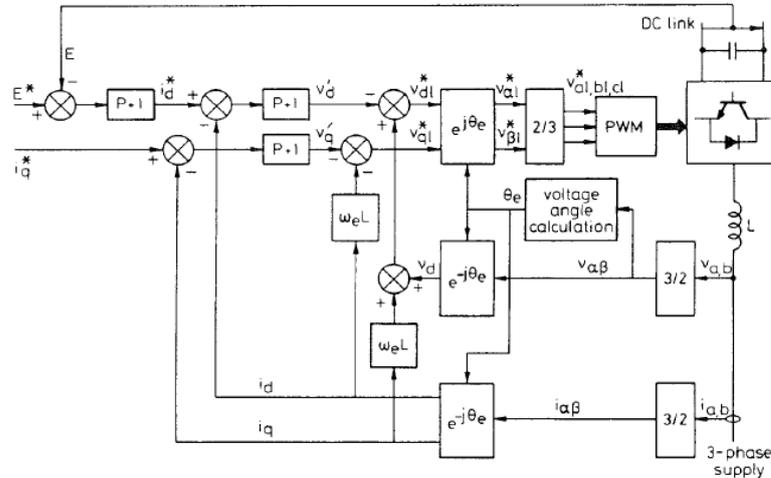
Figure 2.25: Three-phase converter control using dq transform [61]

With eqs. (2.65) to (2.68) it is possible to calculate the converter reference voltage vector which is synthesized using the SVM strategy as explained in the previous section. The complete control and modulation strategy is visualized in fig. 2.25.

2.6.3 Voltage sags

The location at which an EV is charged cannot be known in advance, and it cannot be known how strong the grid is at this location. If the phases are loaded unequally by other single-phase equipment connected nearby then voltage may differ between phases. This is currently not supported by the control circuit presented in the last section, because it assumes the three-phase voltage to be equal in amplitude. We can alter the controller slightly to support per-phase voltage sags with *symmetrical components* theory.

Using symmetrical components theory, any unbalanced set of three-phase voltages can be decomposed into three sets of balanced components, namely, positive-sequence, negative-sequence and zero-sequence components [36]. The transformation matrix for doing so can be expressed as

$$a = e^{j\frac{2\pi}{3}} \tag{2.69}$$

$$\begin{bmatrix} V_p \\ V_n \\ V_h \end{bmatrix} = \frac{1}{3} \begin{bmatrix} 1 & a & a^2 \\ 1 & a^2 & a \\ 1 & 1 & 1 \end{bmatrix} \begin{bmatrix} V_a \\ V_b \\ V_c \end{bmatrix} \tag{2.70}$$

Here, V_p is the positive sequence component, V_n is the negative sequence component, V_h is the zero-sequence or homopolar component and V_a, V_b, V_c are the phasors for the three phases a, b and c. Dealing with phasors, all quantities are expressed as complex numbers. As illustrated in fig. 2.26, the positive sequence phasors are always balanced and with phasors a,b,c shifted 120° in forward (positive) direction. The negative sequence phasors are balanced and shifted 120° but in reverse direction. The zero sequence phasors are in-phase and unbalanced.
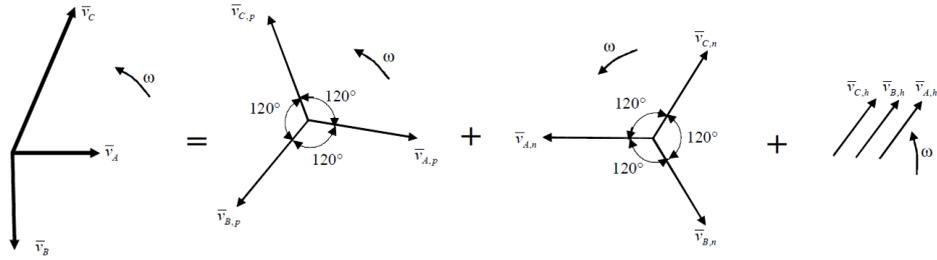
Figure 2.26: Any unbalanced voltage can be decomposed into positive, negative and homopolar components [66]
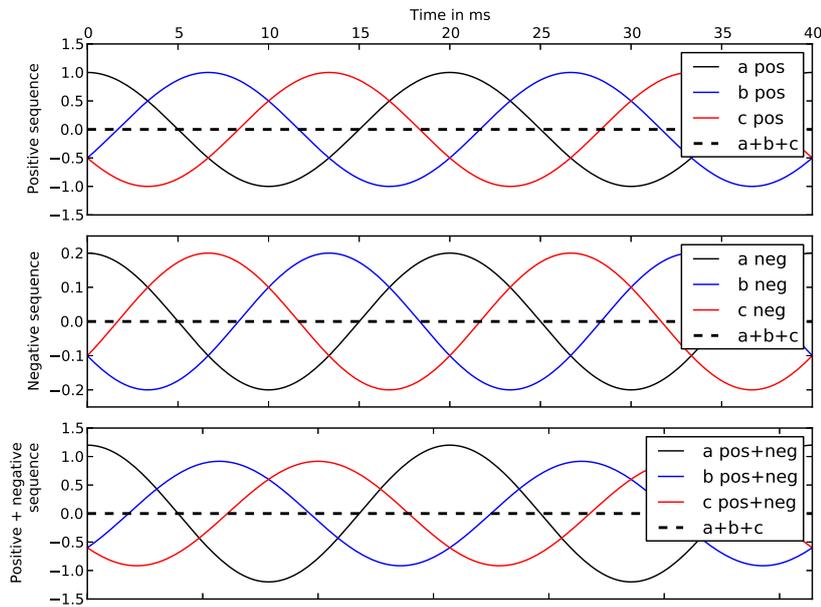
Figure 2.27: Example of positive, negative components and their sum

Notice the zero-sequence component is given by $V_h = \frac{1}{3}(V_a + V_b + V_c)$. Hence, the zero-sequence component determines whether a system is unbalanced or not, and a non-zero zero-sequence component implies unbalance. This is not the case with positive and negative sequence components since they can attain any value and the system remains balanced. For instance, on fig. 2.27 it is evident that the sum of both the positive and negative sequence component sinusoids is zero. Therefore, the three-leg converter is fundamentally capable of synthesizing a voltage consisting of positive and negative sequence components, but not zero-sequence.

A three-phase three-wire system is always balanced because there is no path for zero-sequence currents without a neutral wire. Therefore, the previous control circuit can be extended to decompose the voltages and currents into positive and negative sequence components, control these quantities, and sum the components to yield the $\alpha\beta$ voltage reference phasor. This is still synthesizable by 2D SVM.

The controller will in this case use dq-transformation, but negative sequence components use a reverse rotational transformation, which according to appendix E and eqs. (2.67) and (2.68) changes the sign of the decoupling term in the control
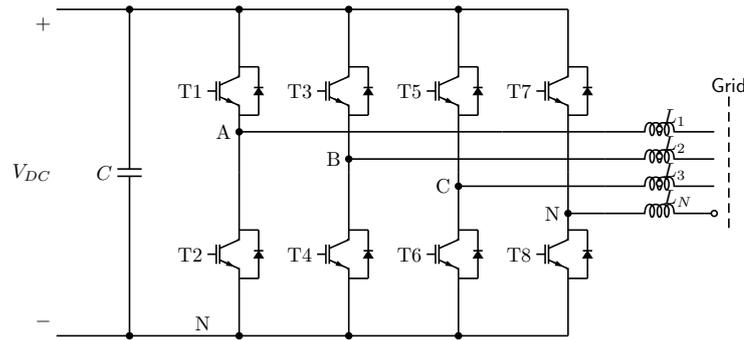
Figure 2.28: Three phase four-wire grid connected converter

circuit (i.e. $+L\omega i_{q,p}$ becomes $-L\omega i_{q,n}$ where subscript p denotes positive components and n denotes negative sequence components):

$$v'_{d,n} = v_{g,d,n} - v_{c,d,n} - L\omega i_{q,n} \tag{2.71}$$

$$v'_{q,n} = v_{g,q,n} - v_{c,q,n} + L\omega i_{d,n} \tag{2.72}$$

Apart from this, there is no change to the control circuit shown in fig. 2.25 and is therefore easily implemented.

2.6.4 Three-dimensional space vector modulation

In the previous sections it was assumed the generated three-phase three-wire converter voltages were balanced, that is, $v_a + v_b + v_c = 0$. However, that may not always be the case. For example, in the case of single-phase charging we have $v_a \neq 0$ and $v_b = v_c = 0$, so this system is not balanced. During faults, one or two phases may de-energize which also results in an unbalanced system. If we in this case want to keep charging, we must take zero-sequence components into account. This means we must let a current flow in the neutral wire, and a fourth leg must be added to the converter, as shown in fig. 2.28.

With the fourth leg added to the converter, any type of balanced or unbalanced three-phase or single-phase load is supported. Specifically, beyond single-phase support, there are two use cases in which this capability is necessary:

- In *grid-forming mode*, the converter is set to charge or discharge with unbalanced currents based on the unbalance in phase voltages. E.g., if voltage sags on one phase (say L3), we can charge at full current on phase L1 and L2 but with less current on L3. Conversely, the converter can supply power to the grid to restore balance in phase voltages.
- In three-phase *vehicle to load* (V2L) the converter can supply power to an islanded grid, e.g. a home during a grid power outage, which may be highly unbalanced and contain many single-phase loads and appliances.

Note the same effect can be achieved using a three-wire to four-wire low-frequency distribution transformer. However, this may in some cases be too impractical to use
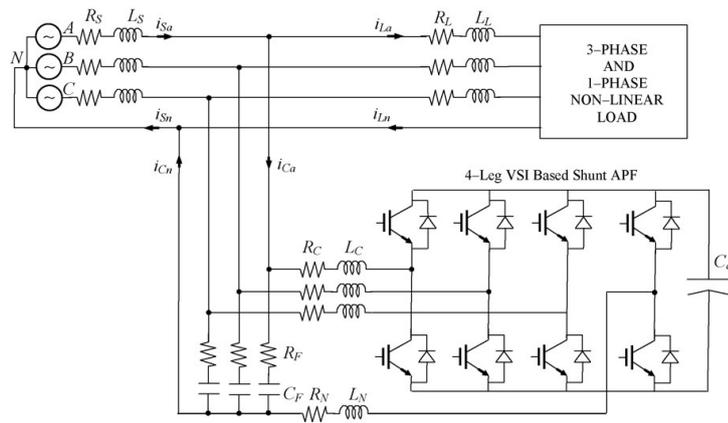
Figure 2.29: Active power filter topology [65]

due to its bulky size. Hence, the four-leg converter with unbalanced grid capability is an ideal alternative.

The four leg inverter has been described in papers [57, 67, 72]. Often, the four leg inverter is used as an *active power filter* (APF) where unbalanced grid currents are minimized and ideally achieves perfectly balanced currents after the APF, that is, current i_L in fig. 2.29 [65]. This can be achieved with little or no energy storage, so only a few capacitors are needed on the DC bus. Various control schemes have been developed for reference voltage phasor estimation [49, 50]. However, the barrier for EV applications is that an APF measures the currents that it is to restore balance to. Hence, the phase currents i_L as shown in fig. 2.29 are used in the control circuit, and they will generally not be available for the onboard EV converter. This quickly eliminates the possibility of using EVs in APF applications. Note in grid-forming mode, the current is controlled based only on grid voltages and is therefore possible to implement in EVs.

With single-phase charging, power fluctuates with two times line frequency. In case only active power is transferred then it varies between zero and twice the average power. Single-phase operation is the most extreme case of varying power transfer. The other extreme is constant transferred power which is achieved during purely positive-sequence balanced three-phase operation. Hence, any converter operation between these two extremes yields fluctuating power, but with a higher percentage of positive-sequence component the power will fluctuate less (shown in simulations in section 2.7). That is, if the converter supplies balanced current with both positive and negative sequence components, the power fluctuates. This must be kept in mind when assessing stress on battery during charging. If only constant power is desired in any operation mode then a DC-DC converter must be placed in between the battery and the converter bridge.

2.6.5 Control of three-dimensional SVM

With unbalanced three-phase voltages, the sum of the phasors do not yield zero, and hence, the phasors are not located on the plane given by $v_a + v_b + v_c = 0$. This means the phasors are located outside the two-dimensional plane spanned by the $\alpha\beta$ vectors, and we must add a third dimension to successfully decompose the phasors.
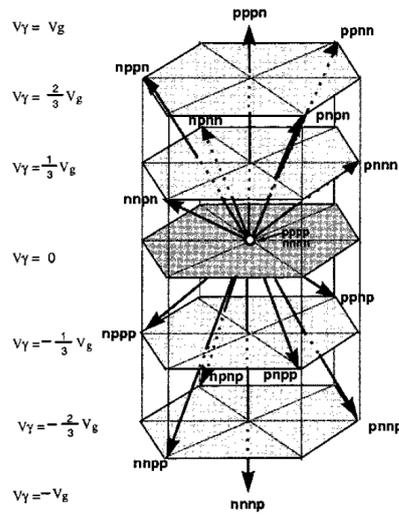
Figure 2.30: Three-dimensional space vectors [72]

A vector normal to this plane is known as the γ vector and is by convention given by:

$$\vec{\gamma} = \frac{2}{3} \begin{bmatrix} \frac{1}{2} \\ \frac{1}{2} \\ \frac{1}{2} \end{bmatrix} \tag{2.73}$$

The three-dimensional $\alpha\beta\gamma$ transform is thus given by:

$$\begin{bmatrix} v_\alpha \\ v_\beta \\ v_\gamma \end{bmatrix} = \frac{2}{3} \begin{bmatrix} 1 & -\frac{1}{2} & -\frac{1}{2} \\ 0 & \frac{\sqrt{3}}{2} & -\frac{\sqrt{3}}{2} \\ \frac{1}{2} & \frac{1}{2} & \frac{1}{2} \end{bmatrix} \begin{bmatrix} v_a \\ v_b \\ v_c \end{bmatrix} \tag{2.74}$$

With the reference vector expressed in three-dimensional $\alpha\beta\gamma$ components, the converter will not be able to synthesize this with 2D SVM. Instead, 3D SVM must be used, where 3D SVM can be seen as a superset to 2D SVM. Its implementation is very similar to 2D SVM as described in section 2.6.1, in that it must estimate the location of the reference vector and synthesize it by projecting it to adjacent vectors realizable by the converter. In case of 3D SVM, there will be three active vectors and a zero vector adjacent to any reference vector. The 3D SVM vectors in $\alpha\beta\gamma$ components are shown in fig. 2.30 [72]. 2D SVM vectors were located in sectors (1-6), whereas 3D vectors are located in prisms (1-6) each with 4 tetrahedrons, and there are thus 24 possible reference vector locations. This makes it somewhat more laborious to calculate the vector projections. Fortunately, this has been addressed in [72], where transformation matrices are defined for each of the 24 tetrahedrons relating $\alpha\beta\gamma$ components with dwell times, which makes it relatively easy to implement.

Including the third γ dimension enables synthesis of zero-sequence components. Hence, the 3D control circuit must add a third zero-sequence controller for its reference vector generation.

2.6.6 Three-phase converter control conclusion

The three approaches described in the previous section can be summarised as follows:

1. Three-leg converters utilizing two-dimensional SVM with a single *dq* controller are capable of synthesizing positive-sequence three-phase voltages. In this case, the converter does not work well with unbalanced grids. The converter currents only consist of positive sequence components and is always balanced.

2. Three-leg converters utilizing two-dimensional SVM with dual *dq* controllers are capable of synthesizing positive and negative-sequence three-phase voltages. In this case, the converter works well with unbalanced grids. The converter three-phase currents may consist of positive and negative sequence components and are always balanced. Hence, single-phase operation is not implicitly supported.

3. Four-leg converters utilizing three-dimensional SVM with triple *dq* controllers is capable of synthesizing positive, negative and zero-sequence three-phase voltages. In this case, the converter works well with unbalanced grids. The converter currents can be controlled per-phase, completely independent of each other, single-phase or three-phase. This enables EV converters to support *grid-forming mode* and three-phase V2L applications.

Simulations of each of these types of operation are shown in the following section 2.7.

2.7 Simulations

Three simulations have been set up using the Simulink graphical environment under Matlab. This software tool is capable of simulating both electric circuits, modulation and control simultaneously, so the simulation results get relatively close to what would be implemented in practice. The three simulations share many components, so only the differences between the simulations will be explained. Furthermore, only select results from each simulation will be presented here. For more results and implementation details, the simulation files should be acquired and explored. The simulation results shown and discussed here will show the following features:

1. Basic properties of three-phase charging, including constant power transfer.

2. Minimum DC bus voltage requirement.

3. Four-quadrant power flow according to theory presented in section 2.3.1.

4. The controller and modulation works as explained in section 2.6.

5. The inductor as designed in section 2.4.3 is reasonably dimensioned.

6. Basic efficiency figures during high and low power charging.

7. Unbalanced grid voltages and converter operation based on symmetrical components decomposition.
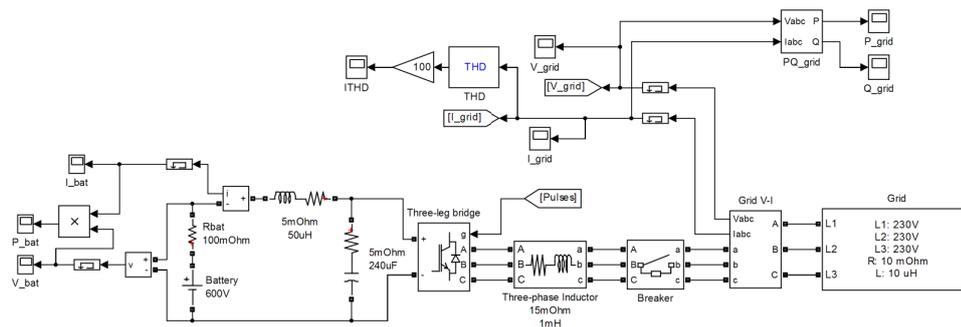
Figure 2.31: Electric circuit used in simulations with measurements and THD estimation

8. Unbalanced grid voltages and four-leg converter operation with 3D SVM, enabling per-phase current control.

9. Single-phase charging, which is a special case of an unbalanced system.

No separate DC-DC converter has been simulated, since this is considered outside the scope of this project. It is also outside the scope of this project to precisely estimate PI controller parameters. The controllers have been tuned by hand, so it is likely that better P and I parameters could be found. However, the control part will work acceptably anyway. Also, finding a "best solution" for PI parameters in the simulation would probably not apply in practice.

2.7.1 Electric component values

The circuit used for most simulations is shown in fig. 2.31 along with measurements of voltages, currents, THD and power.

The DC bus is located on the left, where the battery voltage is set to 600V and a series resistance of 100mΩ is assumed. A small series inductor is placed on the DC bus to remove current ripples from the bridge switches. This is set to $50\mu H$ with a 5mΩ series resistance. The DC bus capacitance component values are based on using film capacitors which have very small ESR. One possible component could be the Epcos 800V 60μF with an ESR of 3mΩ, part no. B32776E8306. Four of those would be placed in parallel to achieve 240μF and one fourth the ESR. However, due to resistance in connectors and terminals in practice, an ESR of 5mΩ is assumed.

The three-leg bridge is found as a single component in Simulink, and it can in practice also be found in a single pack. For example, the Infineon IGBT module with part no. FS100R12PT4 includes six IGBTs in a three-leg configuration rated for 1200V. The continous rated forward current is 100A, and the forward voltage drops across the IGBT and diode are typically 2.05V and 1.65V, respectively, which is therefore put into the simulation. The on-resistance is found from the datasheet to be around 8mΩ at 25°C. The turn-on and turn-off switching times are around 0.5μs and since the time step of the simulation is 1μs, this switching time is entered as a worst-case scenario.

The three inductors are put into the simulation based on the previous results in
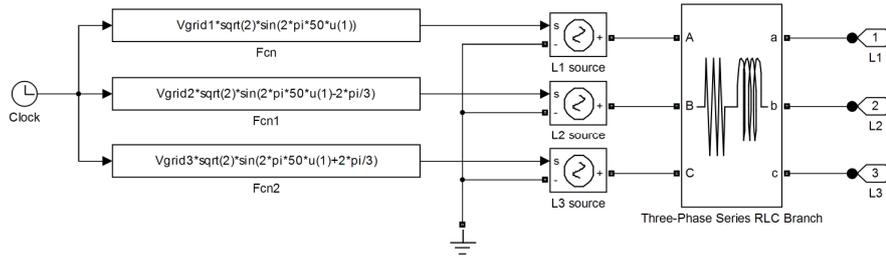
Figure 2.32: Grid model
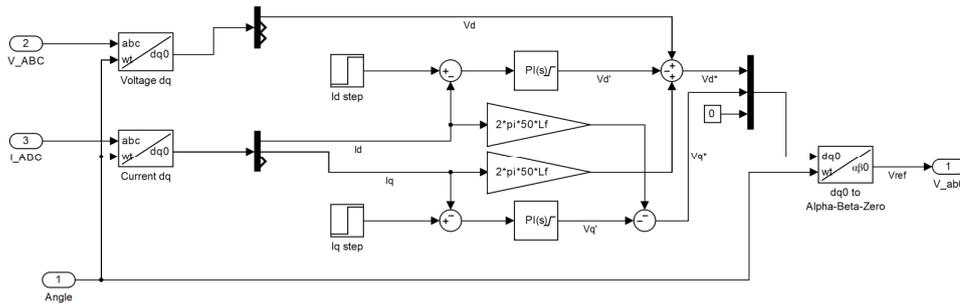
Figure 2.33: Single *dq* controller implemented in Simulink

section 2.4.3. The inductance is set to 1mH and the series resistance is 15mΩ. A breaker is placed between the grid and the converter to start the converter at a specific point in time (e.g. after 10ms of simulation time). A three-phase measurement of currents and voltages is located after the breaker on the grid side of the converter. The measurements are used for estimating active and reactive power transfer to the grid, current THD, and for the control circuit as explained later.

The grid block is shown in fig. 2.32. The grid is modelled as three voltage sources emitting sinusoids spaced 120° apart. A series inductance and resistor is located between the voltage sources and the three-phase output. The values are relatively low, suggesting the converter is connected to a strong grid. This assumption will be used for this simulation, since a weaker grid introduces harmonics and noise on the grid lines, meaning the control circuit has to reject this, which is outside the scope of this simulation.

The memory blocks (the small rectangles with a line and an arrow in it) placed after a measurement speed up simulation. They delay a measurement by one sample period, i.e. 1μs. The measurements *P_grid* and *P_bat* are used to estimate the efficiency of the converter as $\eta = \frac{P\_bat}{P\_grid}$ in charging mode.

2.7.2 Simulation 1: Three-leg single controller

The first simulation implements 2D SVM with a single *dq* controller, shown in fig. 2.33. On the left, the grid voltage and current is transformed to *dq*0 quantities based on the grid angle, which is found from eq. (2.57) and shown in fig. 2.34. The *dq* control structure can be recognized from fig. 2.25, and the reference voltage is calculated on the right by a *dq* to $\alpha\beta$ components transformation.
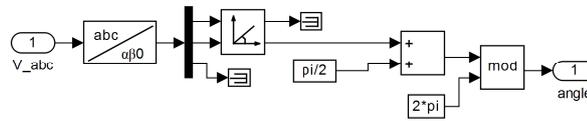
Figure 2.34: Grid angle calculation

The reference vector is synthesized by SVM as shown in fig. 2.35 running at a switching frequency of $f_s = 24\text{kHz}$. Here, the reference vector is the input signal on the left. This input signal is held constant at the beginning of each sample period using the S/H block. Afterwards, the sector (1-6) is determined from the angle of the reference voltage (fig. 2.24). The dwell time for each space vector is found in the dwell time block, expanded in fig. 2.36. This is seen to be based on eqs. (2.51) to (2.53). To the right in the dwell time calculation block, a minimum switch time of $2\mu s$ is imposed to prevent very fast switchings, which reduces switching losses but may increase THD slightly.
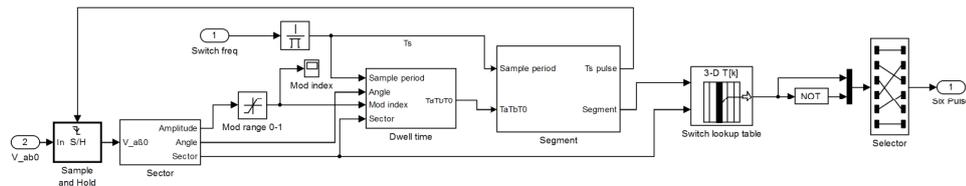
Figure 2.35: Space vector modulation overview
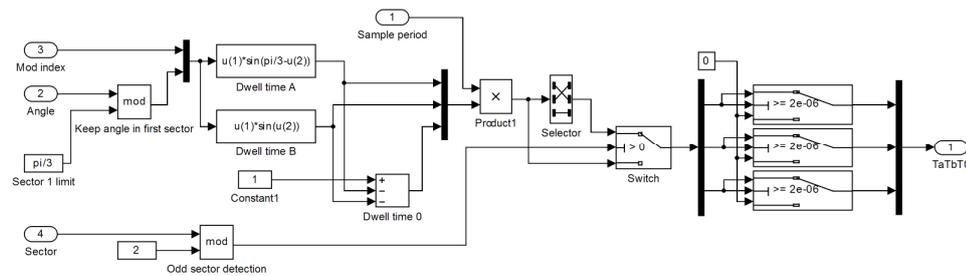
Figure 2.36: Inside dwell time calculation block

The segment block translates the calculated dwell times into signals in time. That is, for each switching period, $\frac{1}{f_s}$, the converter cycles through 7 segments each representing a space vector. The time average of the space vectors yield the reference vector for each point in time. The segments, switch states and corresponding dwell times are shown in fig. 2.37. Based on the segment determination, a lookup table is used to figure out the corresponding switches that are to be turned on and off. Since the two switches in an inverter leg are always operated inversely, we only have to find the switch state of three of the six switches (e.g. the upper switches) in the lookup-table and perform a negating operation to find the rest. These are then passed to the three-leg bridge.
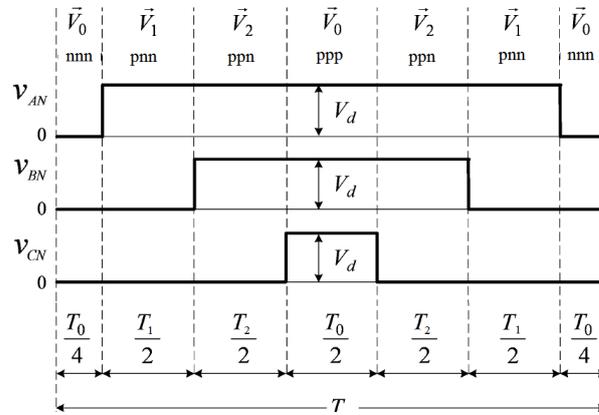
Figure 2.37: Segment determination for each switching cycle in sector 1 [71]
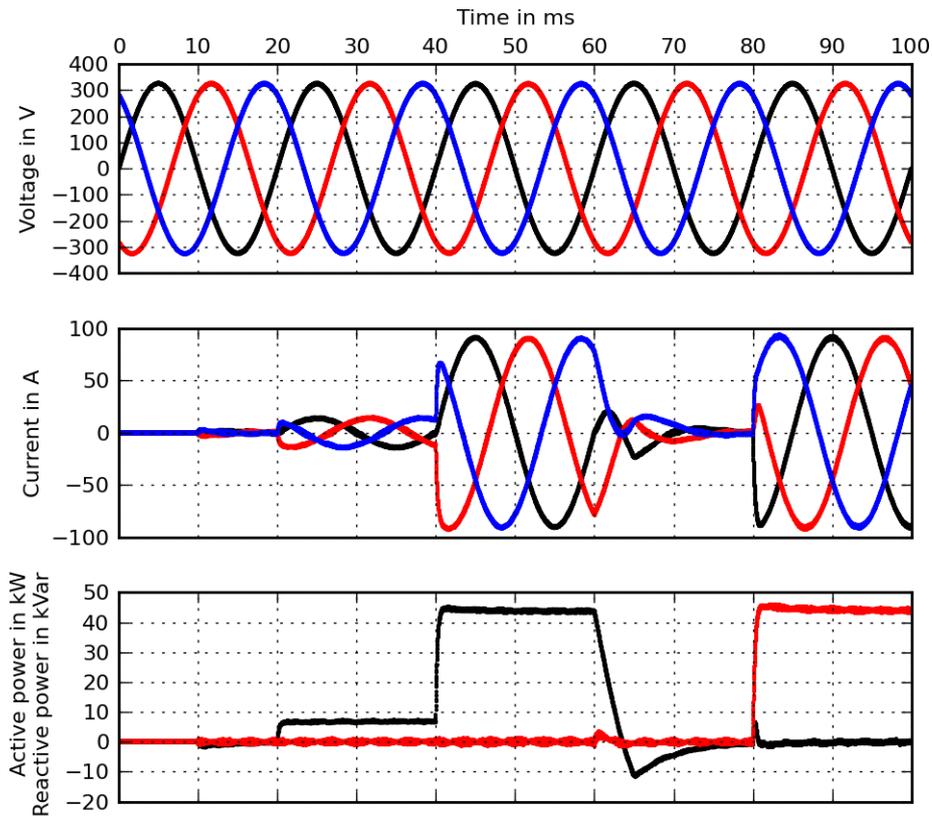
Figure 2.38: Simulation one with balanced grid and three-phase charging
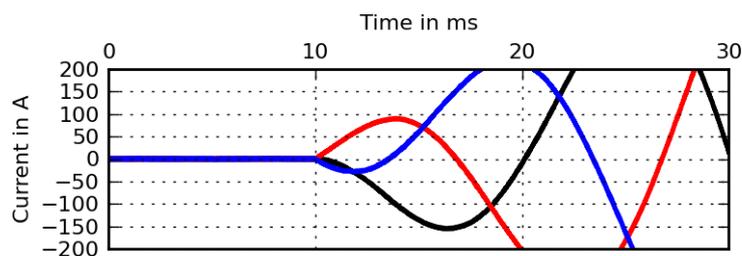
Figure 2.39: Simulation with 500V battery. The current increases uncontrollably

A simulation is run using this model, shown in fig. 2.38. The three-phase grid voltages are shown at the top, the currents in the middle and active (black) and reactive power (red) on the bottom. The simulation runs for 100ms. Initially, the current reference is set to zero when the breaker closes after 10ms. At 20ms, the d current reference is stepped to 10A rms, in which case the active power transfer is $3 \cdot 230V \cdot 10A = 6.9kW$. At 40ms, the current is stepped to 63A rms, in which case the power transfer is 43kW. Notice no reactive power is exchanged at this point. At 60ms, the current is set to zero and it takes approximately 15ms to settle. At 80ms, the q current reference is stepped to 63A rms, and the reactive power is now 43kVar while the active power remains close to zero.

The efficiency was in the time window 20-40ms measured to 99.5% and in the time window 40-60ms 98.6%, that is, a power loss around 600W. The THD was measured to 6.4% during low power transfer and 1.0% during high power transfer. Hence, the THD is a bit higher at low power, which would be a reason for using a higher inductance or higher switching frequency at this power rate.

Note the current is in phase with the voltage when active power is transferred and the current lags by 5ms, 90°, when reactive power is transferred. It is also clear that power is constant, one of the merits of three-phase charging. It is easily imagined that by setting the current reference to negative 63A rms, active power will flow from the battery to the grid, thus enabling V2G.

The minimum DC bus voltage requirement can be clarified by running a simulation at a too low battery voltage, here 500V. In this case, the voltage across the converter inductor cannot be kept at the same level as the grid voltage, and hence, when the breaker opens after 10ms, the current increases uncontrollably. In practice, a fuse or breaker would trip, and the converter would not work. The phase currents with a 500V battery are shown in fig. 2.39.

Now, assume a voltage sag appears on one phase, so the voltage is 75% of nominal value. A new simulation is run, shown in fig. 2.40. Notice the current is distorted, and power varies with two times line frequency. The THD is now 5%, increasing from 1% from previous run. This is obviously undesirable, but can be handled by using symmetrical components as will be shown next.
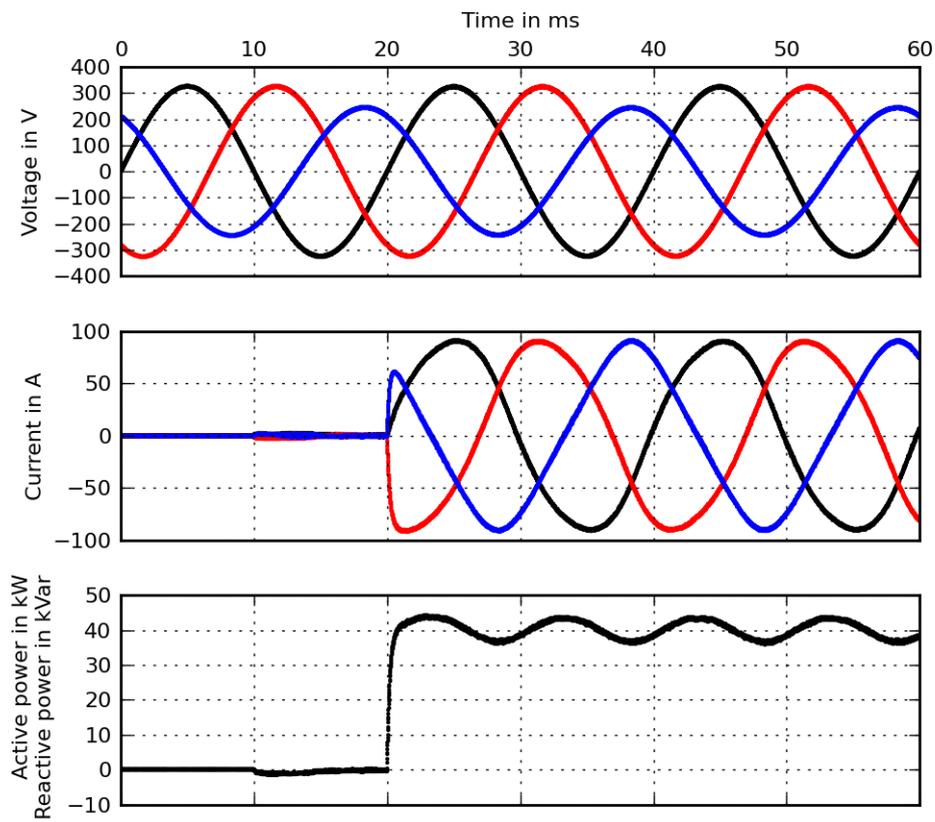
Figure 2.40: Simulation 1 with unbalanced grid. Note the distortion of the current, which increases THD
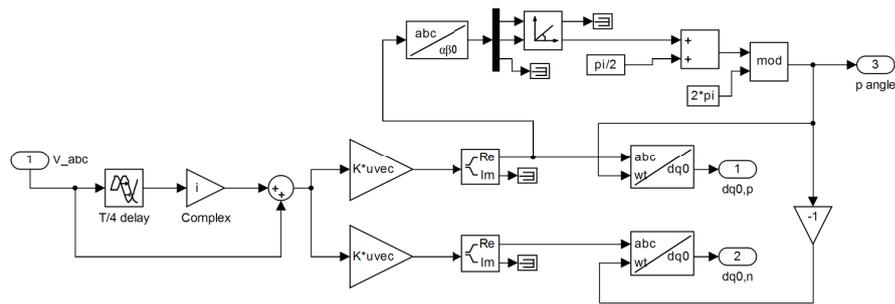
Figure 2.41: Positive and negative sequence decomposition

2.7.3 Simulation 2: Three-leg dual controller

The control part of the simulation is modified to use two *dq* controllers, using positive and negative sequence components. The symmetrical components decomposition is described in [67] and shown in fig. 2.41. The voltage is delayed by one fourth of a grid period, multiplied by the imaginary unit, thus turning the grid voltage into a phasor quantity that can be used with the symmetrical components decomposition matrix (eq. (2.70)). Notice the grid voltage angle is now determined solely from the positive sequence component.

With the same voltage sag as in previous simulation, the currents and power obtained are shown in fig. 2.42. Notice the current is now sinusoidally shaped even though the voltage is unbalanced. Both active and reactive power varies, which has to be accepted when interfacing an unbalanced grid.

Note only the control part has been modified in order to interface an unbalanced grid, that is, it is mostly a matter of software in practice. Hence, this should be implemented in any grid interfacing converter.

2.7.4 Simulation 3: Four-leg triple controller

If unbalanced current should flow then a fourth leg is required in the bridge, and three-dimensional SVM must be utilized to synthesize the reference vector. The zero-sequence component must also be controlled, so a third controller is added [57]. The implementation of three-dimensional SVM is described in [72].

As an example of the capabilities of this converter topology and controller, a simulation is run with varying current references for each phase as shown in fig. 2.43. After 20ms, the current reference is ramped up to 63A rms in 5ms in each phase, yielding the same current and power as shown in earlier simulations. Hence, the charge rate is 43kW when the currents have settled after 40ms. There is a small overshoot in the current PI controllers, which is seen to be eliminated after approximately 10ms, i.e. at 35ms simulation time.

At 60ms, the current reference is set to zero for two phases, leaving one phase with a 63A rms current setpoint. This corresponds to single-phase charging, which can be seen is highly unbalanced with the neutral current equal to the single-phase current with opposite sign. The active power varies between zero and twice the
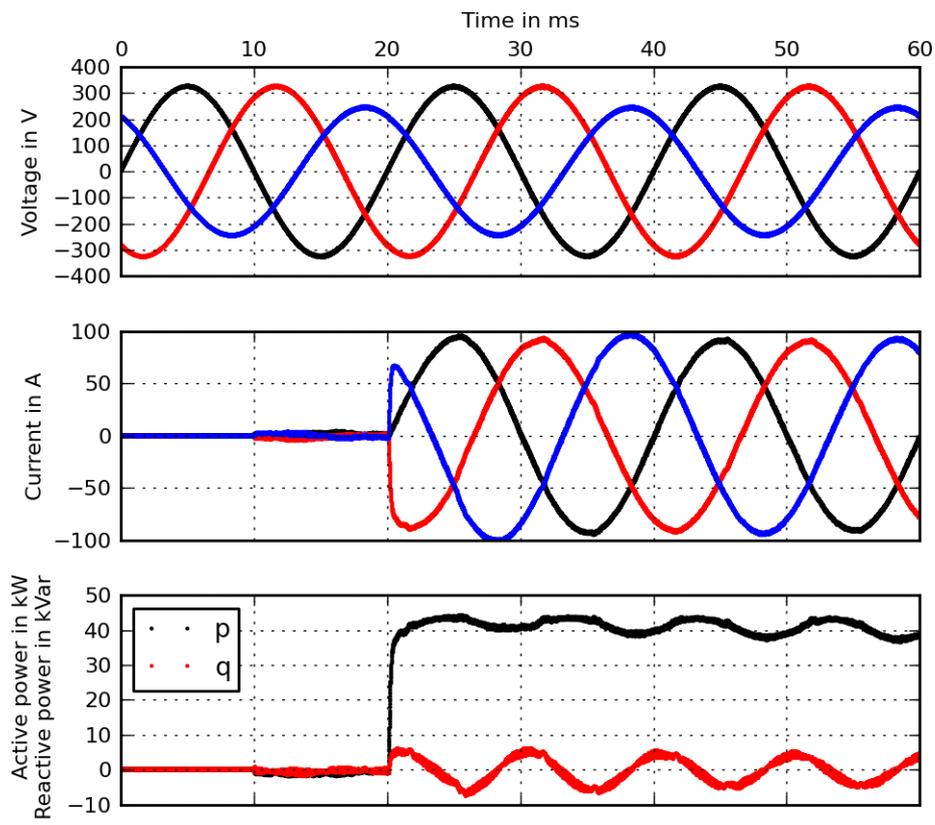
Figure 2.42: Simulation 2 with unbalanced grid. Note the currents are balanced and sinusoidal
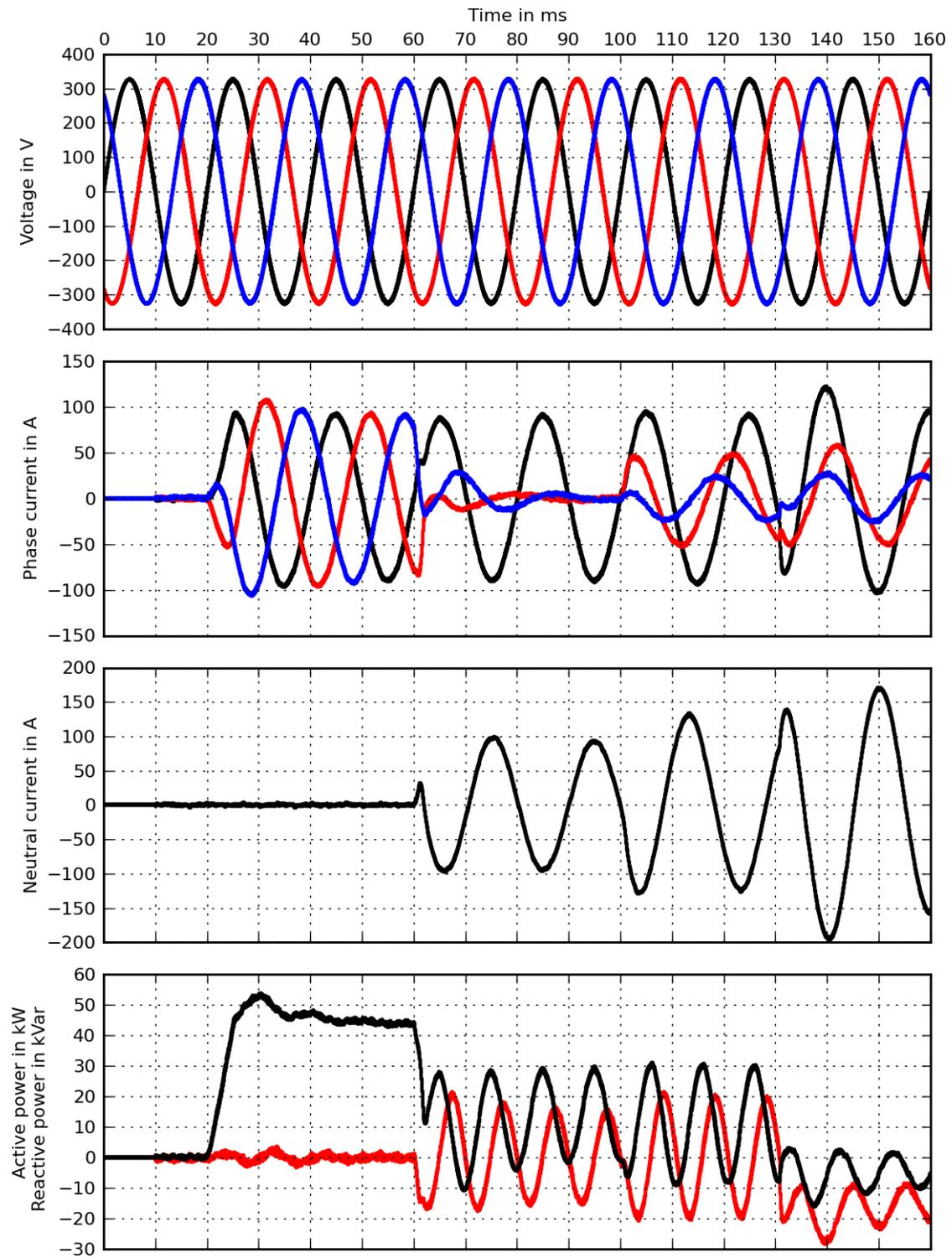
Figure 2.43: Simulation 3 with four-leg converter and per-phase current control

average power after the current has settled at 80-100ms. The average power is $230\text{V}\cdot 63\text{A} = 14.5\text{kW}$. It is seen the reactive power varies as well, which is not true in reality because the current is in phase with the voltage and hence reactive power should be zero. This is a limitation in the power measurement block in Simulink.

At 100ms, the current is left at 63A rms in the first phase, -32A rms in the second phase and 16A in the third phase. That is, one phase discharges the battery into the grid whereas the other two charges it. Hence, the currents have been set completely independent from each other which shows the controller works as expected. The neutral current increases to an rms value of 88A. Note the neutral current may become much larger than any of the phase currents. Since one phase backfeeds, the average three-phase active power decreases, and the power becomes negative in certain intervals. It may seem odd in practice to charge on two phases and discharge on the third, but this is simply to show the generality employed in this control strategy. It also enables the converter to be used in grid-forming mode: If one phase voltage is detected to be low, it can feed back power to restore the voltage on this phase, and charge from the other two. However, this would require a voltage control loop which is not implemented in this simulation.

At 130ms, the phase charging at 63A is shifted 90°, meaning this phase now transfers reactive power rather than active power. The average reactive power is seen to settle at around $63\text{A}\cdot 230\text{V} = 14.5kW$. The average active power becomes negative with an average of around $(16\text{A} - 32\text{A})\cdot 230\text{V} = 3.7\text{kW}$, because one phase is discharging at 32A while another is charging at 16A. The neutral current, being the sum of the phase currents, increases again to around 110A rms. This would be too high in practice since the neutral wire is likely rated for the same currents as the phase wires. Thus, there are no theoretical limits on how the currents can be selected on a per-phase basis, but in reality, the sum of the currents must stay below 63A. Worst-case, if the phase currents are controlled to be in-phase, their rms values must not exceed $63\text{A}/3 = 21\text{A}$.

This simulation clearly shows the fact that single-phase charging is one case of heavily unbalanced three-phase power transfer. Therefore, with a four-legconverter and the 3D control method as explained in this section, it is possible to charge an EV from both single-phase and three-phase outlets using the same power converter and controller onboard the vehicle.

2.8 Conclusion

To enable fast-charging with AC, an onboard converter is required. This section discussed ways of implementing this converter in a cheap and versatile way. Since three-phase motor drives are inherently required, and since three-phase outlets are commonly available, it is a logical step to combine and integrate a three-phase charger with the motor drive.

It is possible to utilize the motor leakage reactance, but torque exertion must be considered. Tests were performed on a 17kW EV induction motor and a per-phase leakage inductance of $170\mu\text{H}$ was found, which is insufficient for a high power EV converter. However, this could be increased if the motor was modified slightly. The

torque was measured to be less than 5Nm at 60A, meaning vehicle restraining is required but relatively easy.

Instead of using the motor, discrete inductors can be used. A prototype inductor was constructed, which featured approximately 1mH of inductance at currents up to 63A rms. The inductor weighs 1.5kg and one manufacturer offers a similar design for $23 per inductor in relatively low volume. Implementing a high-power onboard converter with discrete inductors seems like a feasible approach.

Challenges exist for implementing the non-isolated charger, most notably, a high battery voltage is required. It is possible to use a DC-DC converter or increase battery voltage to overcome this.

By modulating the voltage across the inductor, four quadrant power flow is possible. Specifically, reverse active power flow is useful for V2G applications. Control, modulation and the converter circuit were described and simulated in Simulink. It was shown that charging is possible from unbalanced grids using symmetrical components theory. Furthermore, with a fourth leg added to the converter topology, the neutral current can be controlled as well, which enables grid-forming and three-phase vehicle-to-load applications.

More investigation is required into actual component choices and more practical experience should be acquired on the topics touched upon in this chapter. Based on this chapter, it is possible to implement a high-power converter in practice, which is a logical next-step.

Conclusively, it is reasonable to expect AC high-power charging to be available in future EVs.

CHAPTER 3

AC charging infrastructure

3.1 Introduction

This chapter discusses the infrastructure components required for fast-charging with AC. This includes the cord set connecting the EV supply equipment (EVSE) and the EV, and the EVSE itself. The goal is to allow amperages up to 63A, meaning charge rates of up to 43kW in EU and 52kW in US are achieved.

High-level communications between the EV and EVSE is an important feature, and a new physical-layer communication protocol defined in the upcoming IEC 61851-1 edition 3 will be described. The salient feature of this protocol is that it enables high-level communication in a relatively simple way using the pilot wire readily available in the charging cable. A test employing IP-based communication between the EVSE and EV will be shown.

A new 43kW three-phase AC-only EVSE is constructed based on components developed at the University of Delaware and DTU. The charging station was available in a single-phase version, and it was upgraded to support three-phase charging with utility-grade metering, AC/DC detecting (Type B) GFCI, pilot signal generation and a Linux system-on-module for high-level software capability. As was indicated in table 1.3, there are very few 43kW charging stations on the market, and even less are constructed as pure AC types. Hence, the charging station built in this project fills a gap in the otherwise highly competitive EVSE market. The charging station is tested by supplying three-phase 43kW to a Renault Zoe and 12kW single-phase to an AC Propulsion eBox.

3.2 Fast-charging AC cord sets

Two types of AC cord sets currently exist on the market, the Type 1 (J1772 cord set) and Type 2 (IEC 61851 cord set), see fig. 1.1. For the reasons spelled out in chapters 1 and 2, three-phase charging is preferred for fast-charging, and this requires the use of the Type 2 cord set. A few variations exist of the Type 2 cord
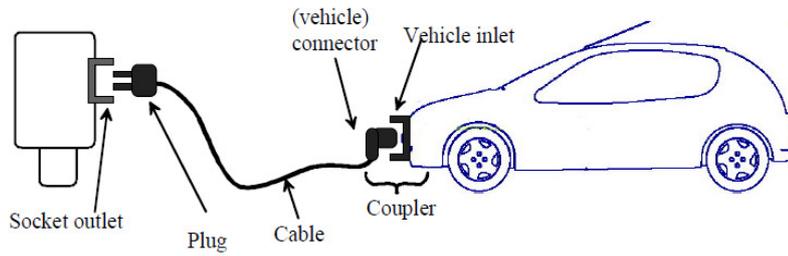
Figure 3.1: Cord set terminology according to IEC 61851-1 [5]
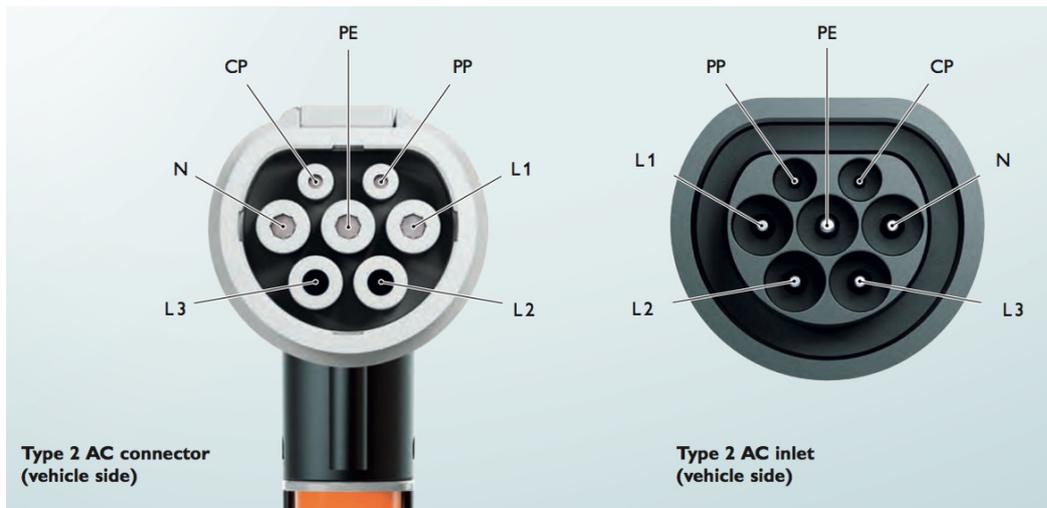
Figure 3.2: Type 2 connector and inlet pin configurations

set because both genders exist for both the EV and the EVSE side. Typically, using the terminology presented in fig. 3.1, the connector is female, the inlet is male, the plug is male and the outlet is female. It is also possible to have the cable fixed to the EVSE, in which case the outlet and the plug do not exist. This is always the case with the J1772 Type 1 cord set.

The male inlet and female connector are shown in fig. 3.2. Note the three phases are present along with the neutral, earth (PE), control pilot (CP) and proximity detection (PP). The proximity pin is connected through a specified resistance to earth inside the connector as shown in table 3.1, so it is not a wire run in the cable. An actual measurement on a 63A cable is shown in fig. 3.3.

Cord set rating	PP resistance
13A	1.5kΩ
20A	680Ω
32A	220Ω
63A	100Ω

Table 3.1: Plug present (PP) resistor value in the couplers

Figure 3.3: Measurement of the PP resistor. 100Ω corresponds to 63A rating.
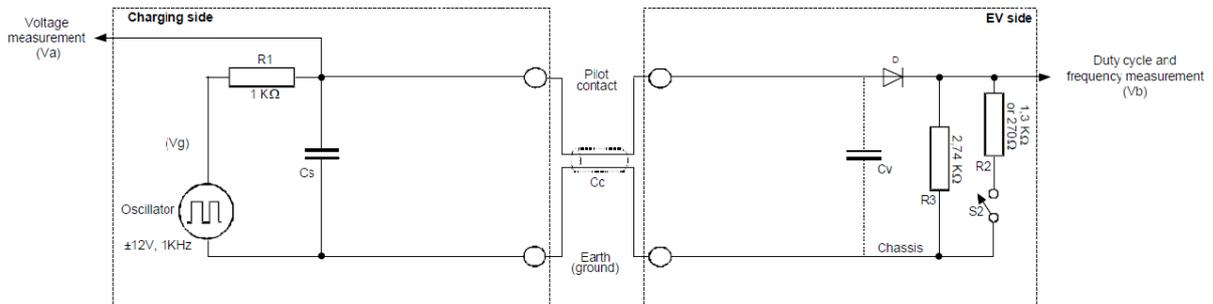
Figure 3.4: Typical pilot function schematic [5]

The control pilot, on the other hand, is a dedicated wire in the cable. Its typical function is to indicate to the vehicle how much current it is allowed to draw during charging. This is done through varying the duty cycle of a 1kHz pulse width modulated (PWM) signal. The EV indicates to the supply equipment if it is connected, and if it is ready to be charged. This is done through changing the amplitude of the PWM signal using a resistive voltage division.

A schematic of the CP circuit is seen in fig. 3.4. Note the 1kHz source at the supply side has a 1kΩ series resistance, meaning the positive peak voltage[1] on the pilot wire change depending on resistors R3, R2 and switch S2. The peak voltage can be measured by the EVSE at point *Va* on the drawing, and this measurement corresponds to one of four possible states:

- State A: 12V peak on pilot. No EV is connected, and the cable is deenergized.

- State B: S2 is off, 9V peak on pilot. EV is connected but not ready to charge.

- State C: S2 is on with R2=1.3kΩ, 6V peak on pilot. EV is connected, ready to charge.

---

[1] The negative voltage is always -12V due to the diode in the EV

PWM duty cycle d	Current draw allowed
$d < 3\%$	Not allowed
$3\% \leq d \leq 7\%$	Digital communication
$7\% \leq d < 8\%$	Not allowed
$8\% \leq d < 10\%$	6A
$10\% \leq d \leq 85\%$	$d \cdot 0.6$A
$85\% < d \leq 96\%$	$(d - 64) \cdot 2.5$A
$96\% < d \leq 97\%$	80A
$d > 97\%$	Not allowed

Table 3.2: Control Pilot (CP) duty cycle definitions [5]

- State D: S2 is on with R2=270Ω, 3V peak on pilot. EV is connected, ready to charge, EV requires ventilation during charging.

The duty cycle generated by the EVSE and the corresponding maximum current draw is shown in table 3.2. With typical CP functionality, the duty cycle will vary between 10% and 96%, which allows the current to vary between 6A and 80A, respectively. It should be noted that between 3% and 7%, nominally 5%, digital communication is allowed between the EVSE and EV. Hence, this duty cycle indicates to the EV that its current limitation should be set by other means than the PWM signal. This will be used in section 3.3 when high-level communication is implemented over the CP wire.

Each state is divided into two substates (A1, A2, B1, B2, C1, C2, D1, D2), depending on the presence of the PWM signal and thus the readiness of the EVSE. For instance, in state C1, the EV is ready to charge but the EVSE is not, so no PWM signal is generated. In state C2, a PWM is generated, meaning both sides are ready, and the vehicle is charged. Further detail on states and and state transitioning is found in IEC 61851-1 Annex A [5].

Evidently, if the CP signal does not mate the EVSE is in state A and the EV cannot charge. This is useful in case it is attempted to connect cables as extension cords. For example, if the female end of a charging cable is extended with the male end of another, the CP signal does not connect because the pins in the female connector are shorter than in the female outlet. Hence, the male plug only connects properly to a female outlet, not a female connector.

The Type 2 cord set is with edition 3 of IEC 61851-1 allowed to carry both AC and DC power over the same pins. Therefore, the pins normally used for the three phases and neutral for AC charging can also be used as positive and negative terminals for DC charging. For example, Tesla's Model S uses the same Type 2 connector for their 120kW DC and 22kW AC charging. This shows the versatility of the Type 2 connector, and that it is positioned to become the dominating charging cord set type in the future, in addition to the combo plug (which carries DC and is outside scope).

A 63A Type 2 AC cord set was procured in this project. The availability of 63A

(a) Type 2 63A AC plug. Note three phases, neutral, earth, CP and PP

(b) Other end of cable to be mounted in EVSE. The CP wire is also seen.

Figure 3.5: Procured charging cable

cord sets seems rather low, and larger cable manufacturers such as Mennekes and Phoenix Contact were not able to supply a 63A EV charging cord set at this point in time. However, it was possible to procure a 63A cord set from the Chinese manufacturer Dostar. This cable features 5 times 10mm^2 wires for the three phases, neutral and earth, and is priced at \$140 in single quantities. The procured cord set is displayed in fig. 3.5.

The cord set is detachable on most public Type 2 EVSEs, and the driver has to bring and plug in the cable. However, since a 63A cable is somewhat bulkier, it was preferred to fix it to the EVSE installation in this project. This corresponds to other fast-charging solutions, including DC fast-chargers, where the cable is always fixed to the supply equipment.

3.3 Communications

Fundamentally, with AC charging, the converter is located onboard the vehicle. In order to control charging, a communication link between a controlling entity (usually known as the backend) and the EV has to be established. This is especially desirable for V2G, intelligent charging, billing purposes, and for providing additional information to the driver.

For V2G, it is necessary to request the EV to charge or discharge at a certain power rate. Also, state of charge (SOC) and vehicle and location identification are required. Location is needed for V2G because in practice, permitting with local authority or distribution company is needed, so electronic confirmation is required prior to allowing reverse power flow. For intelligent charging, SOC is desired, because it will be possible to determine the charge rate based on actual needs. Vehicle identification (VIN or other unique number) is used for billing,

and this enables a "plug and charge" scheme, where the driver simply plugs in the vehicle to start charging, and billing is automatically taken care of using the communicated identification number. For simple charging sessions where billing, V2G and intelligent charging are not required, the CP PWM signal will be sufficient to control charging power.

It was concluded in the previous chapter that a three-phase grid-connected converter may be controlled on a per-phase basis and active and reactive power can be controlled to flow in both directions. With these possible set-points, high-level communication is required to request the desired behaviour from the onboard converter.

This section discusses the physical layer communication protocol defined in IEC 61851-1 Edition 3 Annex D (also known as CAN-CP). This is positioned to meet the needs for high-level communication with cheap and simple hardware. Application layer communication is not discussed here, but this is being standardized in e.g. IEC/ISO 15118-2 and Smart Energy Profile 2.0 [45].

3.3.1 CAN-CP communication

The communications protocol specified in Annex D is based on extending the functionality of the CP wire signalling in the charging cord sets to enable bidirectional half-duplex CAN communication, hence its name CAN-CP. This is also known as *extended pilot function*, compared to *typical pilot function* which uses PWM for unidirectional indications as described in previous section. Annex D is an informative section in IEC 61851-1 Edition 3 and is consequently not a strict requirement for EVs and EVSEs. In case CAN-CP is not supported in both the EV and EVSE, it falls back to using the typical pilot function.

Alternative means of physical layer communication are also being standardized (IEC/ISO 15118-3), most importantly power line communication (PLC). In PLC, a high-frequency communications carrier is injected into the power lines of the charging cable. Variations of this has also been seen where the PLC signal is injected into the CP wire. PLC enables IP communication and achieves data rates of up to 10Mbps using the Homeplug GreeenPHY standard.

However, PLC has a few drawbacks: Its usage is restricted in some regions, it is relatively complex[2] and difficult to isolate, because the high-frequency signals cross couple between wires, across breakers and distribution transformers [45]. This means the grid wires essentially become one shared multidrop communications network, and PLC modems are hence designed to overcome these challenges. This in turn increases complexity and eventually increases cost. Taking a step back, this was not needed in the first place: Communication between an EVSE and EV only requires a direct point-to-point link, which is easily implemented with dedicated communication wires in the cord set. Regrettably, there are no dedicated communication wires, but Annex D allows the use of the CP wire for single-wire CAN communication. Hence, the rather complex PLC technology can be avoided using Annex D, and instead, the CP wire is used for low-voltage wired digital point-to-point communication.

---

[2]Its theory is similar to that of cellular communication
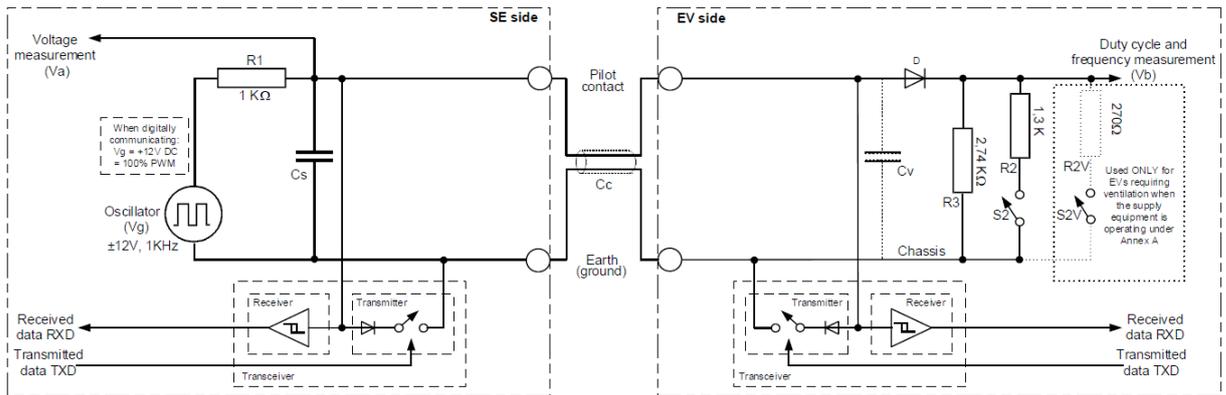
Figure 3.6: Extended pilot function schematic [5]

The additional transceiver circuits needed for Annex D functionality are shown in fig. 3.6. It is seen the generated PWM has a 100% duty cycle, that is, the voltage is held at 12V. Then, the transmitter grounds or ungrounds the pilot wire after R1 to transmit single bits. The receiving end detects this change and translates it into TTL level bits (denoted RXD and TXD). Although not shown on the drawing, the RXD and TXD signals can be passed directly to a regular CAN interface on a microcontroller for further processing.

CAN-CP achieves communication rates up to 500kbps. In case faster communication is needed, CAN-CP can be used as a means for establishing communication and associating the EV with the EVSE. Next, PLC or wireless can be used to increase communication speeds.

3.3.1.1 CAN-CP additional features

There are four feature sets in Annex D, three of which are optional:

1. Basic CAN (mandatory)
2. Advanced CAN using CANopen (optional)
3. Encapsulated IP (optional)
4. High speed (optional)

Basic CAN is a mandatory part of Annex D and serves to replace the functionality of the typical pilot function using PWM. Hence, Basic CAN transmits setpoints for current, ready messages and ventilation requirements. The transmission rate is fixed to 20kbps.

The advanced CAN feature adds CAN packets, including exchange of EVSE and EV identification numbers.

The encapsulated IP option (EIP) is used to transmit point-to-point protocol (PPP) packets inside CAN packets. In turn, PPP carries IP packets, enabling high-level communication using standard Internet protocols [11]. PPP is available in most operating systems including Linux.
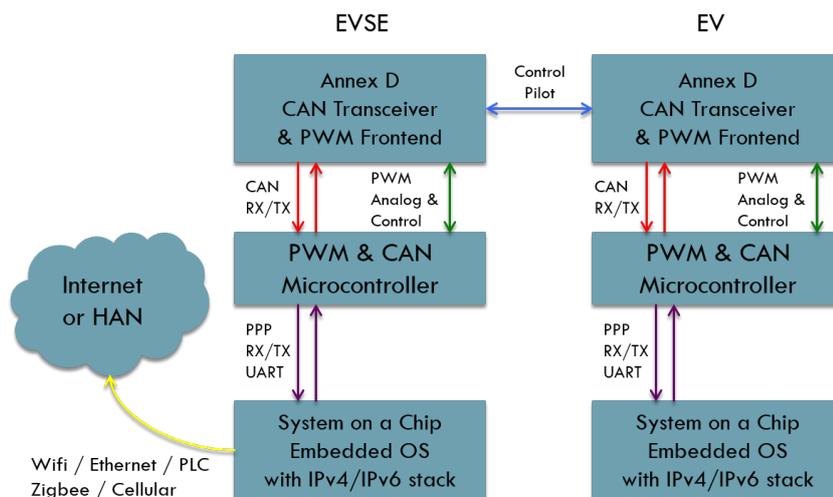
Figure 3.7: System level diagram of Annex D implementation

The high speed option achieves data rates up to 500kbps by surpassing the R1 1kΩ resistor and lowering the voltage on the line to allow quicker level shifts. This is ideally combined with EIP.

3.3.1.2 CAN-CP implementation

A system-level diagram of an example CAN-CP implementation is shown in fig. 3.7. Here, it is suggested that microcontrollers on both the EV and EVSE side are used to control the logic (i.e. the PWM signal) for the control pilot signal. The microcontrollers detect if CAN-CP communication is supported on both sides. If not, the controllers use the typical pilot function. If CAN-CP communication is supported, the microcontrollers serve to mirror all communication on a serial UART port directly to CAN packets. This means two devices connected to the serial ports, one in the EV and another in the EVSE, can communicate with each other. For these devices, the communication looks like any other UART interface. This can be used with e.g. Linux to establish a full IP communication between the EV and EVSE via a serial link.

3.3.2 Communication test

For this project, the microcontroller platform for establishing the CAN-CP communication was readily available, and the implementation of this is therefore not described. This platform was mounted in the project EVSE and the AC Propulsion eBox, meaning communication can be established between these two.

A Linux-based system-on-module was connected to the microcontroller's UART interface. Hence, the only required setup to enable IP communication is to run all IP traffic through the serial port. The procedure of doing this is explained in appendix G. The result is that the EV is fully connected to the Internet, which is revealed by pinging an Internet host such as *google.com* from the EV:

```
1 [ev:~]$ ping google.com
```

```
2 PING google.com (109.105.109.249): 56 data bytes
3 64 bytes from 109.105.109.249: icmp_seq=0 ttl=55 time=150.000 ms
4 64 bytes from 109.105.109.249: icmp_seq=1 ttl=55 time=130.000 ms
5 ^C--- google.com ping statistics ---
6 2 packets transmitted, 2 packets received, 0% packet loss
7 round-trip min/avg/max/stddev = 130.000/140.000/150.000/10.000 m
```

This test shows it is possible to have the EV connected to the Internet using a simple baseband communication through the control pilot wire in the cord set. This enables a wide range of possible applications, including smart charging based on e.g. Internet-accessible price signals, V2G management, vehicle call-for-service, firmware upgrades, and many more.

3.4 Construction of a three-phase 63A EVSE

A 63A three-phase EVSE was built during the project, see fig. 3.8. A similar EVSE has not been found anywhere on the EVSE market, and hence the constructed 63A three-phase EVSE is a novel product. A single-phase version of the EVSE was readily available, meaning some of the components were already developed, but they had to be upgraded to a three-phase counterpart. The EVSE also required software modifications, and these were applied in cooperation with University of Delaware. However, the software changes were few and will not be explained here. The EVSE consists of the following hardware components:

- Power distribution components, including DIN rail mountable terminal blocks for the three phases and neutral (3P+N). Earth clamps (colored green/yellow) are used to connect the PE wire of the cables to the enclosure. There are two sets of terminal blocks, one for the grid cable and one for the EV charging cable, which makes cable upgrade and installation relatively easy. The terminal blocks are all rated for 80A. The wiring is made with 10mm^2 cobber wires.

- A 12V power supply for low-voltage logic. This is rated for 100-240VAC, meaning it can be used for e.g. US split-phase 120V, US single phase 240V, and EU single-phase 230V. The single-phase voltage of a US 480V three-phase installation is 277V, which it therefore does not support at this point. It seems difficult to procure a cheap power supply rated for 100-280VAC as would be required to support all types of installations across the globe.

- A meter for billing, power and energy measurement purposes. An off-the-shelf utility-grade meter employing a Maxim 71M6543F three-phase metrology chip with a watthour accuracy of 0.5% [55]. Three current transformers (the coils with yellow labels on the pictures) are connected to the meter to measure currents, and the voltage is tapped on the DIN rail blocks. The meter has an RS485 communication interface.

- A GFCI for DC and AC fault-current detection. This was readily available for this project in a single-phase version. The single-phase version employs a KG Technologies *K220* two-pole relay rated for live switching at 120A/277VAC. For the three-phase version, two of these relays were used, enabling a four-pole switching of three phases and neutral. The ground fault is detected using

(a) Initial work on three-phase EVSE. It required modifications to all line power components, the power supply and metering, for three-phase capability.

(b) Work in progress.

(c) Finished three-phase EVSE.

(d) Temporary EVSE installation for testing. It draws 63A from a CEE outlet.

Figure 3.8: EVSE construction

a *CTSR 0.3* Fluxgate sensor coil from LEM which detects both DC and AC rms currents between -500mA and 500mA with frequencies up to 3.5kHz. All four wires are run through the ground fault coil, and the sum of the currents is hence measured by the surrounding coil. The fault current is set to 30mA like regular household GFCIs. An additional feature of this GFCI is its self-test ability, which makes a conventional "test" button unnecessary: A fifth (tiny) wire is run through the coil, and a small high-frequency current is applied. The current is measured on the output of the sensor, and by comparing the input with the measured output it is assured the GFCI sensor works as expected and can detect faults. The relay in the GFCI is also used as an over-current breaker, and the relay is only closed when the EVSE is outside of state A, that is, when an EV is connected to the EVSE.

- Hardware board for controlling the states and pilot PWM signal. This was readily available for the project. It also implements the hardware part of CAN-CP communication. When CAN-CP Encapsulated IP communication is established, it mirrors all communication on a UART interface directly to CAN packets on the CP wire.

- A $84 *TS7500* system-on-module running Linux and high-level communication software required for interfacing with the backend, as explained in section 3.3.2. The Linux module connects to the CAN-CP board via a UART, and can send IP packets using PPP to this interface.

These components are capable of handling any AC power up to 43kW in EU, 52kW in US without modification. Only the charging cable may require replacement in case the desired power rate changes, but the cable is easily replaced either during installation or at at later up- or downgrade.

The end price of the EVSE is difficult to assess without a larger scale production, but it is expected to be in the $2-3000 price range.

This price may be compared to other DC fast-charging solutions that are priced at least tenfold of this. Surely, it does not contain the same components as a DC fast-charger and it is thus not completely fair to compare prices: However, a CHAdeMO DC fast-charger and this AC EVSE charge at similar power rates so the comparison is in this context still quite relevant.

3.5 Charging station test

This section tests the constructed EVSE with the Renault Zoe and the AC Propulsion eBox, the latter with CAN-CP communication capabilities.

3.5.1 Renault Zoe charging session

A Renault Zoe was charged at 43kW, see fig. 3.9. This may likely be the first time this is done in Denmark from a dedicated high-power AC EVSE.

The battery capacity of the Zoe is 22kWh, and with 43kW charging, the battery fills in approximately half an hour. However, the charge rate drops after around
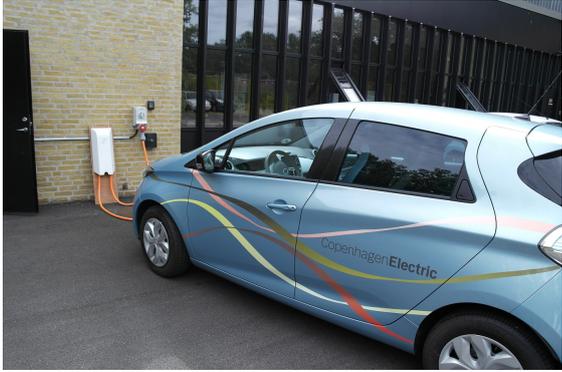
(a) Zoe parked and ready for charge in front of EVSE at DTU.
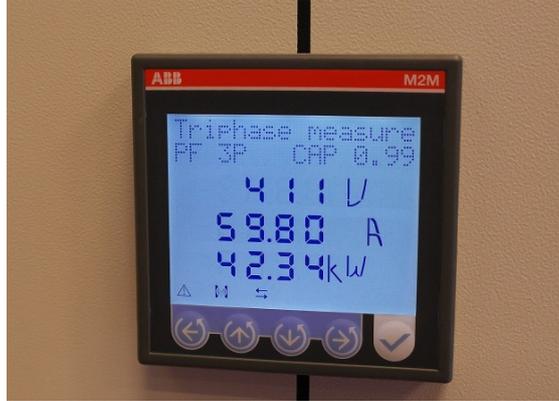
(b) Panel meter measures charge rate to 42.3kW with 0.99 power factor.

(c) Dashboard showing 66% SOC, 25 minutes remaining.

(d) Now showing 80% SOC, 20 minutes remaining: 14% charge in five minutes.

(e) 63A connector in Zoe inlet

(f) Display of first 43kW charging August 19th 2013.

Figure 3.9: Zoe charging session

80% SOC because it enters a constant voltage charging scheme. Hence, it takes 20 minutes to charge from 80% to 100%.

As shown in figs. 3.9c and 3.9d, the Zoe charged 14% in around five minutes, and it was in another session noted to charge 25% in nine minutes. This corresponds to around 2.8% SOC per minute. As with all EVs, its range depends on driving behaviour. Its NEDC rating is 210km, but it achieves more realistically around 150km of varied city driving in normal climates. So, assuming a driving range of 150km, the Zoe charges 150km · 2.8%/min = 4.2km/min.

Comparing this number with the average daily commuting distance in Denmark of 40km, a Zoe needs to be charged on average less than 10 minutes a day.

Renault Zoe pricing starts at 20700 €, plus a monthly fee for the battery.

A 43kW Zoe charging session using the project EVSE was presented at a seminar hosted by DTU and the Danish Electric Vehicle Alliance August 19th 2013 [17], see fig. 3.9f.

3.5.2 AC Propulsion eBox charging session

The AC Propulsion eBox is a 35kWh EV capable of delivering power back to the grid. It is used by the V2G programmes at University of Delaware [3] and DTU and features custom hardware and software developed by the universities. The vehicle supports 80A/19kW of charging and discharging from a single phase using the J1772 Type 1 inlet. To support the Type 2 cord set mounted on the EVSE, the inlet was changed to a 63A Type 2 procured from Dostar, see fig. 3.10. An additional 63A charging cable was also bought in order to connect the eBox with other EVSEs featuring Type 2 outlets.

Due to a missing software upgrade in the onboard computer, the EV did not charge at the full 63A, but was limited to 50A max. However, this is fine for testing the 63A cord set. Charging at 11.5kW is shown in fig. 3.10e and discharging at 9.5kW is shown in fig. 3.10f.

3.5.3 Test conclusion

The two charging sessions presented show fast-charging with AC is possible, and it should be noted that the EVSE is small, light and relatively inexpensive while being capable of providing as much power as many DC fast-chargers. Hence, these tests support several key arguments for AC fast-charging as presented in chapter 1.

3.6 Load management

An issue often encountered with both DC and AC fast-charging is the ampacity limitations in the grid supply. When charging many EVs at one location, e.g. at a parking lot or public space, the vehicles will in many cases be able to draw more current than can be supplied. This issue may be severe for AC EVSEs, because more AC EVSEs with high ampacities will be placed at one site. For example,

(a) Upgrading eBox inlet to 63A

(b) Type 2 connector fits new eBox inlet

(c) eBox charging from 63A EVSE

(d) Dashboard with charge/discharge control
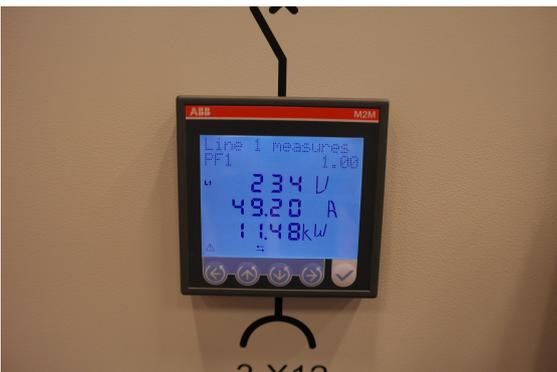
(e) Charge at 49A, 11.5kW

(f) Discharge at 40A, 9.5kW

Figure 3.10: AC Propulsion eBox charging session
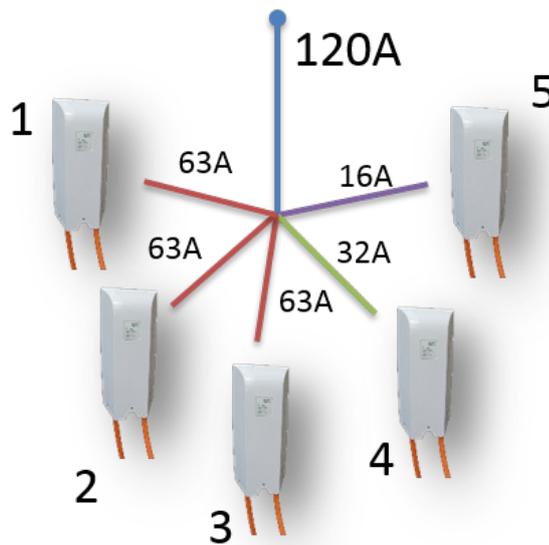
Figure 3.11: Five EVSEs star-connected to the grid with limited ampacity

take the 43kW EVSE built in this project, and say that ten of these are to be installed on a parking lot: It would require a power supply of 430kW and 630A main feeder rating to supply the maximum amount of power, making this solution quite impractical. Instead, we are interested in sharing the available power between the EVSEs, which makes sense, because not all EVSEs are used at the same time anyway. So, an algorithm has to be developed that utilizes the available current in the best way possible.

This section will present a simple algorithm for managing multiple EVSEs connected to the grid with a specific maximum current rating. The algorithm will disregard SOC or any kind of range-need prediction that may affect the priority of the charging. Furthermore, there will be no need to access a centralized server, that is, the EVSEs negotiate on-site in order to share available current. This means no third-party EV operator is needed, and neither do the EVSEs have to be connected to the Internet, only to each other. The algorithm does not require EV to EVSE high-level communication, since it is assumed the CP PWM signal changes an EVs current draw[3]. Overall, the goal is to make this algorithm practical and implementable today. However, an actual implementation is yet to be made.

It will initially be assumed that EVSEs are connected in a star topology. An example of such scenario is shown in fig. 3.11, where five EVSEs are connected to a 120A feeder. EVSE 1-3 are 63A rated, EVSE 4 is 32A rated and EVSE 5 is 16A rated. Clearly, the combined charging power of the EVSEs exceeds the feeder ampacity.

Let us start by explaining the overall idea of the algorithm, and a more detailed explanation follows afterwards. Fundamentally, the EVSEs are not allowed to charge with higher power than the grid can supply. If no communication takes place be-

---

[3]However, EV to EVSE communication is desired to tell the EVSE the nominal EV charge rate. Otherwise, the charge rate has to be "guessed" by using the PWM signal to allow the EV to charge slightly faster than its rated ampacity.

tween the EVSEs, the best we can do is to either hope they never charge too much at once, or permanently limit the EVSEs so that the combined power never exceeds the grid ampacity. Neither of these solutions are elegant. Therefore, the algorithm works by initially assigning a "default" ampacity to each of the EVSEs, where the combined charging power at the default charge rate will not exceed the grid ampacity. Now, the EVSEs that are partially utilized or not utilized at all are allowed to lend ampacity to other EVSEs that need it. An EVSE can only lend out its "default" ampacity, which ensures the grid ampacity is never exceeded. An EVSE can at any point in time reacquire its default ampacity and charge at this rate. Hence, the algorithm is fair because it only allows an EVSE to increase its charge rate when another EVSE is not fully utilizing its default ampacity anyway.

For a more detailed explanation, current values have to be defined:

- I_{car} is the current an EV draws.
- I_{set} is the current an EV is allowed to draw. This is set by the duty cycle of the PWM signal or by high-level EVSE to EV communication (e.g. using CAN-CP).
- I_{EVSE} is the maximum current an EVSE can provide. This is given by the lesser of the EVSE current rating and the current rating of the grid supply cables to the EVSE (not the main supply).
- I_{max} is the maximum current available from the grid in the star topology, e.g. 120A in fig. 3.11.
- I_{def} is the default current available from an EVSE.

Based on these definitions, a few rules can be set up: I_{car} must be lower or equal to I_{set}, and I_{set} varies between 0 and I_{EVSE}. I_{max} will typically be somewhat larger than I_{EVSE}, but if not, I_{EVSE} is set to I_{max}.

The default current I_{def} determines the allowed charge current when all EVSEs are in use. Furthermore, the default current is used whenever communication between EVSEs is faulty. The sum of all EVSE default currents must equal I_{max}. One possible definition of I_{def} is:

$$I_{def,n} = \frac{I_{EVSE,n}}{\sum\limits_{all\ n} I_{EVSE,n}} I_{max} \tag{3.1}$$

where n means the n'th EVSE. Hence, for the five EVSEs in fig. 3.11, $\sum\limits_{all\ n} I_{EVSE,n} = 3 \cdot 63 + 32 + 16 = 237$, and the I_{def} values for the EVSEs are:

$$I_{def,1,2,3} = \frac{63}{237} \cdot 120 = 32 \tag{3.2}$$

$$I_{def,4} = \frac{32}{237} \cdot 120 = 16 \tag{3.3}$$

$$I_{def,5} = \frac{16}{237} \cdot 120 = 8 \tag{3.4}$$

And, $3 \cdot 32 + 16 + 8 = 120$ as expected. In practice, one EVSE is temporarily selected as master, which will calculate the I_{def} values for all other EVSEs. This master will be initialized with the I_{max} value, and other EVSEs will send its I_{EVSE} and receive a corresponding I_{def} value. For every EVSE joining or leaving the network, new I_{def} values will be sent out to all EVSEs. In case of a malfunctioning master EVSE, another master EVSE is dynamically reselected given this knows the I_{max} value. Hence, I_{max} should be sent out along with I_{def} in case another EVSE will be selected as master at a later point in time.

Initially, $I_{set} = I_{def}$, but this should obviously change in order to redistribute available current among the EVSEs. So, in case an EVSE needs to provide more current than I_{def}, a four-way handshake will take place:

1. The EVSE needing more ampacity asks all other EVSEs for a specific amount of current. The current request is denoted I_{req} and is always equal to or less than $I_{EVSE} - I_{def}$, because an EVSE will never need more current than it can supply.

2. Other EVSEs offer the current they can spare.

3. The requesting EVSE chooses one or more offers, and communicates the exact amount of current needed to each of the offering EVSEs.

4. The offering EVSE accepts or declines the deal.

These four steps constitute the core of the algorithm. The idea of step three and four is to enable an EVSE to offer ampacity to many EVSEs, but it is ensured only one other EVSE is assigned this additional ampacity. After the negotiation is settled, the offering EVSE decreases its I_{set} with I_{req}, and the requesting EVSE increases its I_{set} by I_{req}.

In case an EV plugs into an EVSE that has offered some of its ampacity to another EVSE, it can immediately reacquire its ampacity so its I_{set} reaches I_{def}. After this, if needed, it has to negotiate with neighbouring EVSEs to deliver more current than I_{def}, as described above.

After an EV is charged, and the EVSE does not need the ampacity it has previously requested, it hands the ampacity back to the original EVSE. In this way, ampacity always belongs to a specific EVSE but is lent to neighbouring EVSEs when it is not needed. Furthermore, it is guaranteed that an EVSE is capable of charging at no less than the I_{def} setpoint.

During communication faults, an EVSE defaults to its I_{def} value after a predefined timeout: The timeout is short (e.g. 5 minutes) for EVSEs that offers ampacity to other EVSEs, i.e. $I_{set} < I_{def}$. The timeout is longer (e.g. 15 minutes) for EVSEs that use another EVSE's ampacity, i.e. $I_{set} > I_{def}$. Hence, if communication fails, all EVSEs will eventually be able to charge at I_{def}. A "keep-alive" signal must be sent often (e.g. every 2 minutes) to reconfirm the ampacity negotiation and avoid the timeouts.

As shown in chapter 2, an EV may be able to control the charge rate on a per-phase basis, and there will often be a mix of single- and three-phase charging EVs. Hence, all currents must be dealt with per-phase. The algorithm still applies with per-phase values.

Without high-level communication, the only way of knowing if an EV wants to charge at a higher rate than I_{set} is to use the PWM signal and leave a small overhead between the EV's actual charge rate I_{car} and I_{set}, e.g. 5A. In case the difference between I_{car} and I_{set} is less than 5A, an EVSE requests additional ampacity in blocks of 5A. This could be avoided if the EV informed the EVSE of its nominal charge rate through e.g. CAN-CP communication.

It is possible to allow prioritized charging, i.e. an ampacity request from a higher-priority EVSE should be served even though ampacity has already been assigned to another, lower-priority EVSE. The priority is provided along with the ampacity request in step 1 in the handshaking process, and the offering EVSEs must remember the priority of the ampacities it has assigned to other EVSEs, and if it is lower, it must include this in the ampacity offer in step 2.

Specifically, if EVSEs at a site are assigned with increasing priorities, EVs are charged sequentially with the highest priority first.

The communication between EVSEs will in practice likely be IP-based, meaning a communications network has to be established. Since EVSEs connected to the same grid supply are usually placed close to each other, it is possible to use wireless communication. For instance, Wi-Fi has an *ad-hoc* mode in which no access point is required for communication. This is also the case with Wi-Fi Direct, Zigbee and others. For discovering neighbouring EVSEs, the mDNS protocol can be used [7].

In case EVSEs are connected in a more advanced tree topology, it is possible to subdivide the tree into several smaller star topologies and the algorithm still applies.

This concludes the description of the proposed load management algorithm. With this technique, it is possible to connect multiple EVSEs at one site where the grid does not support charging from all EVSEs simultaneously. This is a key enabling technology in installing an increasing amount of AC high-power EVSEs in the field.

3.7   Conclusion

This chapter explored AC fast-charging infrastructure components rated for 63A. It was found that nearly no 63A EVSEs or 63A cord sets exist on the market today. Hence, a new and one-of-its-kind EVSE was built to support charging at 63A.

The company Dostar was found to manufacture 63A cord sets, which was mounted on the constructed EVSE.

The basics of the typical and extended pilot signal were explored in the Type 2 AC cord set. The extended pilot signal features high-level communication using CAN-packets on the pilot line, known as CAN-CP, which is being standardized in IEC 61851 Ed. 3 Annex D. It was shown how e.g. Linux allows IP communication through any serial line, and the EV was in this way connected to the Internet.

With the constructed AC EVSE, a Renault Zoe was charged at 43kW. This corresponds to a charge time from 0% to 80% SOC of around 29 minutes, and the EV gets 4.2km of range per minute at this charge rate. The EVSE in this project is estimated to be priced around $2-3000 for end sales excl. VAT.

A load management algorithm was presented that effectively shares available current at a site with limited grid supply. The algorithm requires communication between the EVSEs but no third-party operator nor Internet connection are required, making this solution simple and practical.

Overall, this chapter shows AC fast-charging at 63A is indeed practically realizable.

Conclusion

This project explored electric vehicle AC fast-charging using a systems engineering approach, encompassing a range of engineering disciplines. In chapter 1 fourteen arguments for the use of AC fast-charging were spelled out. The chapter concluded that with AC fast-charging, EV rollout costs are lowered significantly. The result is that EV fast-charging will be available at many locations, perhaps even in EV drivers' homes, and the range anxiety issue will be reduced. Furthermore, V2G and ancillary grid services rely on AC onboard converters, and these technologies can considerably aid to the business case for EVs.

Chapter 2 investigated a three-phase charger topology based on the traction components used to drive the three-phase motor. These components have the additional benefit that they are inherently designed to allow reverse power flow, which is useful for V2G and ancillary services applications. Challenges in using this converter topology were presented. The inductance required in the charger topology was suggested to be implemented by either utilizing the leakage inductance in the motor or using a discrete inductor. The latter solution seemed relatively straight forward and poses little additional cost (<$70) and weight (<5kg) to the vehicle. Simulations were made using the charger topology and its inductance, and it was shown how three-phase charging can be controlled in balanced and unbalanced grids. Furthermore, a four-leg converter was presented which supports unbalanced per-phase current control and allows three-phase V2L and grid-forming operation.

Chapter 3 presented 63A infrastructure equipment. A 63A cord set was procured and mounted in a 63A EVSE constructed during the project. A Renault Zoe was charged at 43kW using three phases, and an AC Propulsion eBox was charged at 12kW using a single phase. High-level CAN-CP communication was made possible by the upcoming IEC 61851-1 Annex D standard, and the EV was connected to the Internet. This allows for a wide range of applications including intelligent charging/discharging of the EV, and additional EV service capabilities. Finally, to support multiple AC fast-charging stations at a location with limited grid supply, a practical load management algorithm was presented.

Based on the conclusions expressed in this project, four EV policy recommendations can be stated:

1. In future infrastructure roll-outs, AC fast-charging stations should be preferred over AC slow-charging stations. This implies installing a charging sta-

tion with the maximum possible rated amperage, limited only by grid supply constraints.

2. DC charging stations installed to service DC fast-charging EVs must also provide an AC connector rated to its maximum possible value.

3. To increase renewable generation in the electric grid, EVs that provide bidirectional power flow and thus enable V2G and ancillary services, should be fiscally incentivized.

4. Super-fast AC charging should be investigated to explore AC charging power levels beyond 50kW. Standardizing charging cables for this purpose is one first step.

Overall, the project shows that fast-charging using AC is feasible and practically realizable. If the recommendations presented in this project are used in future EVs and infrastructure, it is expected that fast-charging will be easily accessible, range anxiety is minimized and infrastructure costs are considerably reduced.

Future Work

Future work to be undertaken may involve:

- Further exploring converter challenges, e.g. estimate the efficiency, THD, and DC injection and leakage behavior of an existing EV charger.
- Constructing an EV high-power bidirectional charger. This may be using a four-leg converter approach to enable three-phase V2L and grid-forming mode. Super-fast AC charging could be investigated with the same charger.
- Pushing for a larger scale 63A EVSE production and roll-out.
- Implementing the load management algorithm described.

Bibliography

[1] Texas Instruments EV charger website. URL http://www.ti.com/solution/ev_hev_charger_level_1_2.

[2] Think City EV on Wikipedia. URL http://en.wikipedia.org/wiki/Think_City.

[3] V2G website. URL http://www.udel.edu/V2G/.

[4] CHAdeMO website. URL http://www.chademo.com/wp/.

[5] IEC 61851-1 Edition 3 CD2.

[6] Lithium-air battery. URL http://en.wikipedia.org/wiki/Lithium%E2%80%93air_battery.

[7] Multicast DNS. URL http://www.multicastdns.org/.

[8] Quick-Tip: Linux NAT in Four Steps using iptables. URL http://www.revsys.com/writings/quicktips/nat.html.

[9] Nissan Quickcharge Website. URL http://nissanqc.com/.

[10] Panasonic NCR-18650A datasheet. URL https://industrial.panasonic.com/www-data/pdf2/ACI4000/ACI4000CE25.pdf.

[11] PPP IETF Standard. URL http://www.ietf.org/rfc/rfc1661.txt.

[12] PyVISA package. URL http://pyvisa.readthedocs.org/en/latest/.

[13] SMA Transformerless three-phase inverters. URL http://www.sma-america.com/en_US/products/grid-tied-inverters/sunny-tripower/sunny-tripower-12000tl-us-15000tl-us-20000tl-us-24000tl-us.html.

[14] Tesla battery swap. URL http://www.teslamotors.com/batteryswap.

[15] DC Injection into Low Voltage AC Networks, 2005. URL http://webarchive.nationalarchives.gov.uk/20100919181607/http://www.ensg.gov.uk/assets/dgcg0000200.pdf.

[16] Redegørelse om rammebetingelser for opstilling af ladesta-
     tioner til elbiler, January 2011. URL http://www.
     ens.dk/sites/ens.dk/files/info/nyheder/nyhedsarkiv/
     arbejdsgruppe-giver-bud-paa-udrulningsplan-ladestandere-elbiler/
     Redeg_ladestandere_elbiler_jan2011_final.pdf.

[17] Gå-hjem-møde hos DTU Elektro om elbilsprogram, August 2013. URL http:
     //www.danskelbilalliance.dk/Nyhed/2013/13_08_27B.aspx.

[18] International Energy Agency. Global EV Outlook, April 2013.

[19] Joel Anderson and F.Z. Peng. Four quasi-z-source inverters. 2008.

[20] Baocheng, Xiaoqiang, Herong, Qiang, and Weiyang. Real-time dc injection
     measurement technique for transformerless pv systems. *2nd IEEE Interna-
     tional Symposium on Power Electronics for Distributed Generation Systems*,
     pages 980–983, 2010.

[21] Blewitt, Atkinson, Kelly, and Lakin. Approach to low-cost prevention of dc
     injection in transformerless grid connected inverters. *IET Power Electronics*,
     3:111–119, 2010.

[22] Bloomberg. In Ghosn We Trust Tested as Nissan Electric Push
     Falters. URL http://www.bloomberg.com/news/2013-03-20/
     in-ghosn-we-trust-tested-as-nissan-electric-push-falters.html.

[23] Borsen. Better Place Går Konkurs, 2013. URL http://borsen.dk/nyheder/
     virksomheder/artikel/1/258507/better_place_gaar_konkurs.html.

[24] Brusa. Brusa Battery EVB1-350-40-HP datasheet. URL http:
     //www.brusa.biz/fileadmin/Diverses/Download/Datenblaetter/BRUSA_
     DB_EN_EVB1-HP.pdf.

[25] Cory Budischak, DeAnna Sewell, Heather Thomson, Leon Mach, Dana E.
     Veron, and Willett Kempton. Cost-minimized combinations of wind power,
     solar power and electrochemical storage, powering the grid up to 99.9 *Journal
     of Power Sources*, 225:60–74, 2013.

[26] DoE. Greenhouse Gas Emissions for Electric and Plug-In Hybrid Electric
     Vehicles, 2013. URL http://www.fueleconomy.gov/feg/Find.do?zipCode=
     19716&year=2012&vehicleId=32154&action=bt3.

[27] DONG. Avedøre Power Station, 2013. URL http://www.dongenergy.com/
     en/business%20activities/generation/activities/central_power_
     stations/pages/avedoere_power_station.aspx.

[28] DTU. The Danish National Travel Survey, October 2012. URL http://www.
     modelcenter.transport.dtu.dk/english/tu.aspx.

[29] Nicolas H. du Penhoat. Renault ZOE: Quite simply revolutionary and
     yet a reality, 2013. URL http://blog.renault.com/en/2012/03/06/
     renault-zoe-quite-simply-revolutionary-and-yet-a-reality/.

[30] Energinet.DK. Download of market data. URL http://energinet.dk/EN/
El/Engrosmarked/Udtraek-af-markedsdata/Sider/default.aspx.

[31] Energinet.DK. Elproduktion fra vedvarende energikilder,
5 2013. URL http://energinet.dk/DA/KLIMA-OG-MILJOE/
Elsektorens-miljoepaavirkninger/Elproduktion-i-Danmark/Sider/
Produktion-af-vedvarende-energi.aspx.

[32] Energinet.DK. Introduktion til systemydelser, 2013. URL https:
//www.energinet.dk/SiteCollectionDocuments/Danske%20dokumenter/
El/43532-13_v1_Introduktion%20til%20systemydelser.PDF.

[33] Erikson and Maksimovic. *Fundamentals of Power Electronics*. KAP, 2004.

[34] Brus et.al. Fremtidens elpristavle. Technical report, EA Energianalyse, 2013.
URL http://www.ens.dk/sites/ens.dk/files/undergrund-forsyning/2_
-_elpristavlen_hovedrapport_final_ver2.pdf.

[35] Fitzgerald, Kingsley, and Umans. *Electric Machinery*. McGraw-Hill, 2003.

[36] Glover, Sarma, and Overbye. *Power System Analysis and Design*. Cengage
Learning, 2008.

[37] Feng Guo, Lixing Fu, Chien-Hui Lin, Cong Li, Woongchul Choi, and Jin Wang.
Development of an 85 kw bidirectional quasi-z-source inverter with dc-link feed
forward compensation for electric vehicle applications. 2013.

[38] Xiao-Qiang Guo, Wei-Yang Wu, and He-Rong Gu. Phase locked loop and
synchronization methods for gridinterfaced converters: a review. *Electrical
Review*, 87:182–187, 2011.

[39] Saeid Haghbin. *Integrated Motor Drive and Battery Chargers for Electric or
Plug-in Hybrid Electric Vehicles*. PhD thesis, Chalmers University of Technol-
ogy, 2013.

[40] Saeid Haghbin, Sonja Lundmark, Mats Alaküla, and Ola Carlson. Grid-
connected integrated battery chargers in vehicle applications: Review and new
solution. *IEEE Transactions on Industrial Electronics*, 60:459–473, 2013.

[41] Michael Hidrue, George Parsons, Willett Kempton, and Meryl Gardner. Will-
ingness to pay for electric vehicles and their attributes. *Resource and Energy
Economics*, 33:686–705, 2011.

[42] IEA. *Hybrid and Electric Vehicles - The Electric Drive Plugs In*. International
Energy Agency, 2011.

[43] David Infield, Peter Onions, Anton Simmons, and Gordon Smith. Power qual-
ity from multiple grid-connected single-phase inverters. *IEEE TRANSAC-
TIONS ON POWER DELIVERY*, 19, no. 4:1983–1989, 2004.

[44] Joachim Skov Johansen. Design and implementation of an electric vehicle
charging station. Technical report, 2011.

[45] Joachim Skov Johansen. Electric vehicle communication methods. Technical
report, Technical University of Denmark, 2011.

[46] Oskar Josefsson. *Energy Efficiency Comparison Between Two-level and Multilevel Inverters for Electric Vehicle Applications*. PhD thesis, Chalmers University of Technology, 2013.

[47] Antonia Juhasz. Why the war in Iraq was fought for Big Oil, April 2013. URL http://edition.cnn.com/2013/03/19/opinion/iraq-war-oil-juhasz.

[48] Willett Kempton and Jasna Tomic. Vehicle-to-grid power fundamentals: Calculating capacity and net revenue. *Journal of Power Sources*, 144:268–279, 2005.

[49] Hyosung Kim and Hirofumi Akagi. The instantaneous power theory on the rotating p-q-r reference frames. *International Conference on Power Electronics and Drive Systems*, pages 422–427, 1999.

[50] Hyosung Kim, Frede Blaabjerg, Birgitte Bak-Jensen, and Jaeho Choi. Instantaneous power compensation in three-phase systems by using p-q-r theory. *IEEE Transactions on Power Electronics*, Vol 17 no 5:701–710, 2002.

[51] Clifford Krauss and Ashley Parker. Romney Energy Plan Would Expand Oil Drilling on U.S. Land and Offshore. URL http://www.nytimes.com/2012/08/23/us/politics/romney-tries-to-refocus-campaign-on-economy-and-obama-turns-to-education.html?_r=0.

[52] Philip T. Krein. Electrostatic discharge issues in electric vehicles. pages 1245–1250, 1995.

[53] Liu, Abu-Rub, Ge, and Peng. Analysis of space vector modulations for three-phase z-source / quasi-z-source inverter. *IEEE*, pages 5268–5273, 2012.

[54] Eric Loveday. WSJ Nissan Leaf profitable by year three battery cost closer to 18,000, May 2010. URL http://green.autoblog.com/2010/05/15/nissan-leaf-profitable-by-year-three-battery-cost-closer-to-18/.

[55] Maxim. Energy Meter ICs. URL http://www.maximintegrated.com/datasheet/index.mvp/id/7211.

[56] Mohan, Undeland, and Robbins. *Power Electronics - Converters, Applications and Design*. John Wiley & Sons, Inc., 2003.

[57] Mohd, Ortjohann, Hamsic, Sinsukthavorn, Lingemann, Schmelter, and Morton. Control strategy and space vector modulation for three-leg four-wire voltage source inverters under unbalanced load conditions. *IET Power Electronics*, Vol 3, iss 3:323–333, 2009.

[58] Gary Mulcahy and John Santini. Considerations on ground fault protection for electric vehicles, 2012. URL http://www.tdipower.com/PDF/white_paper/Ground-Fault-White-Paper.pdf.

[59] Elon Musk. The Secret Tesla Motors Master Plan (just between you and me), 2006. URL http://www.teslamotors.com/blog/secret-tesla-motors-master-plan-just-between-you-and-me.

[60] Nathaniel S. Pearre, Willett Kempton, Randall L. Guensler, and Vetro V. Elango. Electric vehicles: How much range is required for a day's driving? *Transportation Reseach*, Part C 19:1171–1184, 2011.

[61] Pena, Clare, and Asher. Doubly fed induction generator using back-to-back pwm converters and its application to variablespeed wind-energy generation. *IEEE Electrical Power Electronic Applications*, 143, no 3:231–241, 1996.

[62] Skatteministeriet. Example of registration tax calculation. URL http://www.skm.dk/skatteomraadet/talogstatistik/afgiftsberegning/2287.html.

[63] Terry Tamminen. *Lives per gallon: the true cost of our oil addiction*. Island Press, 2009.

[64] Tesla. Roadster Efficiency and Range, 2008. URL http://www.teslamotors.com/blog/roadster-efficiency-and-range.

[65] Mehmet Ucar and Engin Ozdemir. Control of a 3-phase 4-leg active power filter under non-ideal mains voltage condition. *Electric Power Systems Research*, 78: 58–73, 2008.

[66] Vechiu, Curea, Camblong, Ceballos, and Villate. Digital control of a three-phase four-leg inverter under unbalanced voltage conditions.

[67] Vechiu, Camblong, Tapia, Dakyo, and Curea. Control of four leg inverter for hybrid power system applications with unbalanced load. *Energy Conversion and Management*, 48:2119–2128, 2007.

[68] Matthew Wald. In Two-Way Charging, Electric Cars Begin to Earn Money From the Grid, April 2013. URL http://www.nytimes.com/2013/04/26/business/energy-environment/electric-vehicles-begin-to-earn-money-from-the-grid.html?_r=0.

[69] Wang, Liu, Hicks-Garner, Sherman, Soukiazian, Verbrugge, Tataria, Musser, and Finamore. Cycle-life model for graphite-lifepo4 cells. *Journal of Power Sources*, 196:3942–3948, 2011.

[70] WCA. Coal and Electricity Generation, 2009. URL http://www.worldcoal.org/bin/pdf/original_pdf_file/coal_matters_3_-_coal_and_electricity_generation(16_05_2012).pdf.

[71] Bin Wu. *High-power Converters and AC Drives*. Wiley Interscience, 2006.

[72] Richard Zhang, Himamshu Prasad, Dushan Boroyevich, and Fred C. Lee. Three-dimensional space vector modulation for four-leg voltage-source converters. *IEEE Transactions on Power Electronics*, 17, no. 3:314–326, 2002.

APPENDIX A

Inductor measurements

setV	setF	V	A	P	S	Q	Inductance
1.5	50	1.51	4.53	2.09	6.86	6.54	**1.11E-03**
1.6	50	1.64	4.81	2.50	7.88	7.47	**1.14E-03**
1.7	50	1.68	5.11	2.71	8.58	8.15	**1.10E-03**
1.8	50	1.78	5.33	3.13	9.66	9.14	**1.11E-03**
1.9	50	1.90	5.75	3.55	10.94	10.35	**1.11E-03**
2	50	2.03	5.93	4.17	12.03	11.28	**1.16E-03**
2.1	50	2.11	6.20	4.38	13.28	12.54	**1.13E-03**
2.2	50	2.19	6.53	4.38	14.30	13.61	**1.12E-03**
2.3	50	2.30	6.78	5.42	15.60	14.63	**1.15E-03**
2.4	50	2.39	7.02	5.63	16.76	15.78	**1.15E-03**
2.5	50	2.44	7.26	5.63	17.70	16.78	**1.13E-03**
2.6	50	2.57	7.63	6.68	19.59	18.42	**1.14E-03**
2.7	50	2.63	7.78	6.88	20.45	19.26	**1.14E-03**
2.8	50	2.73	8.15	7.51	22.24	20.94	**1.13E-03**
2.9	50	2.82	8.38	7.72	23.60	22.30	**1.13E-03**
3	50	2.90	8.71	7.93	25.23	23.96	**1.12E-03**
3.1	50	3.05	9.11	9.60	27.77	26.05	**1.13E-03**
3.2	50	3.16	9.43	10.43	29.83	27.95	**1.14E-03**
3.5	50	3.47	10.46	12.73	36.33	34.03	**1.13E-03**
3.6	50	3.55	10.65	13.35	37.78	35.35	**1.13E-03**
3.7	50	3.61	10.92	13.77	39.38	36.89	**1.12E-03**
3.8	50	3.75	11.29	15.02	42.30	39.54	**1.13E-03**
3.9	50	3.85	11.66	16.48	45.11	41.99	**1.13E-03**
4	50	3.97	12.01	16.90	47.65	44.55	**1.12E-03**
4.1	50	4.05	12.21	17.73	49.42	46.44	**1.12E-03**
4.2	50	4.15	12.58	18.36	52.21	48.88	**1.12E-03**
4.3	50	4.33	13.09	20.65	56.62	52.72	**1.13E-03**
4.4	50	4.42	13.41	21.49	59.22	55.18	**1.12E-03**
4.5	50	4.42	13.48	21.49	59.58	55.57	**1.12E-03**
4.8	50	4.81	14.74	25.87	70.90	66.01	**1.12E-03**
4.7	50	4.76	14.62	25.87	69.66	64.68	**1.12E-03**
4.8	50	4.79	14.74	25.66	70.64	65.81	**1.11E-03**
4.9	50	4.82	14.78	25.45	72.06	67.10	**1.10E-03**
5	50	4.96	15.26	27.54	75.65	70.46	**1.11E-03**
5.1	50	5.06	15.58	29.21	78.83	73.22	**1.11E-03**
5.2	50	5.15	15.89	29.83	81.81	76.95	**1.10E-03**
5.3	50	5.29	16.41	32.13	86.83	80.66	**1.10E-03**
5.4	50	5.37	16.69	32.96	89.66	83.38	**1.10E-03**
5.5	50	5.43	16.87	34.21	91.51	84.87	**1.10E-03**
5.6	50	5.54	17.27	36.09	95.68	88.62	**1.10E-03**
5.7	50	5.66	17.68	37.13	99.98	92.83	**1.10E-03**
5.8	50	5.74	17.94	38.80	103.00	95.41	**1.10E-03**
5.9	50	5.86	18.43	40.47	108.02	100.16	**1.09E-03**
6	50	5.92	18.62	41.10	110.28	102.33	**1.09E-03**
6.1	50	6.01	18.93	42.56	114.27	106.05	**1.08E-03**
6.2	50	6.12	19.29	43.60	117.97	109.62	**1.09E-03**
6.3	50	6.26	19.76	47.15	123.76	114.43	**1.09E-03**
6.4	50	6.35	20.07	48.61	127.43	117.79	**1.09E-03**
6.5	50	6.44	20.42	50.28	131.52	121.53	**1.09E-03**
6.6	50	6.54	20.80	52.15	136.03	125.64	**1.08E-03**
6.7	50	6.65	21.15	54.03	140.67	129.88	**1.08E-03**
6.8	50	6.74	21.55	55.91	145.32	134.13	**1.08E-03**
6.9	50	6.84	21.91	57.58	149.78	138.27	**1.08E-03**
7	50	6.94	22.31	60.08	154.82	142.68	**1.07E-03**
7.1	50	7.01	22.73	62.17	159.72	147.13	**1.06E-03**
7.2	50	7.13	23.08	63.42	164.47	151.75	**1.06E-03**
7.3	50	7.25	23.47	66.13	170.03	156.64	**1.07E-03**
7.4	50	7.34	23.83	68.43	174.91	161.75	**1.06E-03**
7.5	50	7.41	24.18	69.47	179.27	165.27	**1.06E-03**
7.6	50	7.53	24.63	72.81	185.38	170.48	**1.06E-03**
7.7	50	7.62	25.02	75.10	190.63	175.21	**1.05E-03**
7.8	50	7.73	25.45	78.02	197.05	180.95	**1.05E-03**
7.9	50	7.83	25.87	80.94	202.63	185.76	**1.05E-03**
8	50	7.95	26.31	83.24	209.06	191.78	**1.05E-03**
8.1	50	8.02	26.68	85.32	214.04	196.94	**1.04E-03**
8.2	50	8.13	27.06	88.25	220.14	201.68	**1.04E-03**
8.3	50	8.21	27.49	90.54	226.34	207.44	**1.03E-03**
8.4	50	8.35	27.99	94.50	233.65	213.68	**1.04E-03**
8.5	50	8.42	28.39	96.80	239.17	218.70	**1.03E-03**
8.6	50	8.54	28.86	100.34	246.38	225.02	**1.03E-03**

Figure A.1: Inductor 50Hz test, calculations in bold

8.7	50	8.64	29.32	103.47	253.31	231.21	**1.03E-03**
8.8	50	8.74	29.71	106.60	259.59	236.69	**1.03E-03**
8.9	50	8.83	30.18	109.73	266.29	242.63	**1.02E-03**
9	50	8.93	30.64	112.65	273.51	249.93	**1.01E-03**
9.1	50	9.02	31.11	116.83	280.61	255.14	**1.02E-03**
9.2	50	9.12	31.57	120.16	288.77	262.58	**1.01E-03**
9.3	50	9.23	32.09	124.54	297.31	269.96	**1.00E-03**
9.4	50	9.33	32.56	127.26	303.72	275.77	**1.00E-03**
9.5	50	9.47	33.31	133.51	315.44	285.79	**9.99E-04**
9.6	50	9.53	33.51	135.39	319.36	289.24	**9.99E-04**
9.7	50	9.64	34.03	139.77	327.92	296.64	**9.97E-04**
9.8	50	9.73	34.57	144.36	336.44	303.90	**9.92E-04**
9.9	50	9.81	34.99	147.49	343.33	310.03	**9.89E-04**
10	50	9.92	35.55	152.92	353.76	319.00	**9.82E-04**
10.1	50	10.04	36.13	158.13	362.62	327.36	**9.79E-04**
10.2	50	10.14	36.64	162.51	371.40	333.96	**9.79E-04**
10.3	50	10.23	37.11	166.27	379.60	341.25	**9.76E-04**
10.4	50	10.33	37.64	170.86	388.72	349.16	**9.72E-04**
10.5	50	10.41	38.20	176.28	397.67	356.46	**9.68E-04**
10.6	50	10.51	38.70	181.29	406.66	364.01	**9.65E-04**
10.7	50	10.62	39.27	187.76	417.05	372.40	**9.64E-04**
10.8	50	10.71	39.81	192.34	426.47	380.64	**9.60E-04**
10.9	50	10.80	40.42	197.98	437.10	389.69	**9.53E-04**
11	50	10.94	40.99	204.44	448.53	399.23	**9.55E-04**
11.1	50	11.02	41.51	209.87	457.46	406.48	**9.51E-04**
11.2	50	11.09	41.98	213.83	465.43	413.40	**9.46E-04**
11.3	50	11.20	42.60	221.34	476.97	422.50	**9.45E-04**
11.4	50	11.31	43.23	228.64	489.68	433.03	**9.41E-04**
11.5	50	11.42	43.83	235.32	501.01	442.31	**9.39E-04**
11.6	50	11.52	44.36	241.16	511.16	450.70	**9.38E-04**
11.7	50	11.61	44.87	247.21	521.87	459.26	**9.33E-04**
11.8	50	11.71	45.52	254.51	532.90	468.19	**9.32E-04**
11.9	50	11.80	46.06	260.56	545.11	478.11	**9.26E-04**
12	50	11.91	46.73	268.91	556.61	487.35	**9.27E-04**
12.1	50	11.99	47.25	273.91	566.69	496.10	**9.23E-04**
12.2	50	12.08	47.89	280.17	578.32	505.92	**9.18E-04**
12.3	50	12.22	48.63	291.44	594.11	517.72	**9.18E-04**
12.4	50	12.33	49.31	299.36	607.81	528.98	**9.14E-04**
12.5	50	12.41	49.82	305.62	618.16	537.32	**9.12E-04**
12.6	50	12.50	50.48	313.76	630.73	547.16	**9.08E-04**
12.7	50	12.60	51.12	322.10	644.21	557.91	**9.06E-04**
12.8	50	12.70	51.71	330.66	656.72	567.41	**9.05E-04**
12.9	50	12.79	52.22	337.96	667.78	575.95	**9.04E-04**
13	50	12.91	52.93	348.81	683.00	587.21	**9.03E-04**
13.1	50	13.01	53.56	357.99	698.46	599.74	**8.98E-04**
13.2	50	13.13	54.19	366.96	711.28	609.31	**9.00E-04**
13.3	50	13.20	54.77	374.68	724.74	619.75	**8.95E-04**
13.4	50	13.30	55.44	383.85	737.39	629.60	**8.94E-04**
13.5	50	13.41	56.11	394.49	752.40	640.68	**8.93E-04**
13.6	50	13.50	56.68	402.00	765.09	650.97	**8.91E-04**
13.7	50	13.61	57.38	412.64	780.86	662.92	**8.89E-04**
13.8	50	13.72	58.13	423.70	797.62	675.78	**8.87E-04**
13.9	50	13.82	58.73	433.51	811.40	685.89	**8.86E-04**
14	50	13.91	59.36	443.10	825.50	696.50	**8.84E-04**
14.1	50	14.02	60.07	454.58	842.33	709.14	**8.83E-04**
14.2	50	14.10	60.64	462.92	854.78	718.58	**8.80E-04**
14.3	50	14.20	61.31	474.19	872.08	730.95	**8.78E-04**
14.4	50	14.30	62.03	485.45	886.90	742.25	**8.77E-04**
14.5	50	14.40	62.69	496.51	902.62	753.79	**8.75E-04**
14.6	50	14.51	63.42	508.61	920.28	766.96	**8.74E-04**
14.7	50	14.61	64.03	518.62	937.12	779.56	**8.71E-04**

Figure A.2: Inductor 50Hz test - continued

Voltage (mV)	Current (A)	Resistance (mΩ)
13.4	0.83	**16.1**
15.6	0.95	**16.3**
17.4	1.07	**16.3**
19.2	1.18	**16.2**
20.8	1.28	**16.3**
22.2	1.36	**16.3**
24.2	1.49	**16.2**
26.4	1.62	**16.3**
28.5	1.76	**16.2**
30.6	1.88	**16.3**
32.6	2.00	**16.3**
		16.3

Figure A.3: Inductor DC resistance test

APPENDIX **B**

Tests on Think Induction Motor

B.1   Stator resistance test

The stator resistance is measured by applying a DC voltage between two of the three motor terminals. Thus, a DC current will flow through two phase windings and two times the stator resistance will be found from the voltage-current slope. The result for a measurement between two terminals is found in fig. B.1. The dots mark the measurements, the line shows the added trendline, and the trendline equation is shown on the chart. Evidently, the combined stator resistance of two phase windings is 20.1mΩ, and the stator resistance for one phase winding is hence 10.05mΩ ≈ 10mΩ. That is, in the equivalent circuit diagram in fig. 2.13 we have:

$$R_1 = 10\text{m}\Omega \tag{B.1}$$

The cables from the power amplifier to the motor constitutes another series resistance, not attributable to the stator winding. Since these cables are rather long
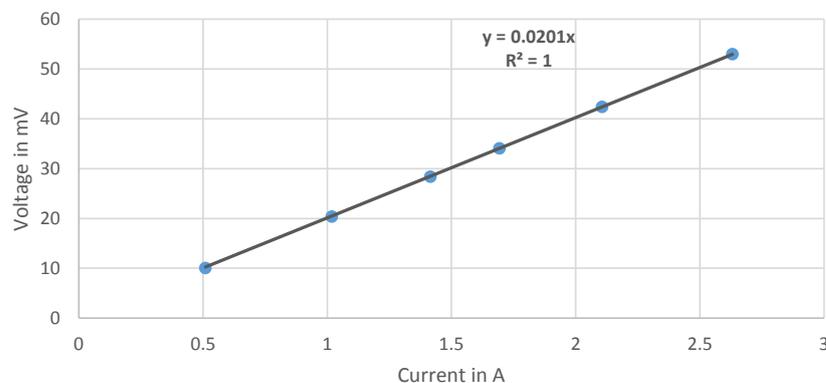

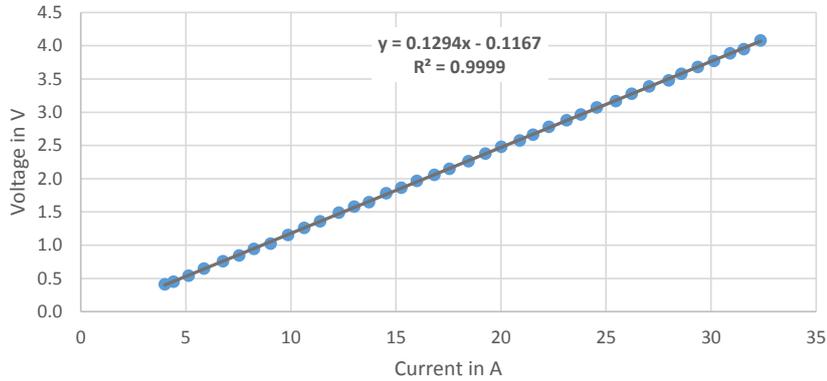**Figure B.1:** Line-line DC voltage-current characteristic

Figure B.2: Line-line DC voltage-current characteristic from amplifier

in the lab setup, it is important to estimate this cable resistance. Thus, a similar resistance test was made by connecting the amplifier between two motor terminals and applying a DC voltage to these. The resulting voltage-current characteristic is shown in fig. B.2 along with a trendline. It is seen that the total series resistance was found to be 129.4mΩ. A non-zero voltage at zero current is projected by the trendline (the second term in the trendline equation), which must be attributed to e.g. a miscalibration or a leakage current flowing internally in the amplifier. In any case, this term is small and will be neglected.

Two times phase winding resistance and two times amplifier to motor cable series resistance are included in the 129.4mΩ estimate. Hence, the series resistance for the part of the cable from the amplifier to the motor, excluding stator windings, is:

$$R_{cable} = \frac{129.4\text{m}\Omega - 20.1\text{m}\Omega}{2} \approx 55\text{m}\Omega \tag{B.2}$$

This is almost 6 times larger than the stator winding resistance, and is therefore important to take into account in the calculations in the following sections.

B.2 Blocked rotor test

The IM equivalent circuit diagram was shown in fig. 2.13. In the blocked rotor test, the slip s is 1. Therefore, the rotor resistance will be equal to R_2, and the current through the magnetizing branch can be neglected, as shown in fig. B.3. Since R_1 is known from the previous test, R_2 can be estimated from the active power dissipated. Furthermore, $X_{leak} = X_1 + X_2$ can be found from the reactive power. A rough assumption is that leakage reactance is equally shared among the stator and rotor [35], thus $X_1 = X_2 = \frac{X_{leak}}{2} = \frac{X_1+X_2}{2}$.

The applied 50Hz three-phase voltage is changed in steps of 0.5V. Measurements are shown in fig. B.4. These are per-phase measurements, and the total leakage reactance can thus be found by:
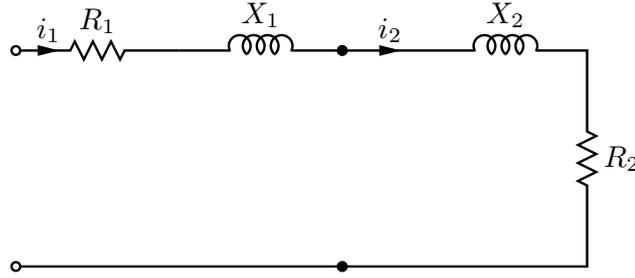
Figure B.3: IM equivalent circuit in blocked rotor test

Set V	1	1.5	2	2.5	3	3.5	4	4.5	5	5.5
Set freq	50	50	50	50	50	50	50	50	50	50
V	1.17	1.54	2.00	2.49	3.01	3.46	3.80	4.30	4.77	5.45
A	7.35	12.55	18.32	24.03	29.87	35.28	38.78	44.74	50.40	58.35
P	4.59	11.68	25.24	43.81	68.84	95.55	117.03	161.05	196.31	262.86
S	8.58	19.26	36.50	59.91	89.90	121.97	147.18	199.25	240.53	317.88
Q	7.25	15.31	26.37	40.86	57.81	75.82	89.24	117.32	138.99	178.75
Scale, kg	0	0	0	0	0.16	0.36	0.46	0.68	0.88	1.06
Torque	**0**	**0**	**0**	**0**	**0.63**	**1.41**	**1.81**	**2.67**	**3.46**	**4.16**
R_tot	**0.085**	**0.074**	**0.075**	**0.076**	**0.077**	**0.077**	**0.078**	**0.080**	**0.077**	**0.077**
R2	**-1.460**	**-1.471**	**-1.470**	**-1.469**	**-1.468**	**-1.468**	**-1.467**	**-1.465**	**-1.468**	**-1.468**
Xleak	**1.34E-01**	**9.73E-02**	**7.85E-02**	**7.08E-02**	**6.48E-02**	**6.09E-02**	**5.93E-02**	**5.86E-02**	**5.47E-02**	**5.25E-02**
Lleak	**4.27E-04**	**3.10E-04**	**2.50E-04**	**2.25E-04**	**2.06E-04**	**1.94E-04**	**1.89E-04**	**1.87E-04**	**1.74E-04**	**1.67E-04**

Figure B.4: Blocked rotor measurements and calculations (bold)

$$X_{leak} = \frac{Q_{leak,1p}}{I_{line}^2} \tag{B.3}$$

Here, $Q_{leak,1p}$ is the per-phase reactive power arising from leakage reactance, and I_{line} is the line current. The leakage inductance is given by:

$$L_{leak} = \frac{X_{leak}}{2\pi f} \tag{B.4}$$

Here, f is the frequency of the supplied voltage. The leakage inductance is calculated in fig. B.4 and two separate measurement series are drawn in fig. B.5 as a function of current. The leakage is at low currents quite high, but becomes nearly constant at currents of about 30A and above, that is, around one fourth of the motor's rated current. Here, the leakage inductance is around $170\mu H$. The decreasing leakage current as a function of current may be attributable to magnetic saturation in certain areas of the stator material. After this initial saturation, the stator material will feature a permeability of μ_0, similar to that of the air gap and copper, and the leakage therefore becomes constant.

The leakage reactance can be found in fig. B.4 for a current close to half the rated current to be approximately $X_{leak} \approx 54m\Omega$. Hence:
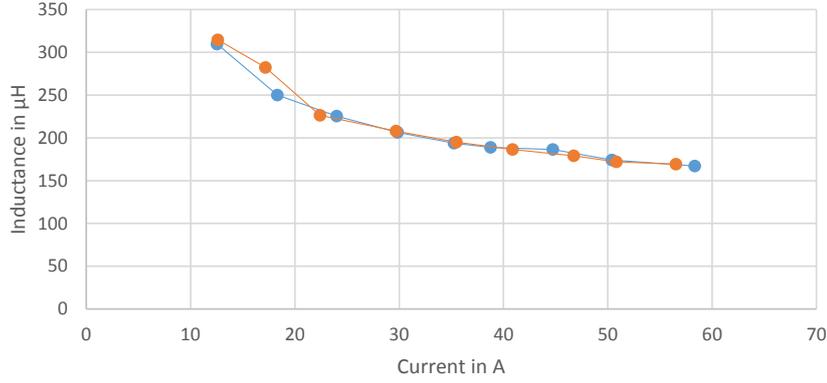
Figure B.5: Per-phase leakage inductance versus current

$$X_1 = X_2 = \frac{X_{leak}}{2} = 26m\Omega \tag{B.5}$$

The rotor resistance R_2 can be estimated in a similar way using active power:

$$R_2 = \frac{P_{1p}}{I_{line}^2} - R_{cable} - R_1 \tag{B.6}$$

The results of this calculation is also shown in fig. B.4. The average of this value is calculated to $16m\Omega$, thus:

$$R_2 = 16m\Omega \tag{B.7}$$

We now have estimated values of R_1, R_2, X_1 and X_2, and we need values for R_c and X_m.

B.3 No-load test

During a no-load test, the slip s is close to 0 because the rotor is allowed to spin freely. Therefore, as seen in fig. B.7 the rotor resistance $\frac{R_2}{s}$ is large and current i_2 can be neglected. The test was performed at rated frequency, 120Hz. The measurements and calculations are found in fig. B.6.

The total no-load reactance X_{nl} is given by:

$$X_{nl} = \frac{Q_{nl}}{I_1^2} \tag{B.8}$$

Set V	Set F	V	A	P	P no friction	S	Q	Xnl	Xm	Rnl	Rc
14	120	13.99	11.03	105.14	5.14	154.43	113.10	0.93	0.90	0.04	-1.98E-02
15	120	14.99	11.14	108.27	8.27	166.87	126.97	1.02	1.00	0.07	4.65E-03
16	120	16.00	11.29	109.11	9.11	180.60	143.91	1.13	1.10	0.07	9.40E-03
17	120	17.00	11.59	113.07	13.07	196.93	161.23	1.20	1.18	0.10	3.53E-02
18	120	17.98	11.82	115.16	15.16	212.59	178.70	1.28	1.25	0.11	4.64E-02
19	120	18.99	12.11	115.57	15.57	229.84	198.67	1.36	1.33	0.11	4.42E-02
20	120	20.00	12.54	119.75	19.75	250.79	220.36	1.40	1.37	0.13	6.35E-02
21	120	21.00	12.96	122.88	22.88	272.16	242.85	1.45	1.42	0.14	7.41E-02
22	120	21.98	13.42	123.71	23.71	294.87	267.67	1.49	1.46	0.13	6.97E-02
23	120	22.99	13.95	125.80	25.80	320.58	293.60	1.51	1.48	0.13	7.05E-02
24	120	23.99	14.41	132.26	32.26	345.70	319.40	1.54	1.51	0.16	9.33E-02
25	120	24.98	14.84	136.02	36.02	370.63	344.77	1.57	1.54	0.16	1.02E-01
26	120	25.97	15.30	137.27	37.27	397.47	372.34	1.59	1.56	0.16	9.71E-02
27	120	26.99	15.88	143.53	43.53	428.43	403.67	1.60	1.58	0.17	1.11E-01
28	120	27.99	16.44	148.12	48.12	460.17	435.68	1.61	1.58	0.18	1.16E-01
29	120	28.98	17.02	151.04	51.04	493.19	469.49	1.62	1.59	0.18	1.14E-01
30	120	29.98	17.62	157.51	57.51	528.21	504.18	1.62	1.60	0.19	1.23E-01
31	120	30.99	18.22	163.14	63.14	564.54	540.46	1.63	1.60	0.19	1.28E-01
32	120	31.98	18.84	170.65	70.65	602.32	577.64	1.63	1.60	0.20	1.37E-01
33	120	32.99	19.47	175.66	75.66	642.31	618.22	1.63	1.60	0.20	1.38E-01
34	120	33.99	20.08	177.74	77.74	682.51	658.96	1.63	1.61	0.19	1.31E-01
35	120	34.98	20.75	184.63	84.63	725.70	701.83	1.63	1.60	0.20	1.35E-01
36	120	35.99	21.37	191.72	91.72	769.01	744.73	1.63	1.60	0.20	1.39E-01
37	120	36.98	22.03	197.98	97.98	814.69	790.21	1.63	1.60	0.20	1.40E-01
38	120	37.98	22.74	203.40	103.40	863.60	839.30	1.62	1.60	0.20	1.38E-01
39	120	38.97	23.42	210.91	110.91	912.49	887.78	1.62	1.59	0.20	1.40E-01
40	120	39.97	24.10	217.38	117.38	963.47	938.62	1.62	1.59	0.20	1.40E-01
41	120	40.97	24.80	221.97	121.97	1016.67	991.39	1.61	1.59	0.20	1.36E-01
42	120	41.98	25.53	229.69	129.69	1071.47	1046.56	1.61	1.58	0.20	1.37E-01
43	120	42.97	26.25	242.41	142.41	1128.32	1101.97	1.60	1.57	0.21	1.45E-01
44	120	43.98	27.01	250.55	150.55	1187.86	1161.13	1.59	1.57	0.21	1.44E-01
45	120	44.98	27.74	254.10	154.10	1248.40	1222.27	1.59	1.56	0.20	1.38E-01
46	120	45.97	28.52	262.02	162.02	1311.00	1283.51	1.58	1.55	0.20	1.37E-01
47	120	46.96	29.35	272.66	172.66	1377.88	1351.14	1.57	1.54	0.20	1.38E-01
48	120	47.98	30.21	284.14	184.14	1449.60	1421.48	1.56	1.53	0.20	1.40E-01
49	120	48.98	31.08	289.77	189.77	1522.13	1494.29	1.55	1.52	0.20	1.34E-01
50	120	49.97	31.95	298.32	198.32	1596.44	1568.32	1.54	1.51	0.19	1.32E-01
51	120	50.96	32.82	311.05	211.05	1671.18	1641.98	1.52	1.50	0.20	1.34E-01
52	120	51.96	33.77	320.02	220.02	1753.72	1724.08	1.51	1.49	0.19	1.31E-01
53	120	52.97	34.72	330.66	230.66	1838.80	1808.83	1.50	1.47	0.19	1.29E-01
54	120	53.97	35.74	343.59	243.59	1931.08	1900.26	1.49	1.46	0.19	1.29E-01
55	120	54.97	36.85	350.27	250.27	2025.39	1994.88	1.47	1.44	0.18	1.22E-01
56	120	55.97	37.96	368.21	268.21	2124.10	2091.94	1.45	1.43	0.19	1.24E-01
57	120	56.97	39.23	382.60	282.60	2235.34	2202.35	1.43	1.40	0.18	1.22E-01
58	120	57.96	40.52	396.16	296.16	2347.57	2313.90	1.41	1.38	0.18	1.18E-01
59	120	58.96	41.85	423.70	323.70	2467.38	2430.73	1.39	1.36	0.18	1.23E-01
60	120	59.97	43.38	431.84	331.84	2601.51	2565.41	1.36	1.34	0.18	1.14E-01
61	120	60.97	44.98	452.49	352.49	2742.29	2702.84	1.34	1.31	0.17	1.12E-01
62	120	61.97	46.59	470.22	370.22	2887.58	2849.04	1.31	1.29	0.17	1.08E-01
63	120	62.96	48.40	492.96	392.96	3047.20	3007.06	1.28	1.26	0.17	1.06E-01
64	120	63.96	50.28	526.34	426.34	3215.93	3172.56	1.25	1.23	0.17	1.07E-01
65	120	64.95	52.49	549.08	449.08	3408.89	3364.38	1.22	1.19	0.16	1.01E-01
66	120	65.95	54.75	581.41	481.41	3608.38	3560.00	1.19	1.16	0.16	9.86E-02
67	120	66.96	57.13	619.38	519.38	3825.23	3774.75	1.16	1.13	0.16	9.71E-02
68	120	67.94	59.67	652.76	552.76	4053.96	4001.06	1.12	1.10	0.16	9.32E-02
69	120	68.95	62.39	697.61	597.61	4301.62	4244.68	1.09	1.06	0.15	9.15E-02
69	120	68.95	62.35	684.89	584.89	4298.79	4243.88	1.09	1.07	0.15	8.84E-02

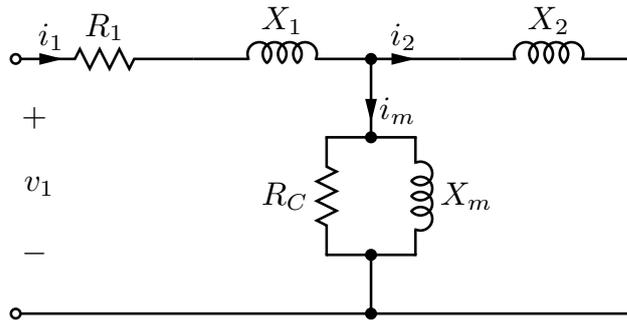**Figure B.6:** No load measurements and calculations

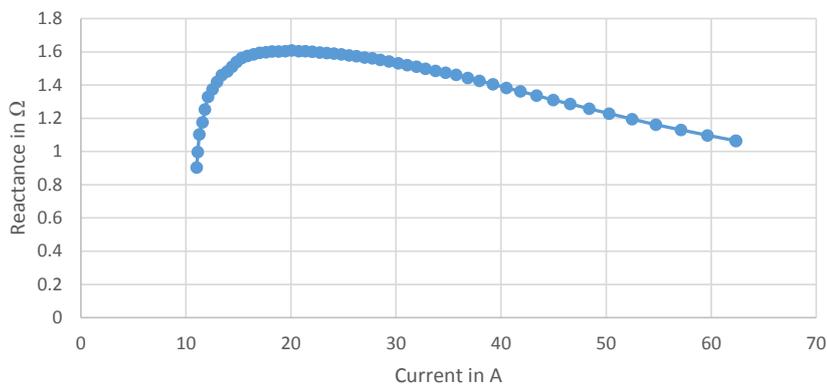**Figure B.7:** IM equivalent circuit in no-load test

Figure B.8: Per-phase magnetizing reactance versus current

Here, I_1 is the line rms current and Q_{nl} is the consumed reactive power. The magnetizing reactance can be found from:

$$X_m = X_{nl} - X_1 \tag{B.9}$$

The magnetizing reactance is found in fig. B.8. It is evident that the reactance is nearly constant at currents above 15A and voltages above 25V. Below these numbers, the reactance drops rapidly, which is due to frictional losses which entails a minimum consumption of active power to spin the motor and wheels, around 100W per-phase (see fig. B.6 at low voltages). Therefore, the slip increases, the i_2 current cannot be neglected, and X_{nl} in eq. (B.8) drops. For higher currents and voltages, the magnetizing reactance drops as well which is due to saturation in the core material. Based on the graph, the magnetizing reactance is roughly estimated to:

$$X_m \approx 1.4\Omega \tag{B.10}$$

Since we can estimate frictional losses P_{fric} to be around 100W per phase, this power can be subtracted from the measured no-load power to yield the power consumed by the motor core material:
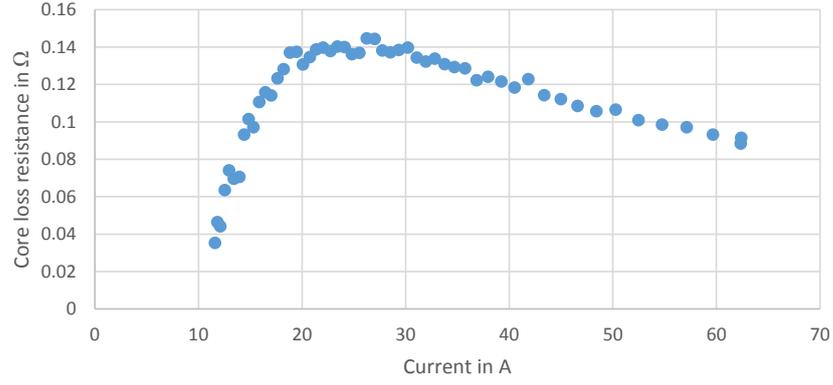
Figure B.9: Per-phase equivalent core loss resistance

$$R_{nl} = \frac{P_{nl} - P_{fric}}{I_1^2} \tag{B.11}$$

$$R_c = R_{nl} - R_1 - R_{cable} \tag{B.12}$$

The core loss resistance is found in fig. B.9. Again, at currents below 15A, the assumption of negligible i_2 current does not hold, and R_c drops rapidly. For higher currents, the resistance is nearly constant but drops slowly due to increasing core losses when the motor material is driven into saturation. Based on the graph, the core loss is rougly estimated to:

$$R_c \approx 0.12\Omega \tag{B.13}$$

Note that this value is approximately 12 times larger than the stator winding resistance R_1 and 8 times larger than the rotor resistance R_2.

B.4 Dynamic torque curve

Based on the above estimated values, it is possible to calculate the dynamic torque characteristic of the motor. First, we need to find the mechanical power delivered by the rotor. This can be found from fig. 2.13. The per-phase power transfered across the air gap to the rotor P_{gap} is:

$$P_{gap} = I_2^2 \frac{R_2}{s} \tag{B.14}$$

The torque is given by the n_{ph}-phase air gap power divided by the synchronous frequency $\omega_s = 2\pi f_s$ [35]:

$$T_{mech} = n_{ph}\frac{P_{gap}}{\omega_s} = n_{ph}I_2^2\frac{R_2}{\omega_s s} \tag{B.15}$$

The current I_2 should be found from the terminal voltage V_1. This is done by applying the Thevenin theorem to the circuit consisting of R_1, X_1, R_c and X_m of fig. 2.13. With this approach, the circuit components placed in parallel can be replaced with an equivalent voltage source ($V_{1,eq}$) in series with an impedance ($Z_{1,eq}$). The derivation can be found in [35]. The result is:

$$\boldsymbol{V_{1,eq}} = V_1 \frac{Z_m}{R_1 + jX_1 + Z_m} \tag{B.16}$$

$$Z_{1,eq} = \frac{Z_m(R_1 + jX_1)}{R_1 + jX_1 + Z_m} \tag{B.17}$$

Here, $Z_m = R_c + jX_m$. The current supplied by the equivalent voltage source is equal to I_2 from eq. (B.15):

$$\boldsymbol{I_2} = \frac{\boldsymbol{V_{1,eq}}}{Z_{1,eq} + jX_2 + R_2/s} \tag{B.18}$$

Inserting eq. (B.18) into eq. (B.15), and inserting numbers from the previous estimated motor parameters into this equation we get the motor's torque curve as shown in fig. B.10. Here, three values of V_1 are shown, which is in the vicinity of the voltages used during the blocked rotor test as seen in fig. B.4, which corresponds to motor currents of around 30A for 3V to 58A for 5.5V. Note this is similar to the currents used in fast-charging applications (up to 63A). The torque characteristic has been multiplied by the speed reduction ratio in the gearbox, which is 10.15 [2]. It is seen that we expect a motor torque of up to around 8Nm for the maximum current that will flow through the motor while it is at standstill ($f = 0$Hz) during charging. We can try to reproduce these values through an actual torque measurement when the rotor is blocked. It should at this point be noted that 8Nm is a rather low torque, making rotor restraining relatively easy.

B.5   50Hz torque test

It was not possible to measure the dynamic torque while the wheels were moving. However, this is not necessary to determine its feasibility for using the leakage reactance for charging purposes. The reason is that the rotor must be blocked during charging anyway, and hence we only have to measure the starting torque. The starting torque was measured quite simply by locking one of the wheels, mounting a lever on the other, and measure the pressure exerted on a scale placed a certain distance from the center of the wheel. This setup is shown in fig. 2.20c. The torque is then given by:

$$T_{start} = r \cdot m_{scale} \cdot g \tag{B.19}$$

Here, T_{start} is the starting torque, r is the distance from the centre of the wheel to the point where the scale touches the lever, m_{scale} is the measured weight on the scale and g is the gravitational acceleration (9.82m/s^2).
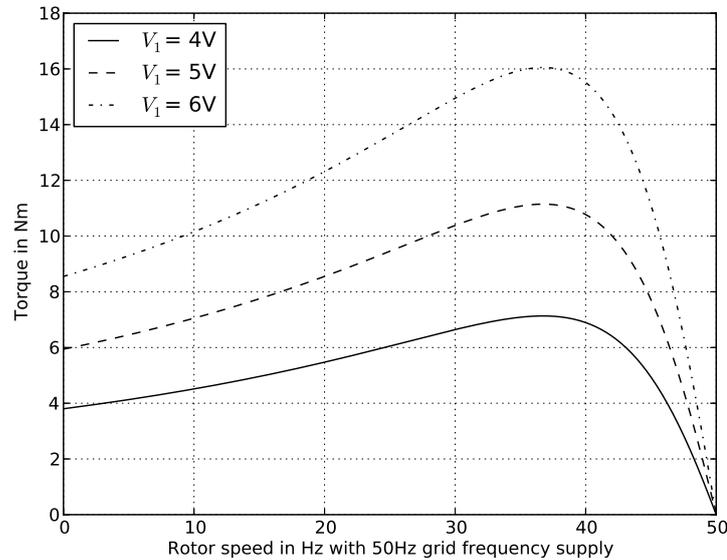
Figure B.10: Torque versus current at 50Hz supply frequency

The start-up torque measurements with 50Hz supply frequency were performed using a lever arm length of 20cm. The resulting scale readings and torque is shown in fig. B.4. Note that the measurement was only done on one wheel and the torque has therefore been multiplied by two to yield the actual torque at the gearbox. The torque is drawn in fig. B.11. Evidently, the torque increases linearly with current (and voltage), and a torque of 4.2Nm is achieved at a line current of 58A.

These measurements are lower than predicted in previous section, but this may be attributable to inaccuracies in the experimental setup, e.g. slightly rusty brakes on the vehicle and static friction in bearings, gears and differential. However, the tendency of increasing torque at increasing currents is clear, and it is also evident that the starting torque at a supply frequency of 50Hz is quite low.
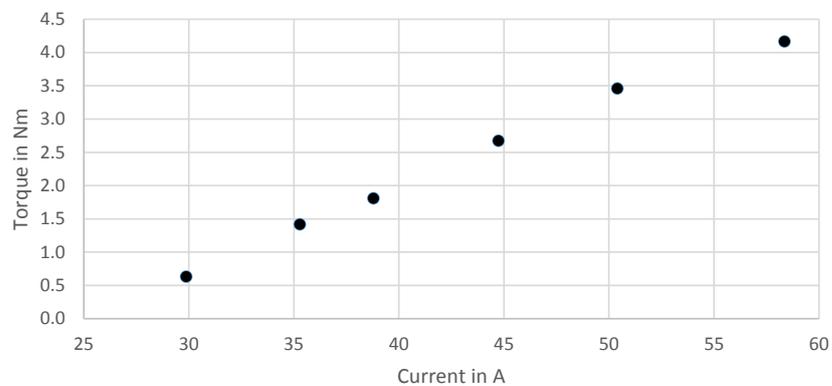

Figure B.11: Blocked rotor torque versus current at 50Hz supply frequency

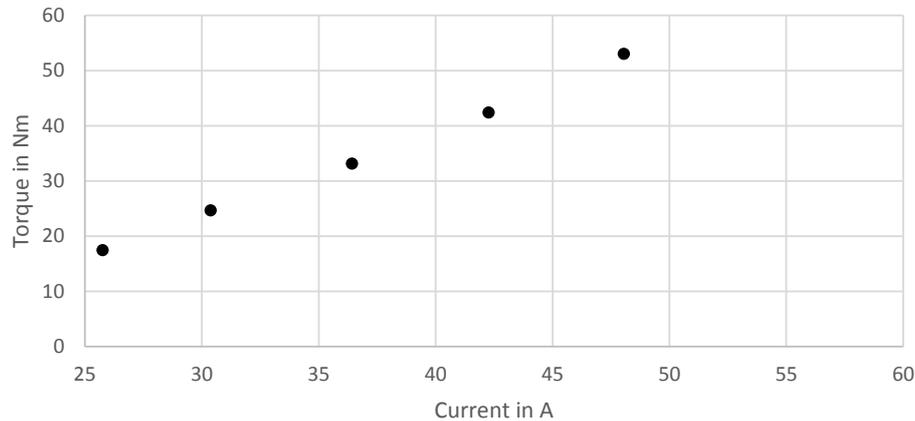| Set V	1	1.5	2	2.5	3	3.5	4	4.5
Set freq	3	3	3	3	3	3	3	3
Scale, kg	1.38	2.02	2.98	4.44	6.28	8.44	10.8	13.5
Torque	5.4	7.9	11.7	17.4	24.7	33.2	42.4	53.0

Figure B.12: Max torque test

Figure B.13: Blocked rotor torque versus current at 3Hz supply frequency

B.6 Max torque test

To compare the previous torque measurements with the motor torque capability, the motor was supplied 3Hz and the measurements were repeated. They are shown in fig. B.12. The torque versus current is drawn in fig. B.13, and the torque curve is shown in fig. B.14 for three voltages and three specific blocked-rotor currents.

The torque is much higher at this low supply frequency. The torque was measured to around 4Nm with 50Hz supply frequency, and is now measured to 53Nm at 3Hz supply frequency. The supply currents are similar in the two tests (50A versus 48A).

Roughly comparing the theoretical and practical findings, it is seen that the practical measurements are a bit lower than the calculated torque curve in fig. B.14. According to the torque calculations based on motor parameters, the torque at 48A should have been closer to 70Nm rather than the measured 53Nm. However, this may again be due to static friction in the setup, as well as to errors in measurement equipment. The voltage is quite low while the current is high in these tests, so this may have resulted in erroneous readings. Furthermore, the theoretical curve is only based on single values of the motor parameters, which was shown previously to vary a lot with varying voltage and current. Therefore, it is assessed that the presented measurements have acceptable accuracy, and the fundamental principles have been validated.
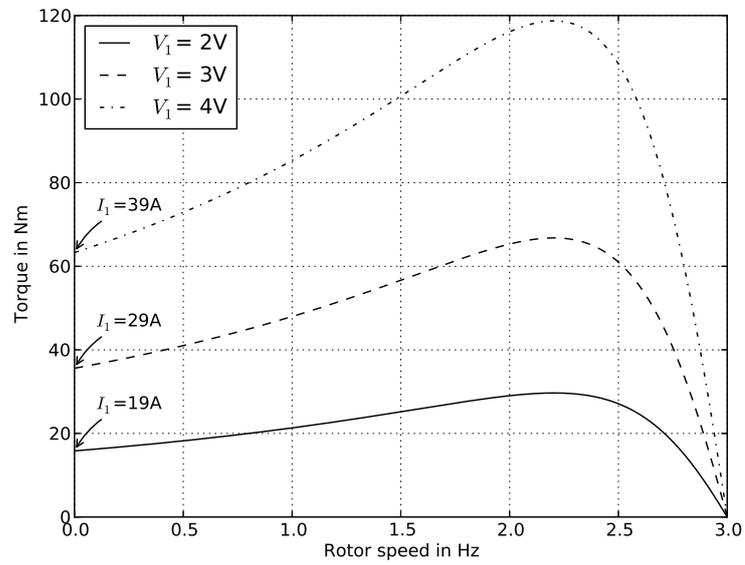
Figure B.14: Torque versus current at 3Hz supply frequency

APPENDIX C

Python script for amplifier measurements

Below is the script used for controlling the power amplifier and obtaining measurements for further processing in Excel. The Python program uses the PyVisa package for communication through a USB to GPIB bus interface to the amplifier, see [12].

The measurements are saved in a log file, called log.csv, which is easily imported into Excel. The program works by pressing button a to decrease frequency by 1Hz, d to increase frequency by 1Hz, w to increase voltage by 0.5V and s to decrease voltage by 0.5V. Button g saves the measurements to the log file. Button q quits the program.

This script serves as an example only, and is written to quickly obtain measurement results from the amplifier. Additional error checking is needed.

```python
1  from visa import *
2  import os
3  import msvcrt
4
5  def get_num(x):
6      return float(''.join(ele for ele in x if ele.isdigit() or ele=='.'))
7
8  instruments = "none"
9  try:
10         instruments = get_instruments_list()
11 except:
12         pass
13
14 print "Instruments:\n" + " ".join(instruments)
15
16 voltage = 0.5
17 frequency = 50
18
19 instr = instrument("GPIB0::6")
20 instr.term_chars = LF
21 print instr.ask("*IDN?")
22
23 instr.write("conf:meas:ph 1")
24 print "Measuring on phase " + instr.ask("conf:meas:ph?")
25
26 flog = open("log.csv","w")
```

```
27 flog.write("setV,setF,V,A,P,S,Q,PF\n")
28 print "Input (w,s,a,d,g):"
29 while True:
30
31         input = msvcrt.getch()
32
33         if input[0] == "w":
34                 voltage = voltage + 0.5
35                 instr.write("osc:amp:accept 0")
36                 instr.write("osc:amp 1,{0}V".format(voltage))
37                 instr.write("osc:amp 2,{0}V".format(voltage))
38                 instr.write("osc:amp 3,{0}V".format(voltage))
39                 instr.write("osc:amp:accept 1")
40                 print str(voltage) + "V"
41         elif input[0] == "s":
42                 voltage = voltage - 0.5
43                 instr.write("osc:amp:accept 0")
44                 instr.write("osc:amp 1,{0}V".format(voltage))
45                 instr.write("osc:amp 2,{0}V".format(voltage))
46                 instr.write("osc:amp 3,{0}V".format(voltage))
47                 instr.write("osc:amp:accept 1")
48                 print str(voltage) + "V"
49         elif input[0] == "a":
50                 frequency = frequency - 1
51                 instr.write("osc:freq {0}".format(frequency))
52                 print str(frequency) + "Hz"
53         elif input[0] == "d":
54                 frequency = frequency + 1
55                 instr.write("osc:freq {0}".format(frequency))
56                 print str(frequency) + "Hz"
57         elif input[0] == "q":
58                 break
59         elif input[0] == "g":
60                 mv = instr.ask("meas:volt?")
61                 mc = instr.ask("meas:curr?")
62                 mp = instr.ask("meas:pow?")
63                 ms = instr.ask("meas:s?")
64                 mq = instr.ask("meas:q?")
65                 mpf = instr.ask("meas:pf?")
66                 mf = instr.ask("meas:freq?")
67                 flog.write("{0},{1},{2},{3},{4},{5},{6},{7}".format(...
                    voltage,frequency,get_num(mv), get_num(mc), get_num(mp...
                    ), get_num(ms), get_num(mq), get_num(mpf))+'\n')
68                 flog.flush()
69                 print mv,mc,mp
70         else:
71                 print "Input (w,s,a,d,g):"
72
73 flog.close()
```

Example calculation on AC versus DC power transfer

Assume a charging cable has 4mΩ of resistance per conductor[1]. There are four conductors in the cable. Furthermore, we assume this cable should transfer 40kW to a resistive load. In the case of DC, the voltage is 400VDC, and in the case of AC, the line-line voltage is 400V RMS, corresponding to 230V line-neutral RMS. The DC connection is allowed to use two conductors for its positive terminal, and the other two conductors for its negative terminal, meaning the resistance is 2mΩ per terminal. With DC power transfer, the current through the cable is:

$$I_{dc} = \frac{40\text{kW}}{400\text{V}} = 100\text{A} \tag{D.1}$$

With DC, the positive terminal conducts the forward current whereas the negative terminal conducts the return current. The resistive losses in the cable with DC can then be found per terminal and multiplied by two:

$$P_{loss,dc} = 2 \cdot 100\text{A}^2 \cdot 2\text{m}\Omega = 40W \tag{D.2}$$

With three-phase AC, one conductor is used for each of the three phases. The fourth conductor is the neutral. The current through each phase/conductor is:

$$I_{phase} = \frac{40\text{kW}}{3 \cdot 230\text{V}} \approx 58\text{A} \tag{D.3}$$

With balanced AC, the current sums to zero at the load and thus no current runs through the neutral. Thus, the resistive losses can be found per conductor and multiplied by three:

---

[1]This is the case for a copper cable with a cross section of 10mm^2 and a length of 2.4m

$$P_{loss,ac} = 3 \cdot 58A^2 \cdot 4\text{m}\Omega = 40W \tag{D.4}$$

Hence, the resistive losses are equal between AC and DC power transfer, in this case 40W.

However, due to the fact that the neutral does not carry any current with three-phase balanced loads, it can be omitted. This means we can do with only three conductors in a cable, which changes the above calculations for DC. With three conductors, we imagine that we split one conductor for each of the DC terminals, and we can then use the copper from one and a half conductor per terminal, resulting in a conductor resistance of $3m\Omega$. This increases the DC losses to:

$$P_{loss,dc} = 2 \cdot 100\text{A}^2 \cdot 3\text{m}\Omega = 60W \tag{D.5}$$

In this way, three-phase AC features lower losses per cross section of conductor given that the neutral is not included, resulting in less required copper and less weight. This is also one (smaller) argument for using an AC grid over a DC grid.

Note the benefit of using AC is only present when three-phase connections are used. With single-phase connections, one hot wire and one neutral are required to conduct the forward and return current, respectively, which is somewhat similar to DC. However, the instantaneous power transfer with single-phase AC is varying (by the double frequency) which makes it difficult to deliver constant power to the battery.

dq control in three-phase converter

Using the *dq* transform as expressed in eq. (2.56) we can find the *dq* components of a balanced three-phase voltage:

$$v_{g,d} = \frac{2}{3}\left(v_{g,a}\cos(\omega t) + v_{g,b}\cos(\omega t - \frac{2\pi}{3}) + v_{g,c}\cos(\omega t - \frac{4\pi}{3})\right) \tag{E.1}$$

$$v_{g,q} = -\frac{2}{3}\left(v_{g,a}\sin(\omega t) + v_{g,b}\sin(\omega t - \frac{2\pi}{3}) + v_{g,c}\sin(\omega t - \frac{4\pi}{3})\right) \tag{E.2}$$

$$v_{c,d} = \frac{2}{3}\left(v_{c,a}\cos(\omega t) + v_{c,b}\cos(\omega t - \frac{2\pi}{3}) + v_{c,c}\cos(\omega t - \frac{4\pi}{3})\right) \tag{E.3}$$

$$v_{c,q} = -\frac{2}{3}\left(v_{c,a}\sin(\omega t) + v_{c,b}\sin(\omega t - \frac{2\pi}{3}) + v_{c,c}\sin(\omega t - \frac{4\pi}{3})\right) \tag{E.4}$$

This can be done similarly for a balanced three-phase current:

$$i_d = \frac{2}{3}\left(i_a\cos(\omega t) + i_b\cos(\omega t - \frac{2\pi}{3}) + i_c\cos(\omega t - \frac{4\pi}{3})\right) \tag{E.5}$$

$$i_q = -\frac{2}{3}\left(i_a\sin(\omega t) + i_b\sin(\omega t - \frac{2\pi}{3}) + i_c\sin(\omega t - \frac{4\pi}{3})\right) \tag{E.6}$$

Taking the derivative of the currents *d*-component:

$$\frac{d}{dt}i_d = \frac{2}{3}\Big(\frac{di_a}{dt}\cos(\omega t) - i_a\omega\sin(\omega t)+$$
$$\frac{di_b}{dt}\cos(\omega t - \frac{2\pi}{3}) - i_b\omega\sin(\omega t - \frac{2\pi}{3})+$$
$$\frac{di_c}{dt}\cos(\omega t - \frac{4\pi}{3}) - i_c\omega\sin(\omega t - \frac{4\pi}{3})\Big) \tag{E.7}$$

$$= \frac{2}{3}\Big(\frac{di_a}{dt}\cos(\omega t) + \frac{di_b}{dt}\cos(\omega t - \frac{2\pi}{3}) + \frac{di_c}{dt}\cos(\omega t - \frac{4\pi}{3})\Big)$$
$$- \frac{2}{3}\omega\Big(i_a\sin(\omega t) + i_b\sin(\omega t - \frac{2\pi}{3}) + i_c\sin(\omega t - \frac{4\pi}{3})\Big)$$

The KVL equations for the converter are expressed in eq. (2.58), and some rearranging gives

$$L\frac{d}{dt}\begin{bmatrix} i_a \\ i_b \\ i_c \end{bmatrix} = \begin{bmatrix} v_{g,a} \\ v_{g,b} \\ v_{g,c} \end{bmatrix} - R\begin{bmatrix} i_a \\ i_b \\ i_c \end{bmatrix} - \begin{bmatrix} v_{c,a} \\ v_{c,b} \\ v_{c,c} \end{bmatrix} \tag{E.8}$$

Inserting eq. (E.8) into eq. (E.7) yield:

$$L\frac{di_d}{dt} = \frac{2}{3}\Big((v_{g,a} - v_{c,a} - Ri_a)\cos(\omega t)+$$
$$(v_{g,b} - v_{c,b} - Ri_b)\cos(\omega t - \frac{2\pi}{3})+ \tag{E.9}$$
$$(v_{g,c} - v_{c,c} - Ri_c)\cos(\omega t - \frac{4\pi}{3})\Big) + L\omega i_q$$

Recognizing similar terms in eq. (E.1):

$$L\frac{di_d}{dt} = v_{g,d} - v_{c,d} - Ri_d + \omega i_q \tag{E.10}$$

This can be done similarly for i_q:

$$\frac{di_q}{dt} = \frac{2}{3}\Big(\frac{di_a}{dt}\sin(\omega t) + \frac{di_b}{dt}\sin(\omega t - \frac{2\pi}{3}) + \frac{di_c}{dt}\sin(\omega t - \frac{4\pi}{3})\Big)$$
$$- \frac{2}{3}\omega\Big(i_a\cos(\omega t) + i_b\cos(\omega t - \frac{2\pi}{3}) + i_c\cos(\omega t - \frac{4\pi}{3})\Big) \tag{E.11}$$

$$L\frac{di_q}{dt} = \frac{2}{3}\Big((v_{g,a} - v_{c,a} - Ri_a)\sin(\omega t)+$$
$$(v_{g,b} - v_{c,b} - Ri_b)\sin(\omega t - \frac{2\pi}{3})+ \tag{E.12}$$
$$(v_{g,c} - v_{c,c} - Ri_c)\sin(\omega t - \frac{4\pi}{3})\Big) - L\omega i_d$$

Again recognizing similar terms:

$$L\frac{di_q}{dt} = v_{g,q} - v_{c,q} - Ri_q - L\omega i_d \tag{E.13}$$

Solving eqs. (E.10) and (E.13) for the grid voltage:

$$
\begin{aligned}
v_{g,d} &= L\frac{di_d}{dt} + v_{c,d} + Ri_d - L\omega i_q \\
v_{g,q} &= L\frac{di_q}{dt} + v_{c,q} + Ri_q + L\omega i_d
\end{aligned}
\tag{E.14}
$$

Which is the desired result.

Appendix F

Industry terminology

The industry terminology in relation to fast-charging is often misused, because the term "fast-charging" or "quick-charging" almost always refer to the use of DC off-board chargers. This is a problem, because AC charging stations can provide as much power as some DC charging stations. It is important to make the distinction between AC and DC fast-charging because otherwise decision-makers and infrastructure planners will not be able to clearly assess the advantages and disadvantages of the two charging methods. If people are told fast-charging requires DC, and AC implies slow-charging then the benefits of AC charging may not surface.

Developing sensible road signs and interactive maps could be an important step in the direction of enlightening the EV industry about the various charging methods. Instead of simply telling people that "there is a charging post at this location", it should be told which connector is available (Type 1, Type 2 or DC), and the power it offers. It would be natural to show these differences with fancy graphics, but the main point is that the EV industry and the EV end user has to know these basic differences. This is not too much detail - for example, how many know what the octane rating means at the local gas station? Yet, people fill their vehicles with the right type of gas every day.

So, the EV industry has to change its terminology and explicitly use the terms AC or DC in relation to fast-charging, the AC connector type (or, alternatively, number of phases, 1 or 3) and how much power the charging station is capable of delivering.

APPENDIX G

EV communication test

The serial port device shows up as */dev/ttyS4* on both the EV and EVSE Linux board. To test the serial link, we can listen on the port on one end and transmit on the other end. We listen on the serial port in the EVSE by running the following Bash-command:

```
1 [evse:~]$ cat < /dev/ttyS4 > annexd.log &
```

This records everything on the serial line and saves it in the file *annexd.log*. We can switch to the EV side, and transmit some text onto the serial line:

```
1 [ev:~]$ echo "Test Annex D" > /dev/ttyS4
```

Returning to the EVSE, we can print the file contents obtained from the serial line:

```
1 [evse:~]$ cat annexd.log
2 Test Annex D
```

Hence, it is seen the UART communication works fine, and we are now interested in establishing IP communication using this link. This is done using Serial Line IP (SLIP) [http://tools.ietf.org/html/rfc1055] which frames IP data directly onto a serial line. The Linux program *slattach* creates the SLIP network interface:

```
1 [ev:~]$ slattach /dev/ttyS4
2 [evse:~]$ slattach /dev/ttyS4
```

The newly created network interface is called *sl0*. We can check its status:

```
1 [ev:~]$ ip addr show dev sl0
2 4: sl0: <POINTOPOINT,MULTICAST,NOARP> mtu 296 qdisc noop state DOWN
3     link/cslip
```

It is seen the link is down and it is not assigned an IP yet. We will give the EVSE the static IP 172.17.2.1 and the EV 172.17.2.2. So, the IP addresses are set up on the EV by:

```
1 [ev:~]$ ip addr add 172.17.2.2 peer 172.17.2.1/24 dev sl0
2 [ev:~]$ ip link set dev sl0 up
3 [ev:~]$ ip route add default via 172.17.2.2
```

The first command sets the IP, the second IP enables the link, and the last command adds a default gateway through the EVSE, meaning all requests from the EV will be sent to the EVSE. On the EVSE, the following commands are given:

```
1 [evse:~]$ ip addr add 172.17.2.1 peer 172.17.2.2/24 dev sl0
2 [evse:~]$ ip link set dev sl0 up
```

It should now be possible to access the EV from the EVSE and vice versa, so:

```
1 [evse:~]$ ping 172.17.2.2 -c 1
2 PING 172.17.2.2 (172.17.2.2) 56(84) bytes of data.
3 64 bytes from 172.17.2.2: icmp_req=1 ttl=64 time=130 ms
4
5 --- 172.17.2.2 ping statistics ---
6 1 packets transmitted, 1 received, 0% packet loss, time 0ms
7 rtt min/avg/max/mdev = 130.000/130.000/130.000/0.000 ms
```

So the EV and EVSE can now ping each other. However, the EV does not have access to the Internet:

```
1 [ev:~]$ ping 8.8.8.8
2 PING 8.8.8.8 (8.8.8.8): 56 data bytes
3 ^C--- 8.8.8.8 ping statistics ---
4 3 packets transmitted, 0 packets received, 100% packet loss
```

This is caused by the EVSE dropping all packets it receives from the EV because it does not know what to do with them. Instead, we should set up the EVSE to forward all packets it receives from the EVSE on the *sl0* interface to the Internet-connected Ethernet interface *eth0*. To do this, a NAT has to take place, which is set up using the following commands [8]:

```
1 [evse:~]$ iptables -t nat -A POSTROUTING -o eth0 -j MASQUERADE
2 [evse:~]$ iptables -A FORWARD -i eth0 -o sl0 -m state --state RELATED,...
    ESTABLISHED -j ACCEPT
3 [evse:~]$ iptables -A FORWARD -i sl0 -o eth0 -j ACCEPT
```

The EV is now connected to the Internet, and the EV can ping Internet hosts, e.g. *google.com*:

```
1 [ev:~]$ ping google.com
2 PING google.com (109.105.109.249): 56 data bytes
3 64 bytes from 109.105.109.249: icmp_seq=0 ttl=55 time=150.000 ms
4 64 bytes from 109.105.109.249: icmp_seq=1 ttl=55 time=130.000 ms
5 ^C--- google.com ping statistics ---
6 2 packets transmitted, 2 packets received, 0% packet loss
7 round-trip min/avg/max/stddev = 130.000/140.000/150.000/10.000 m
```

We can even make the EV tell us the route it uses to get to a remote host from the DTU network, say to udel.edu, using the traceroute facility:

```
1 [ev:~]$ traceroute -q 1 --resolve-hostnames udel.edu
2 traceroute to udel.edu (128.175.13.92), 64 hops max
3  1    172.17.2.1 (172.17.2.1) 110.000ms
4  2    10.59.128.1 (10.59.128.1) 90.000ms
5  3    10.12.2.25 (10.12.2.25) 90.000ms
6  4    10.12.3.236 (10.12.3.236) 90.000ms
7  5    10.12.3.241 (10.12.3.241) 110.000ms
8  6    130.225.166.241 (10g-dtu.ly0.core.fsknet.dk) 90.000ms
9  7    109.105.102.37 (dk-uni.nordu.net) 90.000ms
10  8    109.105.97.69 (us-man.nordu.net) 210.000ms
11  9    109.105.98.10 (xe-2-3-0.118.rtr.newy32aoa.net.internet2.edu) 210.000
12 10    216.27.100.53 (local.internet2.magpi.net) 190.000ms
13 11    216.27.98.38 (remote.udel1.magpi.net) 210.000ms
14 12    128.175.111.100 (chp-core1-xe-2-2-0-0.nss.udel.edu) 210.000ms
15 13    128.175.111.97 (chp-rt5-xe-1-0-35-0.nss.udel.edu) 210.000ms
16 14    128.175.13.92 (copland.udel.edu) 210.000ms
```

Notice the first hop is the EVSE (172.17.2.1). Hops 2-5 are used to get outside of DTU's routers. Hop 6 is fsknet.dk, the Danish national research network. Hops 7 is nordu.net, the Nordic research network. At hop 8 and afterwards the packet reaches US mainland, and after reaching a few more US routers it eventually arrives at the udel.edu network.

www.elektro.dtu.dk

Department of Electrical Engineering
Centre for Electric Technology (CET)
Technical University of Denmark
Elektrovej building 325
DK-2800 Kgs. Lyngby
Denmark
Tel: (+45) 45 25 38 00
Fax: (+45) 45 93 16 34
Email: info@elektro.dtu.dk